Metamaterial Structure Inspired Miniature RF/Microwave Filters

A thesis submitted for the degree of PhD at the University of Manchester

Faculty of Science and Engineering

2016

ABDULLAH ALBURAIKAN

SCHOOL OF ELECTRICAL AND ELECTRONIC ENGINEERING

MATERIALS, DEVICES AND SYSTEMS DIVISION

Table of Content

Word Count: 36662

List of Figures

List of Tables

List of Abbreviations

ADS   Advanced design system

BPF   Bandpass filter

BW   Bandwidth

BJT   Bipolar junction transistor

CAD   Computer aided design

CRLH   Composite right/left-handed

CMOS   Complementary metal-oxide-semiconductor

CSRR   Complementary split ring resonator

DGS   Defected ground structure

DNG   Double negative

EM   Electromagnetic

FBW   Fractional bandwidth

HTS   High temperature superconductor

FoM   Figure of merit

LH   Left-handed

LPF   Low pass filter

LTCC   Low-temperature co-fired ceramics

MMIC   Monolithic microwave integrated circuit

MTM   Metamaterial

NRI   Negative refractive index

PCB   Printed circuit board

PLH   Purely left-handed

PRH   Purely right-handed

PN   Phase noise

RF   Radio frequency

SRR   Split ring resonator

TL   Transmission line

VCO   Voltage controlled oscillator

List of Symbols

ω   Angular frequency

β   Propagation constant

α   Attenuation constant

γ   Complex propagation constant

ε   Electric permittivity

θ   Electrical length

λ   Wavelength

μ   Permeability

τ   Time delay

Abstract

Metamaterial Structure Inspired Miniature RF/Microwave
Filters
Abdullah Alburaikan

A thesis submitted to the University of Manchester for the
degree of Doctor of Philosophy, 2016

Novel feedback signal interference concept for bandpass filter (BPF) design is proposed in this thesis. This new concept was utilized to design wide stopband BPF with superior performance for WLAN applications. The proposed filtering structure consists of two simple coupled-line couplers. The first coupler was employed within the main signal path and the second coupler which is open circuited at the opposite ends was used for the feedback circuit. This new filtering structure was fabricated using low temperature co-fired ceramic technology. The fabricated BPF exhibits an insertion loss (IL) of -1.3 dB with a 3dB fractional bandwidth of 13% at a centre frequency of 2.4 GHz. Furthermore, an attenuation level of -15 dB is achieved up to $4.7f_o$. Using stepped impedance coupled-lines in the feedback; the stopband performance of the proposed structure can be significantly improved while keeping passband performance intact. Furthermore, the feedback signal interference concept proved to be versatile and can be used to design high selectivity microstrip BPF using composite right/left handed transmission line unit cell in the feedback circuit. The measured results show that roll-up/down rate of more than 300 dB/GHz can be achieved with low IL.

The spectrum based quality factor for CRLH TL based BPF is explored and thoroughly studied in this thesis to design a low phase noise oscillator. The proposed metamaterial BPF has higher spectrum based quality factor within the left-handed region due to the slow-wave propagation. This intriguing feature enables the design of a free-running oscillator with excellent phase noise performance operating at a frequency of 2.05 GHz. The fabricated oscillator demonstrates a phase noise of -126.7 dBc/Hz at 100 kHz frequency offset and a FOM of -207.2 dBc/Hz at a 1 MHz frequency offset, being one of the very best reported so far.

Many microstrip multi-band BPF design techniques are presented in the literature that offers superior performance in terms of IL, 3dB FBW, and high selectivity. These methods mainly lack the ability to obtain high performance with compact size. Coupled slotted open stubs are used to design a miniaturized dual-wideband BPF. Interdigital capacitor and inner open stubs are used to improve rejection level within the stopbands and increase selectivity. The measurement results reveal that the fabricated dual-wideband BPF has two passbands with a 3dB FBW of 117% and 36%, at respective centre frequencies of 1 GHz and 6.65 GHz. The filter has a super compact size (0.09 λg × 0.05 λg) where λg denotes the guided wavelength at the centre frequency of the first passband and exhibits an attenuation level greater than 20 dB up to 12 GHz.

Declaration

No portion of the work referred to in the thesis has been submitted in support of an application for another degree or qualification of this or any other university or other institute of learning.

Copyright Statement

The author of this thesis (including any appendices and/or schedules to this thesis) owns certain copyright or related rights in it (the "Copyright"), and he has given The University of Manchester rights to use such Copyright for administrative purposes. Copies of this thesis, either in full or in extracts, and whether in hard or electronic copy, may be made only in accordance with the Copyright, Designs and Patents Act 1988 (as amended) and regulations issued under it or, where appropriate, in accordance with licensing agreements which the University has from time to time. This page must form part of any such copies made.

The ownership of certain Copyright, patents, designs, trademarks and other intellectual property (the "Intellectual Property") and any reproductions of copyright works in the thesis, for example graphs and tables ("Reproductions"), which may be described in this thesis, may not be owned by the author and may be owned by third parties. Such Intellectual Property and Reproductions cannot and must not be made available for use without the prior written permission of the owner(s) of the relevant Intellectual Property and/or Reproductions.

Further information on the conditions under which disclosure, publication and commercialisation of this thesis, the Copyright and any Intellectual Property University IP Policy (see http://documents.manchester.ac.uk/display.aspx?DocID=24420), in any relevant Thesis restriction declarations deposited in the University Library, The University Library's regulations (see http://www.library.manchester.ac.uk/about/regulations/) and in The University's policy on Presentation of Theses.

Acknowledgments

First, I would like to express my deepest gratitude to my supervisor, Dr. Zhirun Hu, for his infinite support and outstanding technical guidance throughout this research project. The successful completion of this research would not have been possible without his constructive comments and constant encouragements.

I would like to express my genuine appreciation to my colleague and best friend, Dr. Mohammed Aqeeli, for his help, useful discussion, and advice throughout the years I spent at Manchester University. I am extremely grateful to my co-supervisor Prof. Ali Rezazadeh, and advisor Prof. Zhipeng Wu for their assistance and advice during my studies. From the bottom of my heart, I would like to thank all PhD students and members of staff at at the school of Electrical and Electronic Engineering for their helpful advice and simulating discussions on different issues related to my research.

Finally, my deep appreciation and special thanks goes to all my family members: my parents Othman Alburaikan and Mona Alsaied, my brothers: Abdulrahman, Ahmad, Abdulaziz, Omar and Abdulmohsen, my wife: Qamar Almutawa, and my In-Laws : Ibrahim Almutawa, Haleema Alqeesi, Bedoor Almutawa, Husain Almutawa, Bader Almutawa and Taiba Almutawa for their incredible support and sacrifices throughout these years which enabled me to complete my studies.

Dedicated with love to my parents, my wife, and my kids..

Chapter 1: Introduction

1.1 Overview

Electromagnetic metamaterials (MTMs) can be described as "artificial effectively homogenous electromagnetic structures with unusual properties not readily available in nature"[1]. The structural average cell size p needs to be at least smaller than a quarter of guided wavelength λ_g to fulfil the effective homogeneity condition. This condition ensures refraction dominates over scattering or diffraction for reliable wave propagation inside the MTM media. When this condition is met, the structure can be seen as a material with constitutive parameters of electric permittivity ε and permeability μ, where it is electromagnetically uniform along the direction of propagation [2]. When the MTM media simultaneously exhibit negative ε and μ, it can be defined as left-handed (LH) MTM. Such materials can be identified by anti-parallel phase and group velocities because of their double negative parameters [1].

In 1967, Viktor Veselago predicted the existence of "substances" or LH MTM that permit backward wave propagation [3]. Such a prediction was validated three decades later by Smith [4] when he suggested a structure consisting of split ring resonators (SRR) arranged periodically and continuous thin wires that would allow wave propagation at a certain frequency region with negative-ε and negative-μ. SRR-based LH MTMs can be considered as a resonant type structure, which suffers from high loss and exhibits narrow bandwidth. Hence, the transmission line (TL) approach of MTM presented by Caloz in [5, 6] was adopted to design LH structures that exhibit low loss and wide bandwidth characteristics. These advantages of LH structure can be utilized to design high performance RF/microwave components such as filters and oscillators.

Ultra-wideband (UWB) bandpass filter (BPF) is a challenging task for RF/microwave engineers since UWB systems require BPF with low insertion loss, sharp passband selectivity and compact size. One of the classical methods to construct such filtering structure is by cascading high pass filter (HPF) with a low pass filter (LPF). Using conventional HPF and LPF to design UWB BPF require large circuit size and LH TL can be used to reduce the filter footprint and enhance the filtering performance [7, 8].

Multi-band BPF is another interesting research topic that attracted researchers from both academia and industry. Modern wireless communication technologies require multi-mode transceivers that can operate at different frequency bands [9]. Dual-band BPF is an essential component in these transceivers and the desired specifications for these filters include high selectivity, good isolation between the passbands, and compact size. Coupled slotted open stubs and interdigital capacitor are utilized in this thesis to design super compact dual-wideband BPF with high selectivity and wide upper stopband bandwidth.

The crowded frequency spectrum places stringent requirements on all components involved in wireless communication system design. One of these components is oscillator where tight specifications on the oscillator's phase noise and power consumption are required. The spectrum based quality factor for CRLH TL based BPF is thoroughly studied for the first time in this research work to design a low phase noise oscillator. Slow wave propagation within the left-handed region enabled the achievement of high spectrum based quality factor using the proposed CRLH TL based BPF. Simulation results and mathematical analysis for the proposed BPF proved that high spectrum quality factor reduce phase noise significantly which enable the design of a free-running oscillator with excellent phase noise performance operating at a frequency of 2.05 GHz. The fabricated oscillator demonstrates a phase noise of -126.7 dBc/Hz at 100 kHz frequency offset and a FOM of -207.2 dBc/Hz at a 1 MHz frequency offset.

New concept of feedback signal interference is presented in this research work and utilized to design high performance BPF. As a design example of this new filtering structure, wide stopband BPF with superior performance for WLAN applications was designed, fabricated, and measured. This new filtering structure consists of two simple coupled-line couplers. The first coupler was employed within the main signal path and the second coupler which is open circuited at the opposite ends was used within the feedback circuit. The fabricated BPF has an insertion loss (IL) of -1.3 dB with a 3dB fractional bandwidth of 13% at a centre frequency of 2.4 GHz. Furthermore, a rejection level of -15 dB is achieved up to $4.7f_o$. Using stepped impedance coupled line; the upper stopband bandwidth was extended to $7.2\ f_o$ with similar rejection level. Feedback signal interference concept proved to be versatile and can be used to design high selectivity microstrip BPF using composite right/left handed transmission line unit cell in the feedback circuit. The measured results show that roll-up/down rate of more than 300 dB/GHz can be achieved with low IL.

1.2 Research Objectives

Recent advancement in mobile and satellite communication requires the miniaturisation of system dimensions without affecting electrical performance. The work presented in this thesis firstly focuses on reducing the size and fabrication complexity in the design of UWB microstrip bandpass filter while maintaining the same frequency response. The first phase of this research project includes designing UWB BPF based on CRLH TL while the second phase involves realizing super compact dual-band BPF using both bandstop and highpass structures. The third objective was to study the spectrum based quality factor for CRLH TL based BPF and design a filter based oscillator that has low phase noise and low power consumption. The last objective

was to present a new and simple filtering topology that can be used to design passive BPF with high selectivity and wide upper stopband.

1.3 Organisation of the thesis

An overview of the research project is presented in chapter 1. Chapter 2 provides an introduction to filter theory and methods used to design conventional microwave filters. An introduction to LH MTM and a literature review of MTM filters are included in chapter 3. Moreover, chapter 3 present a miniaturised design of UWB BPF using CRLH TL unit cell where grounded stubs are used in the first design and capacitive patches are used in the second design to realize a via-less UWB BPF structure. Chapter 4 presents the design and optimisation of super compact dual-wideband bandpass filters that are based on quarter-wavelength open stubs and interdigital capacitors. Full study of spectrum based quality factor for CRLH TL based BPF is presented in chapter 5 which includes a design for a low phase noise oscillator using complimentary split ring resonators (CSRR) based BPF. Feedback signal interference concept is discussed in chapter 6 where several BPF design examples are included to show the effectiveness of the proposed new topology in designing BPF with superior performance.

Chapter 2: Filter Theory and Design

2.1 Introduction

Most of today's RF/microwave applications operate in the frequency range of 300 kHz up to 300 GHz as shown in Figure 2.1. Communications, radar, navigation and radio astronomy are some of the applications that operate on different frequency bands within this frequency range. Hence, filters are needed to select, supress, or combine RF/microwave signals within certain frequency bands for each application [10]. Low-pass, high-pass, bandpass and band-stop are the typical filter functions needed in any RF/microwave application. In the late 1930s, filter theory and practice started to develop, and the image parameter method of filter design was introduced [11]. This method was suitable for low-frequency filters which are mainly utilized in radio and telephony. The insertion loss method was introduced later, and most of today's microwave filter design is based on this method.

Recent technologies, such as wireless communication, challenge RF and microwave filter designers and researchers to design filters that perform better with compact size and low fabrication cost. Designing such a filter can be accomplished today because of recent advancement in new materials and fabrication technologies such as high-temperature superconductor (HTS), monolithic microwave integrated circuit (MMIC), and low-temperature co-fired ceramics (LTCC) [10]. Also, advances in computer-aided design (CAD) tools complemented the above mentioned fabrication technologies to design novel filters with exceptional filtering characteristics.

The main objective of this research is to suggest a new approach in RF/microwave filter design, which can either provide size reduction while maintaining similar passband/stopband

performance or improve filtering characteristics beyond what, can be achieved using classical filter design methods. In the following section, a review of basic concepts of filter design theory is presented.
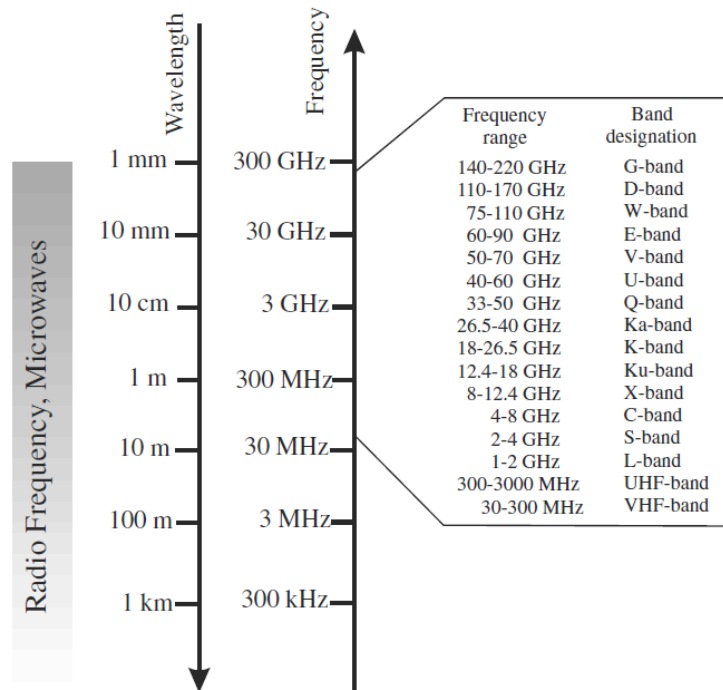
Figure 2.1 RF/microwave spectrums [10]

2.2 Filter Theory

There are two well-known methods for classical filter design: image parameter and insertion loss. Filters designed using the first method can provide the desired cut-off frequencies and attenuation characteristics by cascading simple two-port filter networks. The drawback of this method is that particular frequency response cannot be specified and an iterative process is needed to get the desired results. The second method, insertion loss, uses a network synthesis technique, which can completely specify the frequency response desired for the designed filter. In this method, the design process starts with LPF prototypes that are scaled to the appropriate impedance level and frequency. Then, conversion of the prototype design is done using

transformations to achieve the required frequency range and impedance level. However, microwave filters cannot be implemented directly using the above mentioned methods since both methods provide lumped-element circuits that are difficult to realize at high RF and microwave frequencies. Moreover, the range of values for available capacitors and inductors is limited and need to be estimated by distributed elements such as transmission lines. Approximation of lumped elements is done using transformations, such as Richard's transformation and the Kuroda identities, which allow practical microwave filter implementation.

As stated in the previous section, only basic concepts of filter theory and design will be presented in this chapter, and interested readers can refer to [10, 12, 13] for further detailed study of theoretical background about microwave filters.

2.3 Network Analysis

Most components of RF/microwave filters can be characterized by a two-port network, as shown in Figure 2.2. Different parameters and variables can be used to analyse this network, such as network variables, scattering parameters (S-parameters), short-circuit admittance parameters (Y-parameters), open-circuit impedance parameters (Z-parameters) and transmission parameters (ABCD-parameters). These parameters can be converted to one another using the available formulas mentioned in [11].
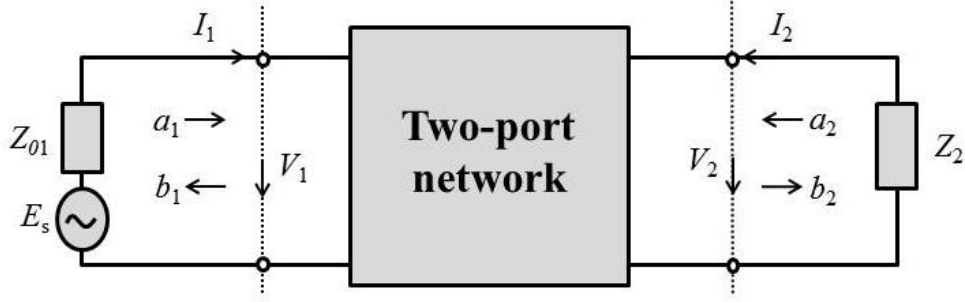
Figure 2.2 Network variables for two-port network [10].

2.3.1 Network Variables

In the above figure, Voltage and current values at ports 1 and 2 are expressed respectively as V_1, V_2, and I_1, I_2. E_s is the source voltage and Z_{01}, Z_{02} are the terminal impedances. Wave parameters a_1, b_1 and a_2, b_2 are defined to characterise the two-port network because voltage and current are hard or impossible to measure at microwave frequencies. Incident and reflected waves are represented by a, and b respectively. Voltage and current variables can be defined in terms of wave variables as stated in the following equations [10]:

$$V_n = \sqrt{Z_{0n}}\,(a_n + b_n) \tag{2.1a}$$

$$I_n = \frac{1}{\sqrt{Z_{0n}}}\,(a_n + b_n) \tag{2.1b}$$

$$a_n = \frac{1}{2}\left(\frac{V_n}{\sqrt{Z_{0n}}} + \sqrt{Z_{0n}}\,I_n\right) \tag{2.1c}$$

$$b_n = \frac{1}{2}\left(\frac{V_n}{\sqrt{Z_{0n}}} - \sqrt{Z_{0n}}\,I_n\right) \tag{2.1d}$$

Where $n = 1$ and 2.

2.3.2 Scattering Parameters

The scattering (S) parameters of a network relate incident voltage waves to reflected voltage waves at any arbitrary ports. For an N port system, S parameters matrix contains N^2 elements,

27

relating complex transmission and reflection coefficients of the network. For a 2 port network, this means that scattering matrix contains four elements, which is shown below [11]:

$$S_{11} = \frac{b_1}{a_1}\bigg|_{a_2 = 0}, \quad S_{12} = \frac{b_1}{a_2}\bigg|_{a_1 = 0}$$

$$S_{21} = \frac{b_2}{a_1}\bigg|_{a_2 = 0}, \quad S_{22} = \frac{b_2}{a_2}\bigg|_{a_1 = 0} \tag{2.2}$$

S_{11} and S_{22} indicates the reflection coefficients of the network at ports 1 and 2 respectively, while S_{21} and S_{12} indicates the transmission coefficients in a similar fashion. Reflection coefficients, in this context, refer to the ratio of reflected voltage wave to the incident voltage wave at the same port. This is also the same for transmission coefficients, which refers to the ratio of incident voltage wave at one port, to the incident voltage wave at the other port.

In order to correctly determine the S parameters of a network, reflections at the ports other than the driven port should be eliminated. Therefore, it is assumed that all ports except the nth port of S_{mn} are terminated with loads that are matched to the network characteristic impedance. This way, the reflected voltage waves at these matched ports will be eliminated. In a 2 port system, for example, this will mean that for S_{m1} measurements, port 2 should be terminated with a matched load, thus reducing a_2 to zero. Similarly, doing S_{m2} measurements requires that port 1 should be terminated with a matched load, thus, reflected voltage wave at port 1 (a_1) disappears. As a general description, for an N port network, S_{mm} measurements require that all ports other than port m should be connected to matched loads. Similarly, S_{mn} measurements indicate that all ports except port m and n are terminated with matched loads.

The S parameters are complex variables and can be expressed in terms of amplitudes and phases as:

$$S_{mn} = |S_{mn}|e^{j\varphi_{mn}} \quad \text{Where } m,n = 1,2. \tag{2.3}$$

Amplitudes of S parameters are defined in decibels (dB) as:

$$20\log|S_{mn}|\ dB \quad m,n = 1,2 \tag{2.4}$$

Two important parameters for filter design can be defined using S parameters. These parameters are: insertion loss (L_A) and return loss (L_R), which can be represented as:

$$L_A = -20\log|S_{mn}| \quad dB \quad m,n = 1,2\ (m \neq n) \tag{2.5a}$$

$$L_R = 20\log|S_{nn}| \quad dB \quad n = 1,2 \tag{2.5b}$$

The first parameter measures the amount of energy that is lost between port n and m and L_R represents the return loss at port n. Signals transmitted through a filter experience some delay at the output, and there are two parameters, phase delay and group delay, which are related to this delay and can be defined as:

$$\tau_p = \frac{\varphi_{21}}{\omega}\ (sec) \tag{2.6}$$

$$\tau_d = -\frac{d\varphi_{21}}{d\omega}\ (sec) \tag{2.7}$$

Port 1 is the input port and port 2 is the output port. Group delay is basically the delay of a packet of frequencies while phase delay considers the delay confronted by a single sinusoid. Other two-port network parameters mentioned earlier are summarised and presented in Table 2.1.

Table 2.1. Summary of two-port network parameters

Parameter	Definition
Short-circuit Admittance parameters: *Y- parameters*	$Y_{11} = \dfrac{I_1}{V_1}\bigg\vert V_2 = 0 , Y_{12} = \dfrac{I_1}{V_2}\bigg\vert V_1 = 0$ $Y_{21} = \dfrac{I_2}{V_1}\bigg\vert V_2 = 0 , Y_{22} = \dfrac{I_2}{V_2}\bigg\vert V_1 = 0$ $\begin{bmatrix} I_1 \\ I_2 \end{bmatrix} = \begin{bmatrix} Y_{11} & Y_{12} \\ Y_{21} & Y_{22} \end{bmatrix} \cdot \begin{bmatrix} V_1 \\ V_2 \end{bmatrix}$
Open-circuit Impedance parameters: *Z- paramters*	$Z_{11} = \dfrac{V_1}{I_1}\bigg\vert I_2 = 0 , Z_{12} = \dfrac{V_1}{I_2}\bigg\vert I_1 = 0$ $Z_{21} = \dfrac{V_2}{I_1}\bigg\vert I_2 = 0 , Z_{22} = \dfrac{V_2}{I_2}\bigg\vert I_1 = 0$ $\begin{bmatrix} V_1 \\ V_2 \end{bmatrix} = \begin{bmatrix} Z_{11} & Z_{12} \\ Z_{21} & Z_{22} \end{bmatrix} \cdot \begin{bmatrix} I_1 \\ I_2 \end{bmatrix}$
ABCD parameters	$A = \dfrac{V_1}{V_2}\bigg\vert I_2 = 0 , B = \dfrac{V_1}{-I_2}\bigg\vert V_2 = 0$ $C = \dfrac{I_1}{V_2}\bigg\vert I_2 = 0 , D = \dfrac{I_1}{-I_2}\bigg\vert V_2 = 0$ $\begin{bmatrix} V_1 \\ I_1 \end{bmatrix} = \begin{bmatrix} A & B \\ C & D \end{bmatrix} \cdot \begin{bmatrix} V_2 \\ -I_2 \end{bmatrix}$

Furthermore, it should be mentioned here that these parameters can be used in composite networks that contain many sub-networks and elements connected in series, parallel, or in cascade.

2.4 Filter Classification and Design methods

Filters can be classified into three main types: active, passive, and hybrid filters [14]. An active filter requires an external power source whilst passive filters can be used without an external

power source. Microwave systems are designed to be energy efficient, so active filters are the considered by filter designer when stringent filtering specifications are required [15]. Passive filters can be further categorised into lumped and distributed categories. The first category, the lumped element, consists of filter constructed only from passive devices such as capacitors, inductors, and resistors. RC and LC filter falls under the first category of the lumped element filter. Assuming lossless LC components, LC filters have no resistor, so they do not dissipate power and can provide good filtering characteristics in theory. In practice, lossy lumped components are used and required filtering performance might not be achieved due to parasitic and limited available values of lumped components. The second category, the distributed element filter, can be realised based on transmission line implementation of the components of the lumped-element filter prototype. Transmission line is considered one of the many filter technologies that can be used to construct distributed element filter as shown in Figure 2.3.
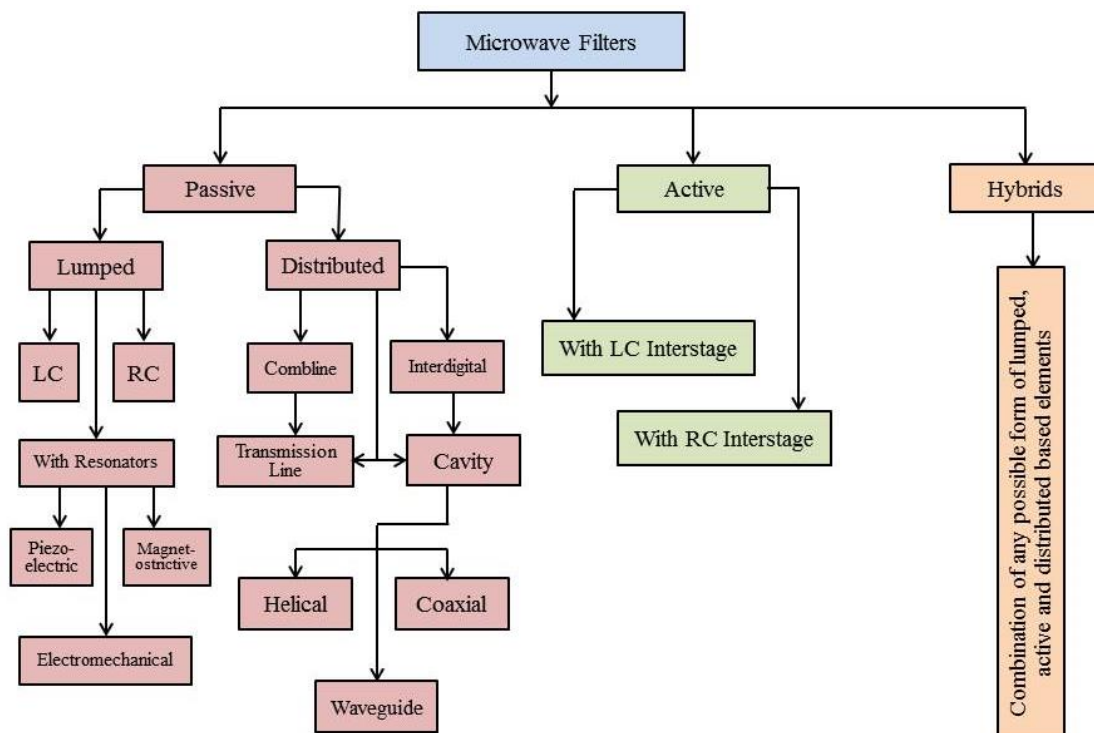
Figure 2.3 Types of microwave filters[15].

Helical resonator filters are known for their high quality factor, which indicates the rate of energy loss is much less than the stored energy of the resonator. The major drawbacks of such filters are their big size, assembly complexity, and significant production time [16]. Interdigital filter is commonly used in microstrip implementation to design bandpass filter of a compact size. Also, first spurious passband occurs at about three times the centre frequency of the first passband but requires a grounding microstrip resonator [17].
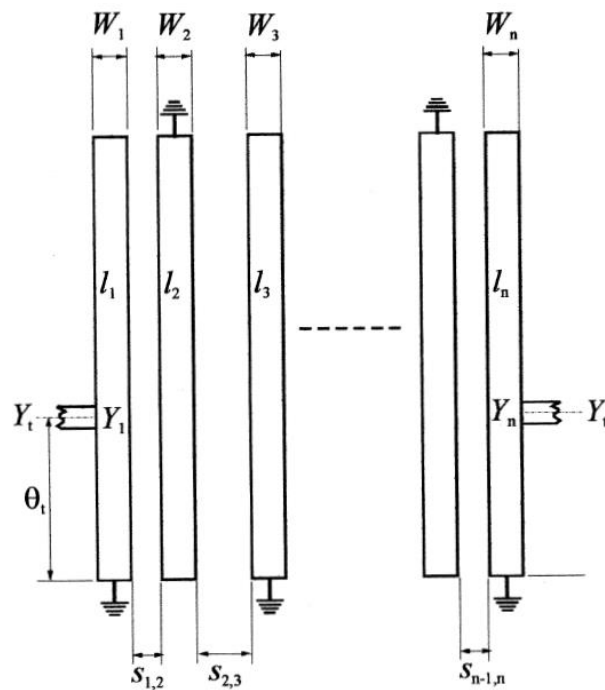
Figure 2.4 Common configuration for interdigital BPF where n denote the number of half-wave length resonators used and l_n, W_n are the length and width of these resonators [10].

Comb-line bandpass filter has a good rejection profile when the distributed and lumped elements of such filter are carefully designed [18]. Good rejection profile is needed to reduce interference from other communication systems.

The output response of the above mentioned filters can be lowpass, highpass, bandpass or bandstop. Moreover, a different function-based response, such as Butterworth (maximally flat),

Chebyshev, Bessel, and Elliptic, can be realised by designing such filters. Typical design requirements for filters are defined below:

- *Bandwidth (BW)*: The difference between the upper and lower cutoff frequencies where the amplitude is 3dB of the nominal passband value, measured in hertz.

- *3dB Fractional bandwidth* (3dB FBW) of a filter can be calculated by dividing the 3dB bandwidth by the centre frequency of filter.

- *Insertion loss (IL)*: a measure of the signal power loss introduced by the circuit.

- *Return loss:* The loss of signal power due to reflections in a network, produced by mismatching in impedance of the transmission line.

- *Ripple:* a measure of the variation of insertion loss amplitude across the filter's passband as illustrated in Figure 2.5, and it can be minimized by increasing the order of the filter [12].
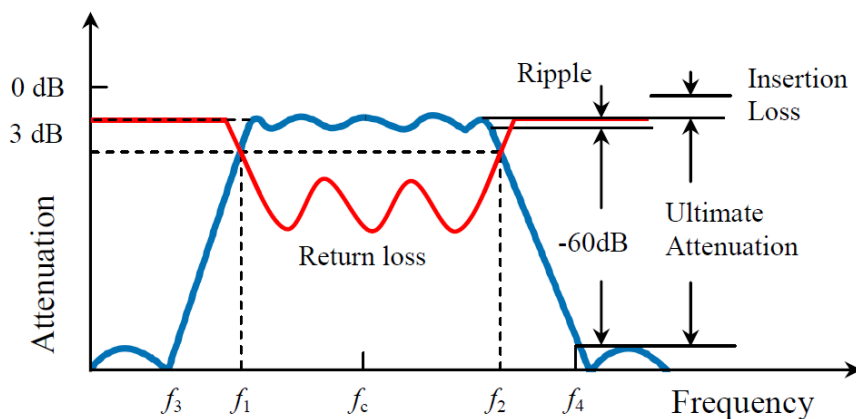
Figure 2.5. Typical bandpass filter response [15].

- *Degree (order)*: The degree of the filter can be determined by the number of reactive elements in the circuit and can control the slope of the attenuation curve.

- *Circuit-Q (circuit quality factor)*: is the centre frequency divided by the bandwidth: $Q= f_c/(f_2-f_1)$**.** Thus, higher Q means narrower bandwidth and better selectivity of a bandpass filter [19].

- *Ultimate attenuation*: The maximum attenuation of the filter in the stopband region that can be improved by increasing the order of the filter [11].

2.4.1 Periodic Structures
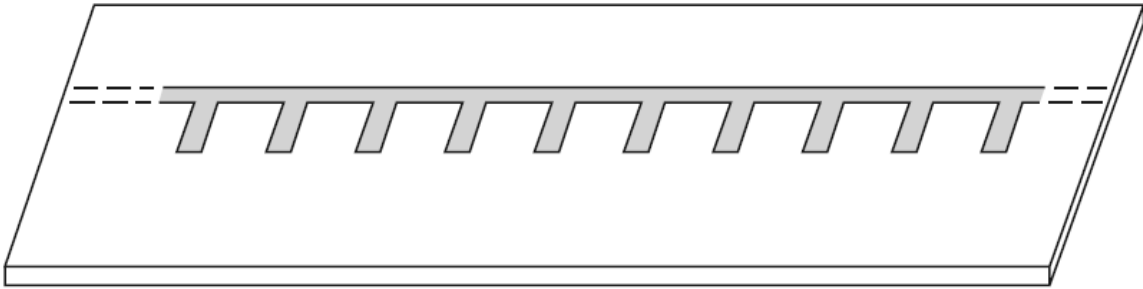
Figure 2.6. Example of periodic structure where microstrip line is loaded with periodic open stubs [11].

Periodic structures are widely used in the design of passive devices and can be referred to transmission lines loaded at periodic intervals with reactive elements (inductors and capacitors), which can be designed as discontinuities in the line itself as seen in Figure 2.6. The interest of these structures in filter design arises from its basic properties, which include passband and stopband characteristics and slow-wave propagation (slower than the phase velocity of unloaded line). Periodic structure can be further analysed by considering the infinite line shown in Figure 2.7.
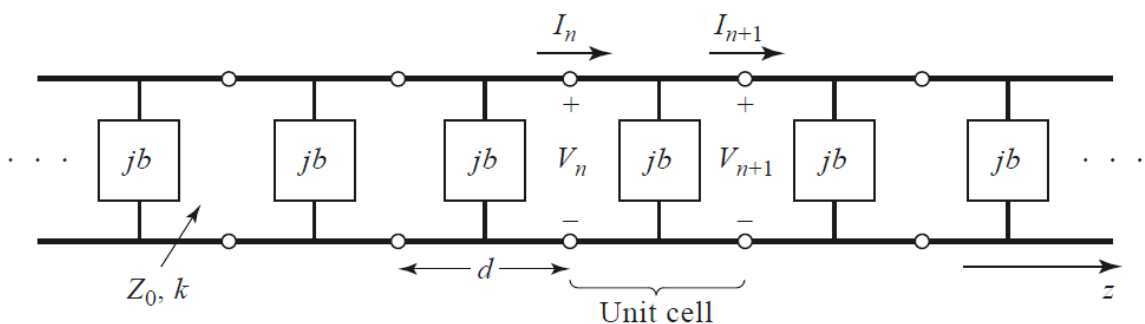
Figure 2.7. Equiv. circuit of transmission line loaded periodically. The characteristic impedance of the unloaded line [11].

The length of each unit cell of this TL is defined as *d* where a shunt susceptance, *b*, is located at the midpoint of the line which is normalized to the characteristic impedance Z_0. Assuming this TL is connected to identical two-port network, the wave propagating in +*z* direction can be described as [11]

$$V(z) = V_0^+(e^{-\gamma z} + \Gamma e^{\gamma z}) \tag{2.8a}$$

$$I(z) = \frac{V_0^+}{Z_0}(e^{-\gamma z} - \Gamma e^{\gamma z}) \tag{2.8b}$$

With a phase reference at *z* = 0 and γ is the complex propagation constant. Assuming γ = α +jβ and using transmission matrix analysis, we have

$$\cosh \gamma d = \cosh \alpha d \, \cos \beta d + j \, \sinh \alpha d \, \sin \beta d = \cos \theta - \frac{b}{2} \sin \theta \tag{2.9}$$

Where θ = *k*d, and *k* is the propagation constant of the unloaded line. Passband and stopband are characterized by the attenuation constant α and propagation constant β. Passband occurs when α=0 and β≠ 0 which correspond to the propagating wave on the periodic structure. In the other hand, the wave will be attenuated when β = 0, π and α≠0 which corresponds to the stopband [11].

When periodic structure is terminated with a load, the load impedance Z_L must be identical to the feeding transmission line impedance Z_0 to reduce reflections of incident power in the network. Dispersion relation for periodic structure can be characterised by plotting the *k*-β (or Brillouin) diagram. As seen in Figure 2.8, this diagram shows the propagation constant β versus frequency (or propagation constant of unloaded line *k*). Also, phase and group velocities related to dispersive structures can be interpreted from such a diagram.
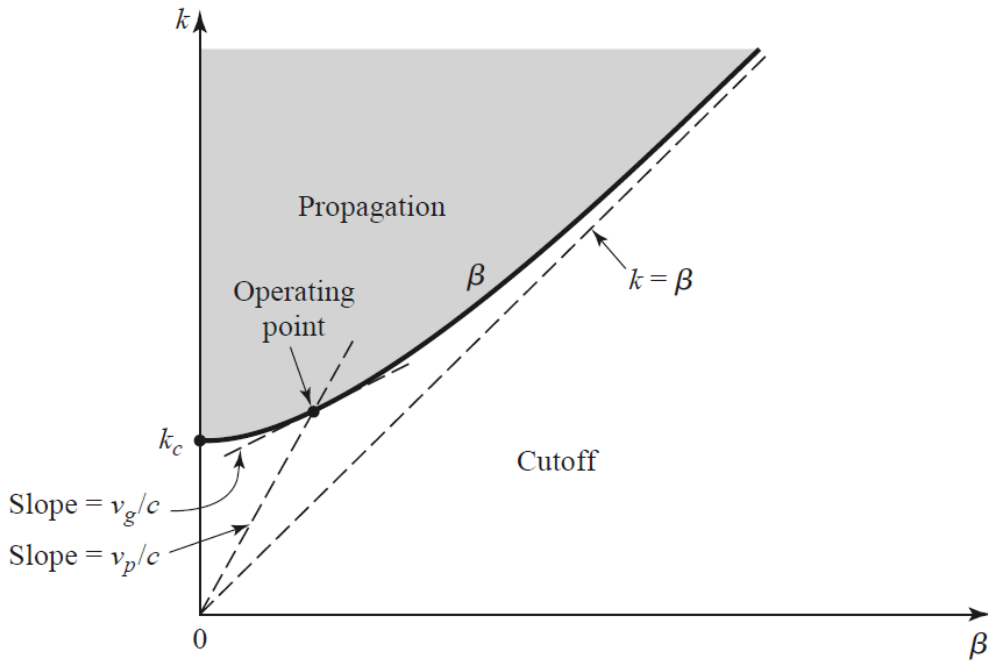
Figure 2.8. Brillouin diagram for a waveguide mode [11].

2.4.2 Image Parameter Method

Image parameter method is a quite simple method in filter design since it uses the image impedance Z_i and voltage transfer function to specify filtering characteristics of simple two-port networks. The image impedances for a two-port network are "the two impedances which will terminate the ports simultaneously in such a way that, at each port, the impedances seen in both direction are equal" [20]. The major drawback of this method is that an arbitrary frequency response cannot be incorporated into the filter design.

Symmetrical T and π circuit are the basic building blocks for filters designed by the image parameters method. The image parameters of T and π networks, presented in Table 2.2, can be used to develop low-pass and high-pass filter section.

Table 2.2. Image parameters for T and π networks [11].
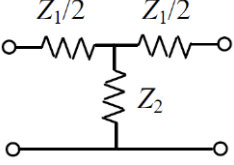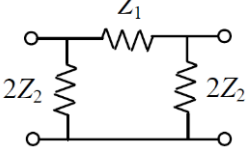
T Network	π Network
\n\nT Network	\n\nπ Network
ABCD parameters: $A = 1 + \frac{Z_1}{2Z_2}$ $B = Z_1 + \frac{Z_1^2}{4Z_2}$ $C = 1/Z_2$ $D = 1 + \frac{Z_1}{2Z_2}$	ABCD parameters: $A = 1 + \frac{Z_1}{2Z_2}$ $B = Z_1$ $C = \frac{1}{Z_2} + Z_1/4Z_2^2$ $D = 1 + \frac{Z_1}{2Z_2}$
Z parameters $Z_{11} = Z_{22} = Z_2 + Z_1/2$ $Z_{12} = Z_{21} = Z_2$	*Y* parameters $Y_{11} = Y_{22} = 1/Z_1 + 1/2Z_2$ $Y_{12} = Y_{21} = 1/Z_1$
Image impedance: $Z_{iT} = \sqrt{Z_1 Z_2}\sqrt{1 + Z_1/4Z_2}$	Image impedance: $Z_{i\pi} = \sqrt{Z_1 Z_2}/\sqrt{1 + Z_1/4Z_2}$
Propagation constant: $e^\gamma = 1 + \frac{Z_1}{2Z_2} + \sqrt{\frac{Z_1}{Z_2} + \frac{Z_1^2}{4Z_2^2}}$	Propagation constant: $e^\gamma = 1 + \frac{Z_1}{2Z_2} + \sqrt{\frac{Z_1}{Z_2} + \frac{Z_1^2}{4Z_2^2}}$

Low-pass and high-pass constant-*k* filter can be designed using the image parameters for *T* and π networks. The passband of this filter occurs when the image impedance Z_i is real and propagation constant γ is imaginary, whereas imaginary Z_i and real value of γ corresponds to the stopband of the filter [13]. As mentioned earlier, the image parameter method requires constant image impedance at both ports that cannot be achieved by constant-*k* filter since Z_i is

a function of frequency, and it is hard to minimize the mismatch with the source or load impedance. Another disadvantage of such a filter is the low attenuation around cut-off frequency, which can be solved by using the *m*-derived filter section. Faster attenuation rate past cut-off frequency can be achieved in the *m*-derived filter by introducing a pole of attenuation in the stopband using an LC resonator in the shunt arm of the *T* and π networks. Although an *m*-derived filter can have a sharp roll-off response, the attenuation decreases for frequencies past the attenuation pole, which results in poor stopband performance. Composite filters, which are basically a combination of constant-*k* and *m*-derived filter sections, can improve stopband rejection and impedance matching to source and load impedance. Controlling the composite filter response is limited to the value of *m* for the sharp roll-off section once the cut-off frequency and impedance are specified. Hence, it is unclear how a filter designed by the image parameter method can be further improved.

2.4.3 Insertion loss Method

Insertion loss method can be used to obtain a desired filter response that meets the application requirement. This method uses different types of transfer functions, such as Butterworth, Chebyshev, etc., responses to control amplitude and phase characteristics of the desired filter performance. The type of transfer function must be carefully chosen to meet the design constraint. For example, the Chebyshev response can be chosen if a sharp roll-off is required, while minimum insertion loss can be obtained when the Butterworth response is used. Moreover, this method offers a direct way to enhance filter performance by increasing the order of the filter.

In this method, filter response can be expressed in terms of power loss ratio P_{LR} or insertion loss as [11]:

$$P_{LR} = \frac{Power\ available\ from\ source}{Power\ delivered\ to\ load} = \frac{P_{in}}{P_{load}} = \frac{1}{1-|\Gamma(\omega)|^2} = 1 + \frac{M(\omega^2)}{N(\omega^2)} \qquad (2.10)$$

Where $|\Gamma(\omega)|^2$ is an even function that can be described in terms of two real polymonials M and N in ω^2. Some of the practical filter response include: *Butterworth, Chebyshev, Elliptical,* and *linear phase*. The characteristics for these filter responses are outlined below:

- *Butterworth* (also known as *maximally flat* or *binomial*):
- Flattest possible passband response can be obtained.
- Attenuation monotonically increases past the cut-off frequency.

- *Equal ripple*:
- Sharper roll-off can be obtained when compared to maximally flat response.
- Pass-band ripple occurs.
- Attenuation monotonically increases past the cut-off frequency.

- *Elliptical*:
- Equal-ripple responses can be observed in the passband and stopband.
- Steep roll-off rate can be achieved by specifying maximum passband attenuation A_{max}, and minimum stopband attenuation A_{min}.

- *Linear phase*:
- Linear phase response in the passband.
- Poor roll-off rate when compared to other filter responses.

The procedure of filter design using this method starts with the design of a low-pass filter prototype employing normalised impedance and frequency ($Z_s = 1$ Ω, $\omega_c = 1$ radian/s) as shown in Figure 2.9. Then, the prototypes are de-normalised by impedance transformation and frequency scaling and different types of filters can be synthesised by replacing the lumped-element component with a distributed circuit element.
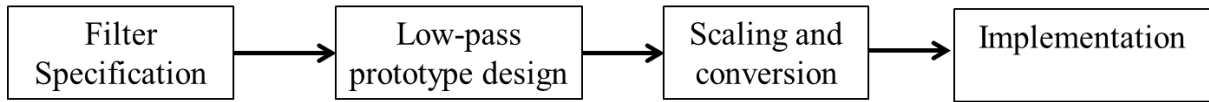
Figure 2.9 The process of filter design by insertion loss method [11].

Ladder network, which contains reactive elements forming a ladder, can be used to construct a low-pass filter prototype. The order of the filter corresponds to the number of reactive elements and normalised values of such elements that can be found in existing tables. After selecting a filter type, order and topology (e.g. 7th Chebyshev low pass filter) that suits the required specifications, a low pass prototype is built. Elements of this low pass prototype are then replaced with the corresponding elements according to the filter topology (e.g. series inductors are replaced with series LC pairs for a bandpass filter). Then, the normalised values of the filter components (also known as G values) are de-normalised according to the filter topology. This includes the impedance transformation, which is done in order to de-normalise the effect of the source impedance from the filter components. Source impedance, in this context, is the impedance of the input terminal. If number of elements to be used is odd, this impedance value will be the same for both filter terminals. If even number of elements are desired to be used, though, the impedance of the load side will be either higher or lower than the source impedance, depending on the selection of series or shunt placement of the first element. For filter elements, this impedance transformation is done as follows [11] :

$$L'_k = R_0 L_k \quad \text{(H)} \tag{2.11a}$$

$$C'_k = \frac{C_k}{R_0} \quad \text{(F)} \tag{2.11b}$$

$$R'_s = R_0 \quad (\Omega) \tag{2.11c}$$

$$R'_L = R_0 R_L \quad (\Omega) \tag{2.11d}$$

where R_0 is the de-normalised source impedance. L_k, C_k, R_L are the values for the original prototype, i.e. normalised values (g values). Primed variables represent de-normalised values for the respective components.

Frequency scaling should also be applied to the normalised values, in order to correctly find the inductance and capacitance values for the desired cut-off frequency. This is achieved by substituting the cut-off frequency ω of the low-pass prototype with ω/ωc. Since the low-pass prototype consists of series inductors and shunt capacitors, frequency scaling is done by dividing the normalised inductance and capacitance values (L_k and C_k) by the desired cut-off frequency. For a low-pass filter, assuming that impedance transformation is done beforehand, the final inductor and capacitor values can be written as follows:

$$L = \frac{L'_k}{\omega_c}$$
(2.12a)

$$C = \frac{C'_k}{\omega_c}$$
(2.12b)

where L'_k and C'_k are the impedance transformed inductance and capacitance values of the low-pass prototype, given in Eq. 2.11a-b. As resistance and conductance are not frequency dependent, scaling is not needed for those terms.

2.5 Filter implementation

Filter implementation at microwave frequencies using a lumped element is challenged with two main obstacles. The first is the limited availability of values for lumped element such as inductors, capacitors, and resistors. These components are manufactured with specific values that are determined by international standards, so the designed filter's capacitor and inductor values may not always match the standard values. The second is that the distance between

41

filter elements cannot be ignored at microwave frequencies, as filter elements start to act like distributed elements with increasing frequency. Parasitic reactance also become apparent when the sizes of components become closer to the wavelength. In addition to this, soldering pads for surface mount components also create parasitic reactance that should be included in the equivalent circuits. These elements are restricted to operate at frequencies where the size of the element should be much smaller than a quarter-wavelength which is hard to implement at high frequencies. These problems can be solved using Richard's transformation [21] and Kuroda's identities. Richard's transformation can be used to substitute the inductors and capacitors of a lumped-element filter with grounded and open-circuited transmission line stubs as shown in Figure 2.10.
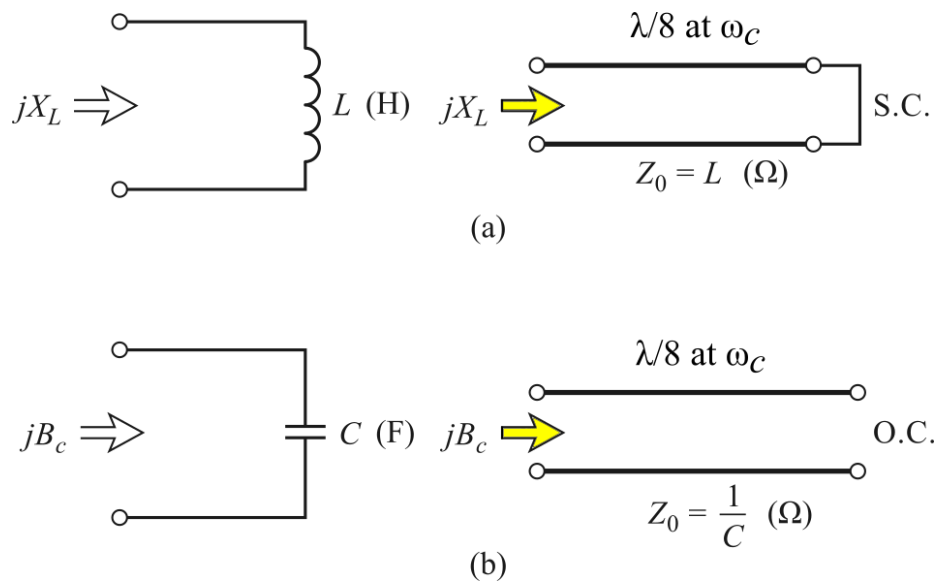
Figure 2.10 Richard's transformation. (a) An inductor is converted to a grounded stub. (b) A capacitor is converted into an open circuited stub [11].
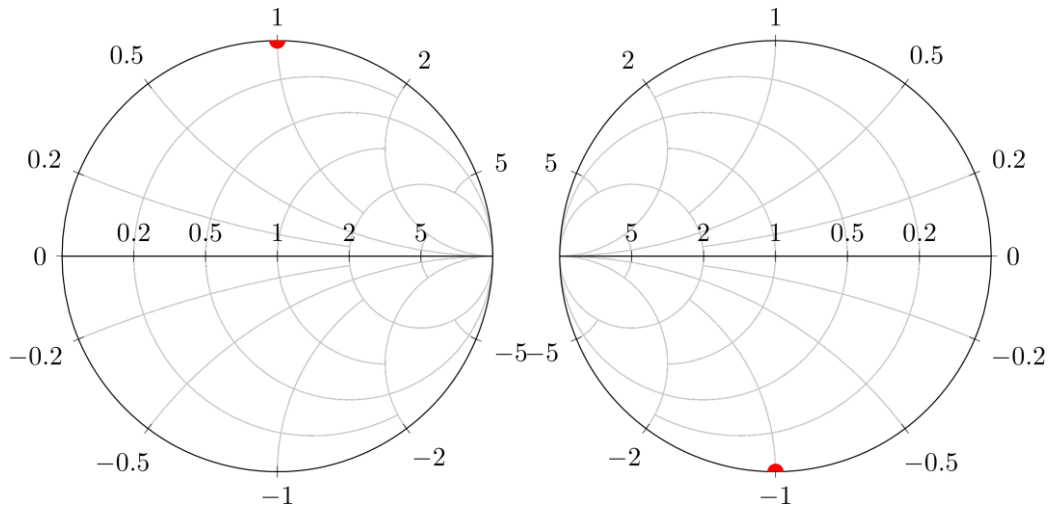
Figure 2.11 Richard's transformation for shorted unit length transmission line (a) and open circuited unit length transmission line visualized on impedance and admittance Smith charts.

In the Figure 2.11a, the Smith chart represents that the unit transmission line transforms the reactance to Z0. Similarly, the admittance Smith chart in Figure 2.11b shows that the unit transmission line transforms the open circuit susceptance to Z0. Representing these reactance and susceptance values with inductor and capacitor respectively, one can get the Richards transformed versions of the short and open circuited transmission lines shown in Figure 2.9.

Richard's transformation depends on the fact that a lossless one-port microwave network can be represented by cascaded transmission line elements, each with the same length, shorted or open circuited at the end. These transmission lines are called *unit elements*. This can be used to represent lumped elements as transmission line elements, or vice versa.

A one port network consisting of a single lossless inductor can be represented with a unit element shorted at the end. This is possible, since impedance of the lumped element at the centre frequency (w_c) can be made equal to the impedance of a shorted transmission line. Impedance of a single inductor and a shorted transmission line can be written as follows:

$$Z_{in}(\omega) = j\omega L \qquad (\Omega) \qquad (2.13)$$

$$Z_{in}(\omega) = jZ_o \tan \beta \ell \qquad (\Omega)$$

43

where L is the inductance, Z_o is the characteristic impedance of the transmission line, β is the phase constant and ℓ is the line length. Phase constant can be written in terms of wavelength of the centre frequency as follows:

$$\beta = \frac{2\pi}{\lambda_c} \tag{2.14}$$

Substituting the input impedance of the inductor into the transmission line, and setting the frequency to cut-off frequency, we get the following equality:

$$\omega_c L = Z_o \tan\frac{2\pi\ell}{\lambda_c}$$

$$L = Z_o \tan\frac{2\pi\ell}{\lambda_c}$$

The angular frequency at the LHS can be normalised to 1, since it is at cut-off. In addition to this, unit element length can be set as $\lambda_c/8$. This reduces the equality above to a simple form shown below:

$$L = Z_o \tan\frac{\pi}{4} \tag{2.15}$$

$$L = Z_o$$

Hence, a lumped inductor can be represented by a unit length transmission line that is shorted at one end. The same procedure can also be applied to a capacitor, where an open circuited unit element can represent the lumped capacitor. In this case, the input impedance of the capacitor will be written as follows:

$$Z_{in}(\omega) = \frac{1}{j\omega C} \qquad (\Omega) \tag{2.16}$$

$$Z_{in}(\omega) = jY_o \tan\beta\ell \qquad (\Omega)$$

Applying the same procedure as before, we find the following expression for the unit element characteristic impedance:

$$C = Y_o = \frac{1}{Z_o} \qquad (2.17)$$

Kuroda's identities can be utilised to obtain physical isolation between transmission line stubs, conversion of shunt stubs to series stubs, or vice versa, and the realisation of more practical characteristic impedance. When using a microstrip transmission line for filter implementation, it is preferable to use shunt stubs instead of series stubs. Kuroda identities can be used for such conversion, but another approach is to use impedance (K) or admittance (J) inverters. Since the input impedance of such inverters is inversely proportional to the load impedance or admittance, it can be used for a transformation of series elements to shunt elements and vice versa.

2.6 Coupled-line Filters

2.6.1 Coupled-lines Theory

Coupling can be defined as the power transferred between two or more unshielded transmission lines when positioned in close proximity to each other [22]. The power coupled from one line to another depends on many aspects. The physical structure, mode of propagation, and operating frequency are some of them. The operation of a coupled transmission line is usually assumed in the transverse electromagnetic (TEM) modes for coaxial line and stripline structures whereas microstrip line and slotline structures are working in quasi-TEM modes [11]. Edge-coupled and broad-side coupled are some of the geometries used to construct coupled transmission lines. Some of these geometries can be represented by the structure shown in Figure 2.12. The coupling fields will of course be different for the other transmission

45

line geometries. Coupled lines can be analysed by considering two types of excitations: odd and even modes. In the odd mode, strip conductors carry equal amplitude currents but in the opposite direction, whereas in even-mode excitation, equal amplitude currents travel in the same direction along the strip conductors as shown in Figure 2.13.
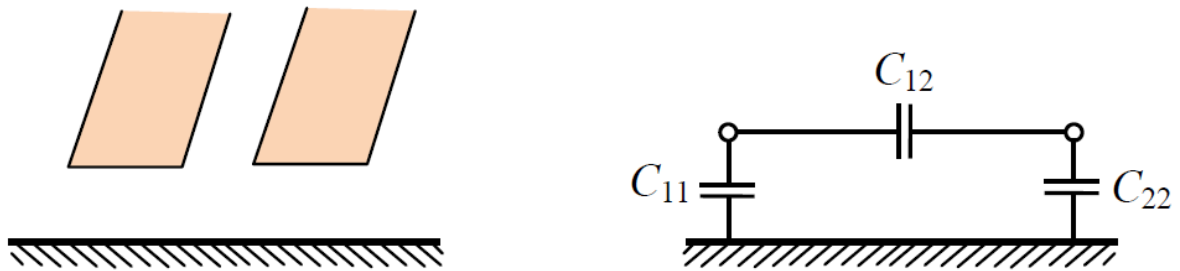
(a)
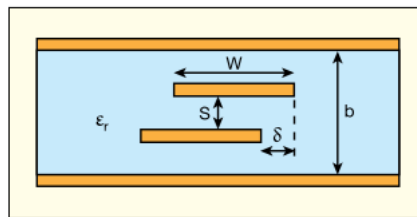
(b)

Figure 2.12 (a) A coupled microstrip TL and its equivalent capacitance network, (b) broadside coupled stripline TL [11].
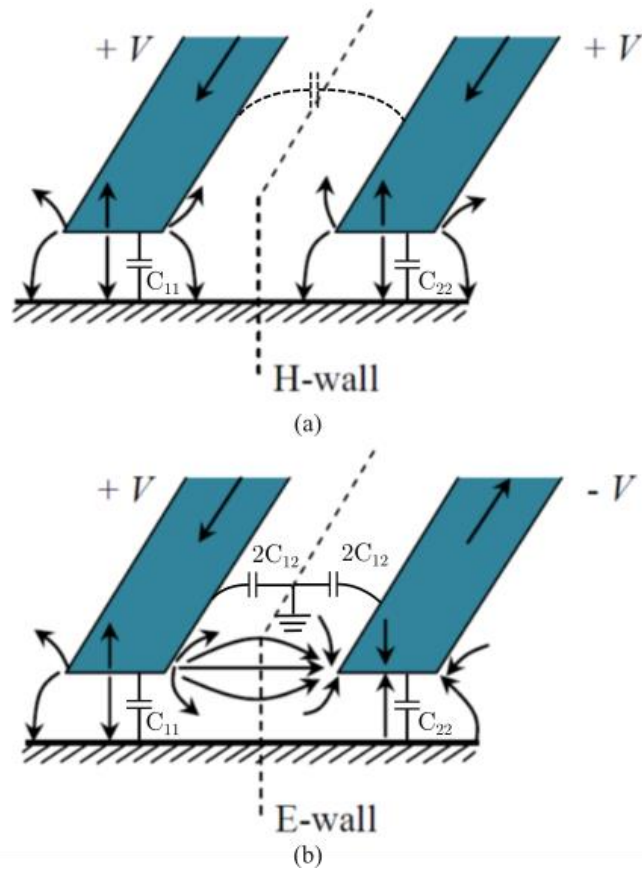
Figure 2.13 (a) Even-mode (b) Odd-mode, excitation for a coupled-line and its equivalent capacitance networks[11].

In the even mode excitation, there should be no current flowing between coupled lines, this is modelled by a perfect magnetic (H) conductor wall between the coupled lines. This is no different than separating the coupled lines so that capacitive coupling between lines disappears, thus the equivalent capacitor is marked as dashed in Figure 2-13a. Odd mode, on the other hand, implies that coupled lines behave as a differential transmission line, therefore, a perfect electric (E) conductor wall is assumed to be present between lines. This wall ensures that the equivalent capacitors modelling the capacitive coupling between coupled lines are connected to each other at the middle of the lines, and voltage of this point is equal to that of the ground. Assuming the two conductors are symmetrical, the even and odd-mode characteristic

impedances, Z_{0e} and Z_{0o}, can be written in terms of resulting capacitance C_e and C_o for even and odd-mode as [13]:

$$Z_{0e} = \sqrt{\frac{L}{C_e}} = \frac{1}{v_p C_e} \qquad (2.18a)$$

$$Z_{0o} = \frac{1}{v_p C_0} \qquad (2.18b)$$

where $C_e = C_{11} = C_{22}$, $C_0 = C_{11} + 2C_{12} = C_{22} + 2C_{12}$ and v_p is the phase velocity of the line. In pure TEM propagating structures, both E and H fields are always in the transverse plane. However, this is not the case for microstrip transmission lines, since fields are not contained in a single dielectric medium. Assuming substrate material is not the same as to the region above the strip, fields are contained in two different media with different dielectric constants. Then, the phase velocities of the fields contained in each material will be different, which breaks the transverse nature of the E and H fields. However, the longitudinal component that breaks the TEM behaviour is often too small to have a significant effect, so it can be assumed that the propagating mode is similar to the quasi-static behaviour of the transmission line. Therefore, the propagating mode in a transmission line is called quasi-TEM mode [11]. For a coupled transmission line supporting TEM mode, these capacitances can be calculated analytically, whereas it is calculated numerically for quasi-TEM lines, as quasi-TEM requires a more comprehensive solution compared to pure TEM mode, caused by the different phase velocities in different media [23, 24]. Nowadays, calculation of characteristic impedance for either case can be done easily by using commercially available microwave CAD packages. These CAD packages solve the characteristic impedance by using either an approximate analytical solution, or from the ratio of numerically calculated E and H fields.

2.6.2 Parallel Coupled-line Filters

Many types of filters can be designed using parallel coupled transmission lines. Bandpass or bandstop coupled-line filters with a fractional bandwidth of less than 20% can be realised by cascading parallel coupled-line. The major drawback of such a filter is that wide bandwidth cannot be obtained since it requires closely coupled-lines, which are very difficult to realize using microstrip transmission lines. Parallel coupled-lines can be defined as a four-port network where the open circuit impedance matrix for such network is acquired through superposition of even and odd-mode excitations. Since only two ports are required for filter design, the remaining two ports can be terminated in open circuit to have a bandpass filter response as shown in Figure 2.14 [23].
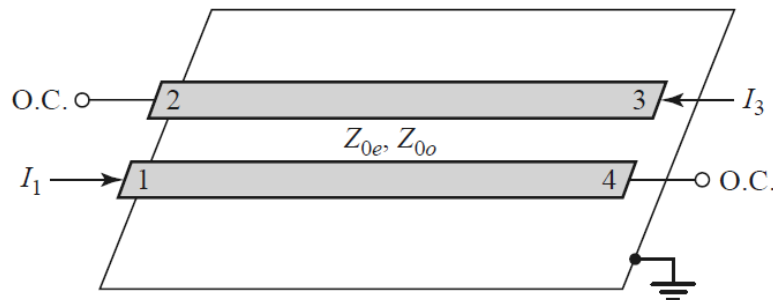
Figure 2.14 A parallel coupled line section having a bandpass response [11].

If the coupled lines are solved for port impedances using even-odd mode analysis, it is observed that bandpass response is obtained when currents at ports 2 and 4 are zero[11] . This can be achieved by leaving these port as open circuit. By cascading coupled line segments, one can get even sharper bandpass responses. Figure 2.15 shows the frequency response of a 3rd order open circuited coupled line bandpass filter.
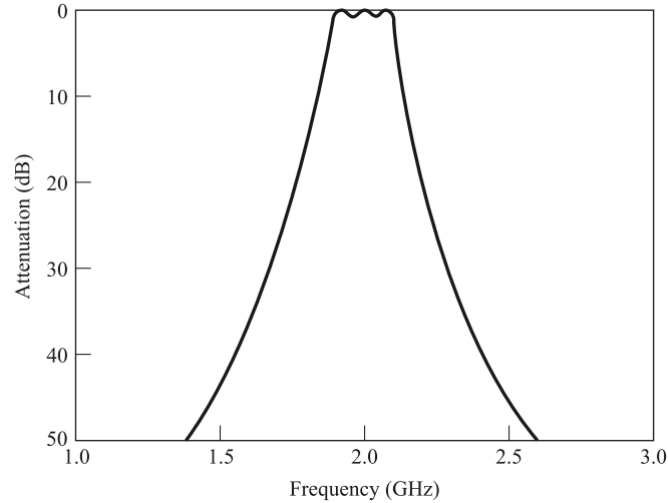
Figure 2.15 Frequency-magnitude response of a 3rd order coupled line bandpass filter [11].

The passband and stopband characteristic of the filter mentioned in Figure 2.14 can be determined by calculating the image impedance at port 1 or 3. The image impedance can be denoted in terms of odd and even mode impedances as [11]:

$$Z_i = \frac{1}{2}\sqrt{(Z_{0e} - Z_{0o})^2 csc^2\theta - (Z_{0e} - Z_{0o})^2 cot^2\theta} \qquad (2.19)$$

When the electrical length of the coupled-line section is $\theta = \pi/2$, it can be seen that the value of the image impedance is real, which indicates a passband. However, when $\theta = 0$ or π, the value of image impedance is imaginary, which refers to the stopband of the filter.

2.7 Coupled Resonator Filter

Microstrip square ring resonator is one type of resonators that can be employed to design narrowband RF/microwave filters [10]. Different orientations of open-loop square ring resonators results in three different coupling structures as shown in Figure 2.16. Each of the open-loop resonators is essentially a folded half-wavelength resonator. The maximum electric coupling in a single resonator is observed at the side of the open-gap because electric fringe fields are stronger at the side having the maximum electric field distribution. In contrast,

maximum magnetic coupling is realised at the opposite side since magnetic fringe fields are stronger near the side having the maximum magnetic field distribution. Maximum electric coupling is achieved when the sides of the open-gap are positioned close to each other as shown in Figure. 2.16(a). Likewise, magnetic coupling can be attained if the sides with the maximum magnetic field of the two coupled resonators are nearly located as shown in Figure. 2.16(b). Finally, both electric and magnetic coupling can be observed when the resonators are placed as seen in Figure 2.16(c,d), which can be referred to as mixed coupling.
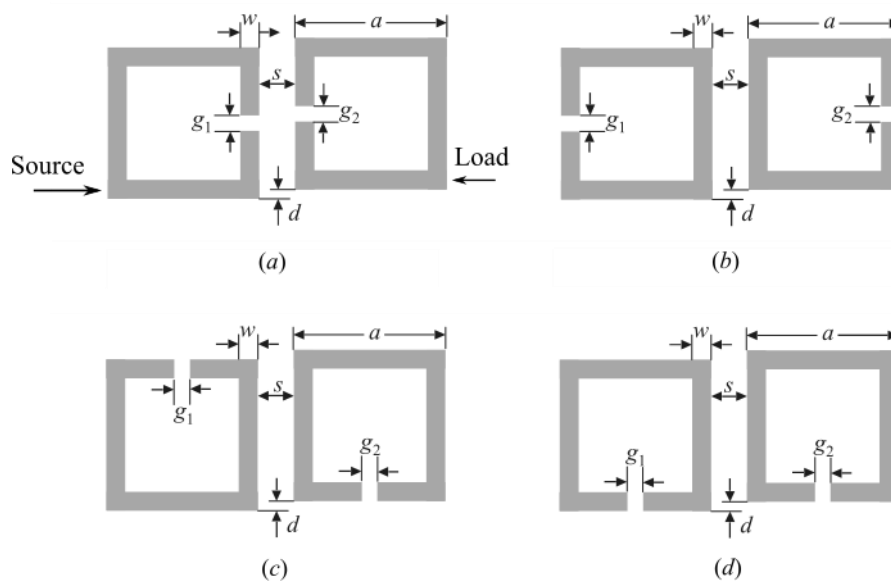
Figure 2.16 Coupling Structures of coupled square open-loop resonators with (a) electric coupling (b) magnetic coupling, and (c,d) mixed coupling [10]

An equivalent circuit model for electrically coupled resonators is presented in Figure 2.17, where L, C, and C_m denote the self-inductance, self-capacitance and mutual capacitance between resonators respectively. Therefore, the resonant frequency of the uncoupled resonator is equal to $(LC)^{-1/2}$. If the symmetry plane of such a circuit model is short-circuited, the resonant frequency of the resultant circuit is:

$$\omega_e = \frac{1}{\sqrt{L(C+C_m)}}$$

(2.20)

51

The resonant frequency is lower than of the uncoupled resonator because the coupling effect improves the ability of a single resonator to store charge if odd mode circuit is considered. On the contrary, the resonant frequency is increased if even mode circuit is, which is defined by:

$$\omega_m = \frac{1}{\sqrt{L(C-C_m)}}$$

(2.21)

Thus, the electric coupling coefficient can be defined using equations (2.20) and (2.21) [10] as:

$$k_E = \frac{\omega_m^2 - \omega_e^2}{\omega_m^2 + \omega_e^2} = \frac{C_m}{C}$$

(2.22)

It can be observed here that k_E is equal to the coupled electric energy divided by the stored energy of uncoupled single resonator. It is worth mentioning here that the energy stored on a capacitor can be determined by $E = \frac{1}{2} CV^2$ where C is the capacitance value and V is the voltage.
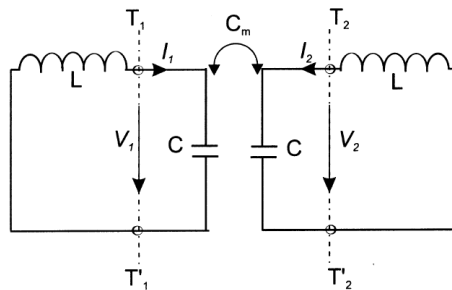
Figure 2.17 An equivalent circuit model for coupled resonator circuit with electric coupling [10].

Magnetic coupling can be explained by considering the equivalent circuit model for a magnetically coupled resonator shown in Figure 2.18. Self-inductance and self-capacitance are denoted by L and C, whereas mutual inductance is represented by Lm. Similarly, replacing the symmetry plane by a short-circuit and an open-circuit respectively will result in two resonant frequencies as given below:

$$\omega_e = \frac{1}{\sqrt{C(L-L_m)}}$$

(2.23)

$$\omega_m = \frac{1}{\sqrt{C(L+L_m)}} \qquad (2.24)$$

Magnetic coupling coefficient can be calculated using equations (2.23) and (2.24) as

$$k_M = \frac{\omega_e^2 - \omega_m^2}{\omega_e^2 + \omega_m^2} = \frac{L_m}{L} \qquad (2.25)$$

It can be seen that k_M is equal to the coupled magnetic energy divided by the stored energy.
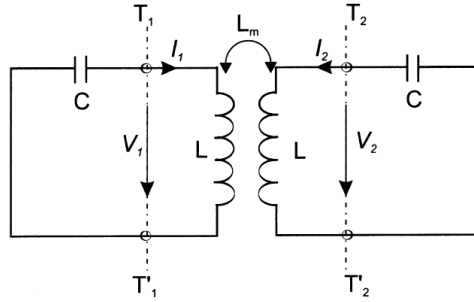
Figure 2.18 Equivalent circuit model for a magnetically coupled resonator structure [10]

In the mixed coupling structure, both electric and magnetic couplings are considered to find the resonant frequencies of the structure. Similarly, replacing the symmetry plane by short-circuit and open-circuit respectively, the resonant frequencies of the mixed coupled resonator can be obtained as

$$\omega_e = \frac{1}{\sqrt{(C-C_m)(L-L_m)}} \qquad (2.26)$$

$$\omega_m = \frac{1}{\sqrt{(C+C_m)(L+L_m)}} \qquad (2.27)$$

where L and C represent self-impedance and self-capacitance. C_m and L_m represent the mutual capacitance and mutual inductance between resonators. The mixed coupling coefficient can be defined using equations (2.26) and (2.27) as:

$$k_x = \frac{\omega_e^2 - \omega_m^2}{\omega_e^2 + \omega_m^2} = \frac{CL_m + LC_m}{LC + L_m C_m} \qquad (2.28)$$

Assuming that $L_m C_m \ll LC$, equation (2.28) reduces to:

$$k_x = \frac{L_m}{L} + \frac{C_m}{C} = k_M + k_E \qquad (2.29)$$

This shows that the mixed coupling is the superposition of the magnetic and electric couplings. In [10], an eight-pole microstrip filter shown in Figure 2.19 is designed using coupled open loop resonator. The fractional bandwidth of the filter is almost 10% and the centre frequency is 985 MHz. Coupling coefficients for this structure are calculated using the formulas mentioned in [10]. The filter was designed using a substrate with relative dielectric constant of 10.8 and a thickness of 1.27 mm. The size of the filter is 120 mm ×50 mm which is relatively large and the electrical size of such filter can be easily reduced using metamaterial structures as will be seen in the next chapter [24].
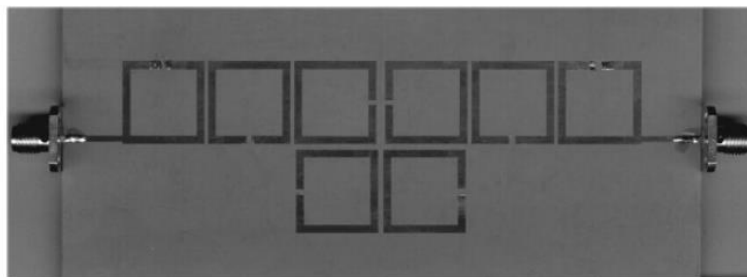
(a)
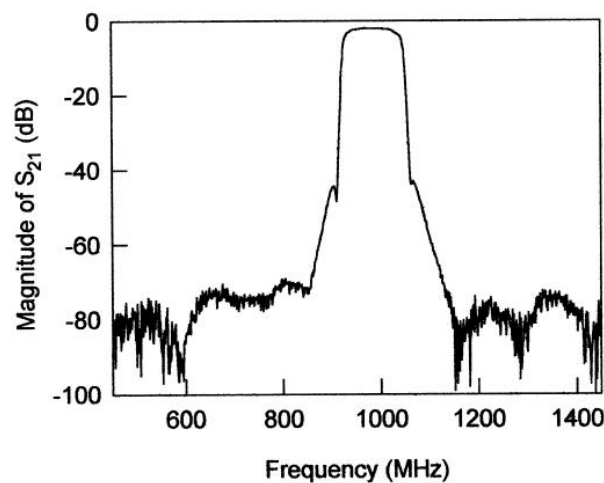
(b)

Figure 2.19 (a) Picture of the designed eight-pole bandpass filter. (b) Measured frequency response[10]

2.8 Chapter Summary

This chapter is intended to provide a brief introduction to filter design theories and techniques and lay out the foundation required to design filters using CRLH TL. Coupled-line and coupled resonator are two of the main building blocks for many bandpass filter designs available in the literature and the theories behind such structures need to be carefully reviewed. In communication systems, filters are mainly used to select desired frequencies or supress unwanted frequencies. They can be classified into three main categories: active, passive, and hybrid, where each kind has its own advantages considering filter specification requirement for different application. The main focus of this research will be on passive filters because of ease of fabrication and lower cost. Such filters are characterised and designed using transmission lines where filter parameters such as bandwidth, insertion loss, return loss and selectivity are used to analyse the filter performance.

Network parameters such as S, Z, Y and ABCD parameters are presented in this chapter and will be used to simplify the analysis of filters designed using CRLH TL. Transmission lines that have been periodically loaded with reactive element are defined as periodic structures. Such structures inherently have filtering properties and can be mainly realized by introducing a discontinuity in the line. Historically, two main approaches are used to design filter which are image parameter method (IPM) and insertion loss method (ILM). ILM is more preferable since it's capable of providing desired frequency response whereas only centre frequency and attenuation characteristic can be specified using IPM. These conventional methods proved to be useful in filter design and filter performance can be easily enhanced by increasing the order of the filter at the expense of larger circuit size. In the following chapter, metamaterials are introduced and used to design filters with better performance and smaller size than conventional filters.

Chapter 3: Metamaterials

3.1 History of Metamaterials and Left-Handed Metamaterials

Electromagnetic metamaterials (MTM) are artificial electromagnetic structures with special properties that cannot be found in nature [1]. The structural cell size p should be at least smaller than a quarter of guided wavelength λ_g to meet the effective homogeneity condition as shown in Figure 3.1.
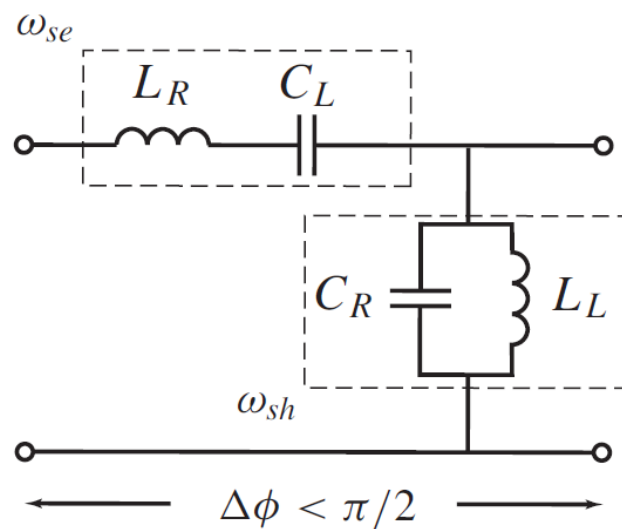
Figure 3.1 MTM transmission line unit cell.

This condition ensures refraction dominates over scattering or diffraction for reliable wave propagation inside the MTM media. When this condition is met, the structure can be seen as a material with constitutive parameters of electric permittivity ε and permeability μ, where it is electromagnetically uniform along the direction of propagation [2]. The refractive index n can be defined in terms of the constitutive parameters ε and μ as[1]:

$$n = \pm\sqrt{\varepsilon_r \mu_r} \tag{3.1}$$

Where ε_r and μ_r are the relative permittivity and permeability respectively, which are associated with free space permittivity and permeability by $\varepsilon_0 = \frac{\varepsilon}{\varepsilon_r} = 8.854 \times 10^{-12}$ (F/m) and $\mu_o = \frac{\mu}{\mu_r} = 4\pi \times 10^{-7}$ (H/m) [1]. It can be concluded from (3.1) that the sign for (ε, μ) can be (+,+), (+,-), (-,+) and (-,-) as shown in Figure 3.2. The first quadrant of ε- μ diagram corresponds to the conventional right-handed material with forward wave propagation. When either ε or μ is less than zero, the wave cannot propagate because the negative sign for either ε or μ results in an imaginary propagation constant ($\beta = nk_0$ (rad/m) where $n = \pm\sqrt{\varepsilon_r \mu_r}$, $k_0 = \omega\sqrt{\varepsilon_0 \mu_o}$) and stopband can be observed [25]. The fourth quadrant in Figure 3.2 represents left-handed (LH) material where $\varepsilon = \varepsilon_r \varepsilon_0$ and $\mu = \mu_r \mu_o$ are simultaneously negative. Such materials can be identified by antiparallel phase and group velocities because of their double negative parameters [1].

In 1967, Viktor Veselago predicted the existence of LH MTM that allows backward wave propagation [3]. This prediction was confirmed three decades later by Smith [4], where he proposed a structure consisting of a periodic array of split ring resonators and continuous thin wires shown in Figure 3.3 that allow wave propagation at a certain frequency region with negative- ε and negative-μ.
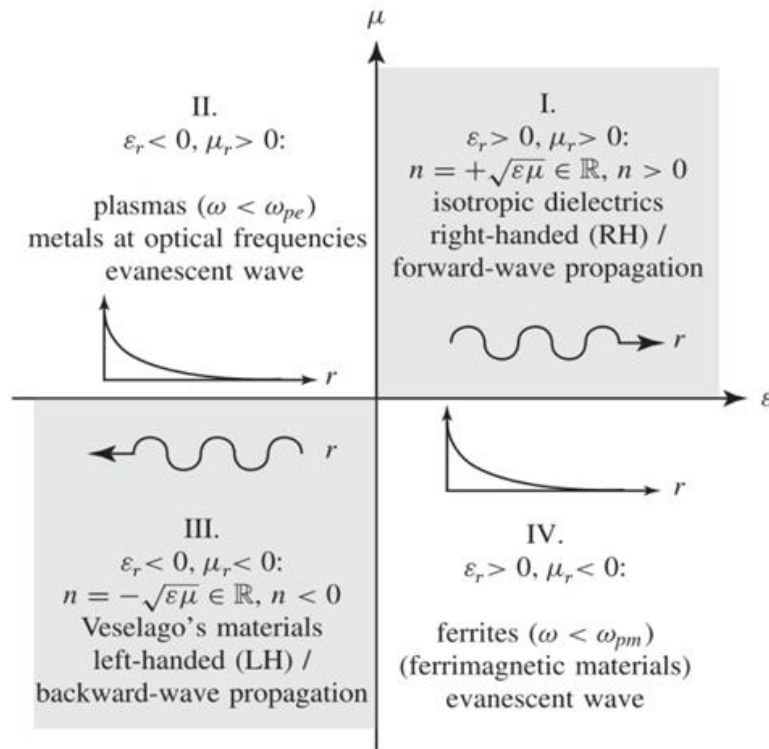
Figure 3.2 Permittivity-permeability (ε- μ) diagram where the sign of refractive index (n) is controlled by ε and μ[1].
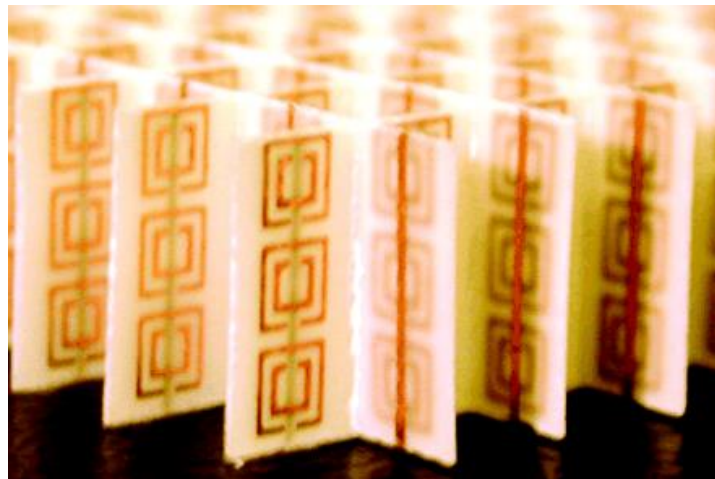
Figure 3.3 LH MTM consisting of square split resonators and copper wire strips [26].

After Smith's breakthrough, the research on LH MTM continued and different theoretical and experimental approaches were used to verify the backward wave propagation in LH MTM. The

LH structure presented in Figure 3.2 was inspired by Pendry's work in [27, 28] and can be considered as a resonant type structure that suffers from high loss and exhibits narrow bandwidth. Therefore, transmission line approach of MTM was presented by Caloz in [5, 6] to solve the problems of the resonant type structure presented by Smith. In the next section, it will be shown that TL approach of MTM is preferred since classical TL theory can be used to design and analyse LH MTM.

3.2 Transmission Line Approach

The main characteristic of the LH TL is the antiparallel phase and group velocities, which can be easily verified when considering the incremental circuit model for a lossless LH TL shown in Figure 3.4.
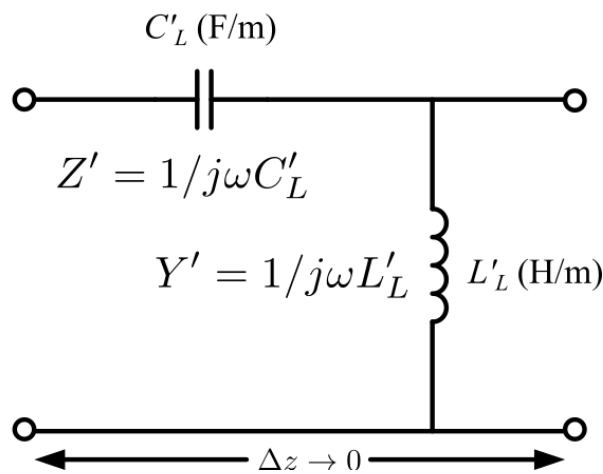
Figure 3.4 The "incremental circuit model for a hypothetical uniform LH TL" [1]

The complex propagation constant γ, for the above lossless transmission line is given by [1]

$$\gamma = j\beta = \sqrt{Z'Y'} = \frac{1}{j\omega\sqrt{L'_L C'_L}} = -j\frac{1}{\omega\sqrt{L'_L C'_L}} \tag{3.2a}$$

where β is the propagation constant and the phase and group velocities can be expressed as:

$$v_p = \frac{\omega}{\beta} = -\omega^2\sqrt{L'_L C'_L} \tag{3.2b}$$

$$v_g = \left(\frac{\partial \beta}{\partial \omega}\right)^{-1} = +\omega^2 \sqrt{L'_L C'_L} \qquad (3.2c)$$

It can be concluded from the above equations that phase propagation (β) is in the opposite direction of the power flow, which proves the TL of Figure 3.3 is LH. For practical design of LH TL, the average cell size *p* should be much smaller than the guided wavelength *λg*. Satisfying such condition, allows the realization of LH medium in a certain frequency range. The first microstrip LH TL structure was presented by Caloz et al. in [29], which consisted of a series interdigital capacitor and short-circuited shunt stub inductors. One of the main benefits of TL MTM is that it can achieve low loss by designing a balanced structure and minimising the mismatch between the input and output ports. Also, broad bandwidth can be attained by adjusting the TL constitutive LC parameters. Moreover, Integration with other passive and active RF/microwave components is easy since TL MTM structures can be realised in planar configuration.

3.3 Ideal Composite Right/Left-Handed (CRLH) TL

The series capacitor C_L and shunt inductor L_L are needed to realise a LH TL as shown in Figure 3.3, but wave propagation through the structure introduces series inductance and shunt capacitance parasitic effect. Magnetic flux can be induced when the current flows along the series capacitor C_L, which resembles the existence of a series inductor L_R. Also, a shunt capacitor C_R is present due to the existence of voltage gradient, i.e electric field E, between upper conductors and ground [1]. Since the contribution of right-handed (RH) conventional TL elements L_R and C_R cannot be disregarded, it is impossible to realise a purely LH (PLH) TL structure, and the term composite right/left-handed (CRLH) is a general term used to describe LH structure.
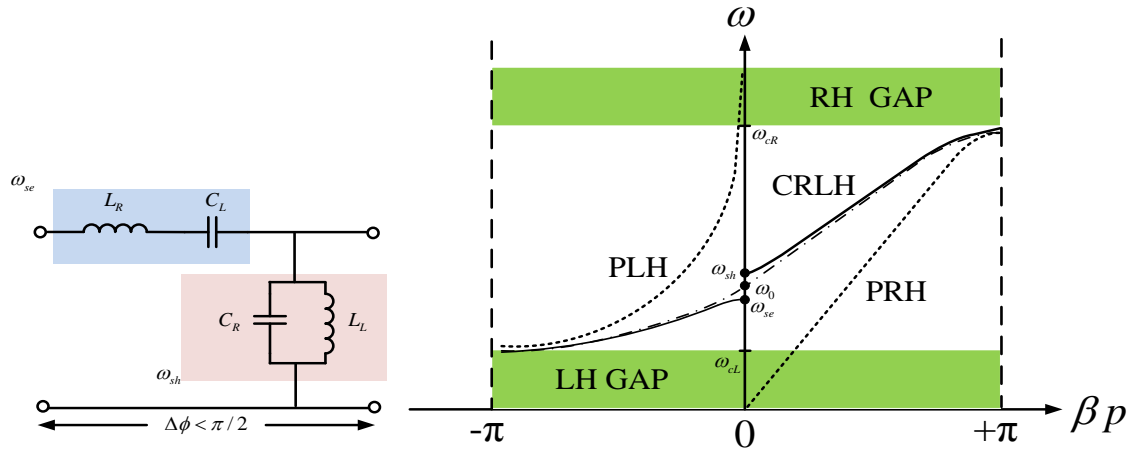
Figure 3.5 Characteristics of CRLH TL. (a) Circuit model for unit cell TL. (b) Dispersion diagram for CRLH, PLH, PRH structures [1].

CRLH TL structure can be studied using the equivalent circuit model in Figure 3.5(a). At low frequencies, series inductance L_R and shunt capacitance C_R can be interpreted as short and open circuit respectively. So the remaining series capacitance C_L and shunt inductance L_L can be regarded as a high-pass filter with a cut-off frequency ($\omega_{CL} = 1/\sqrt{L_L C_L}$, (rad.m)/s). At high frequencies, only the RH elements (L_R, C_R) are taken into account in the equivalent circuit since LH elements (C_L, L_L) can be considered as short and open circuit respectively. Therefore, the resulting circuit acts as low-pass filter with cut-off frequency ($\omega_{CR} = 1/\sqrt{L_R C_R}$, (rad.m)/s) where only RH elements are considered (L_R, C_R). The transmission characteristics of CRLH TL are determined by considering the effects of RH and LH elements at all other frequencies. Therefore, CRLH TL has bandpass response due to the existence of RH and LH elements.

From the dispersion diagram for CRLH TL in Figure 3.5(b), it can be seen that attenuation occurs at a certain range of frequencies within the passband when shunt resonance ($\omega_{sh} = 1/\sqrt{L_L C_R}$) and series resonance ($\omega_{se} = 1/\sqrt{L_R C_L}$) are different, which refers to the case of unbalanced CRLH TL. On the other hand, when the transition frequency $\omega_0 = \omega_{se} = \omega_{sh}$,

balanced CRLH TL can be realised and an infinite wavelength ($\lambda_g = 2\pi/|\beta|$) is attained at ω_0 [1]. The cases for balanced and unbalanced CRLH TL are discussed in the following section.

3.3.1 Balanced and Unbalanced CRLH TLs

The properties of balanced and unbalanced resonance observed in CRLH TL are both useful in filter design. For example, ultra-wide bandpass filter (BPF) can be constructed using one unit cell of balanced CRLH TL [30] where dual-band BPF can be realized using the unbalanced case[31]. Both cases can be examined by considering the characteristic impedance Z_c of the CRLH TL unit cell defined as[1]:

$$Z_c = Z_L \sqrt{\frac{(\omega/\omega_{se})^2 - 1}{(\omega/\omega_{sh})^2 - 1}} \tag{3.3a}$$

$$\begin{cases} Z_c[0 < \omega < \min(\omega_{se}, \omega_{sh})] \in \mathbb{R} \text{ (LH pass band)}, \\ Z_c[\min(\omega_{se}, \omega_{sh}) < \omega < \max(\omega_{se}, \omega_{sh})] \in I \text{ (gap for unbalanced case)}, \\ Z_c[\omega > \max(\omega_{se}, \omega_{sh})] \in \mathbb{R} \text{ (RH pass band)}. \end{cases} \tag{3.3b}$$

where $Z_L = \sqrt{\frac{L_L}{C_L}}$ is the impedance of purely LH TL. It can be seen from (3.3a) when $\omega = \omega_{se}$ or $\omega = \omega_{sh}$, a zero and a pole will be introduced in the characteristic impedance which results in a zero group velocity or stopband. Unbalanced CRLH TL can be only matched in a certain frequency range since Z_c is a function of frequency, whereas balanced CRLH TL can be matched over an infinite frequency band because Z_c ideally becomes frequency independent when ($\omega_{se} = \omega_{sh}$). Moreover, propagation constant of PRH and PLH TL can be added to obtain the propagation constant of balanced CRLH TL.

Non-zero group velocity at the transition frequency ω_0 is one of the remarkable properties of a balanced CRLH TL. Propagation is supported at this frequency while propagation constant $\beta = 0$. Hence, phase origin is defined at ω_0. This can be easily understood by calculating the

phase shift along the TL with physical length l, i.e. $\emptyset = -\beta l = 0$. Phase behaviour in CRLH

TL is different than conventional RH TL. Below ω_0, phase shift is positive and reaches positive

∞ as frequency approaches zero: $\emptyset(\omega \to 0) = -\beta d \to +\omega_{CL}.(l/\omega)$. In the other hand, phase

becomes negative as frequency increases above ω_0 and reaches negative ∞ at very high

frequencies: $\emptyset(\omega \to \infty) = -\beta d \to -\omega.(l/\omega_{CR})$ [1]. Guided wavelength shows different

behaviour in CRLH TLs when compared to RH TLs. As shown earlier, $\lambda_g = \infty$ at ω_0 and it

becomes smaller at frequencies $(\omega < \omega_0)$ or $(\omega > \omega_0)$.

3.3.2 LC Network Implementation

Ladder networks consisting of LC unit cells can be used to realize CRLH TL since it's not

readily available in nature. These networks are operative in a restricted frequency range as long

as effective homogeneity condition is met. The operational frequency range or bandwidth for

these networks can be easily controlled by the LC parameter values. It worth mentioning here

that bandwidth obtained using TL approach of MTM is larger than that of resonant approach

mentioned before (i.e. TW-SRR)[1]. Hence, appropriate number of LC unit cells N is repeated

to obtain a TL with total length of l as shown in Figure 3.6. Assuming the structural average

cell size p is very small, ideal CRLH TL can be represented by NLC unit cells to ensure

homogeneity condition. This condition is needed to avoid resonance along the discontinuities

of the lines. Although, CRLH TL is generally implemented in periodic configuration due to its

design simplicity, non-periodic implementation of CRLH TL unit cell exist [32]. Additional

degree of freedom is usually associated with non-periodic structure at the expense of higher

design complexity.
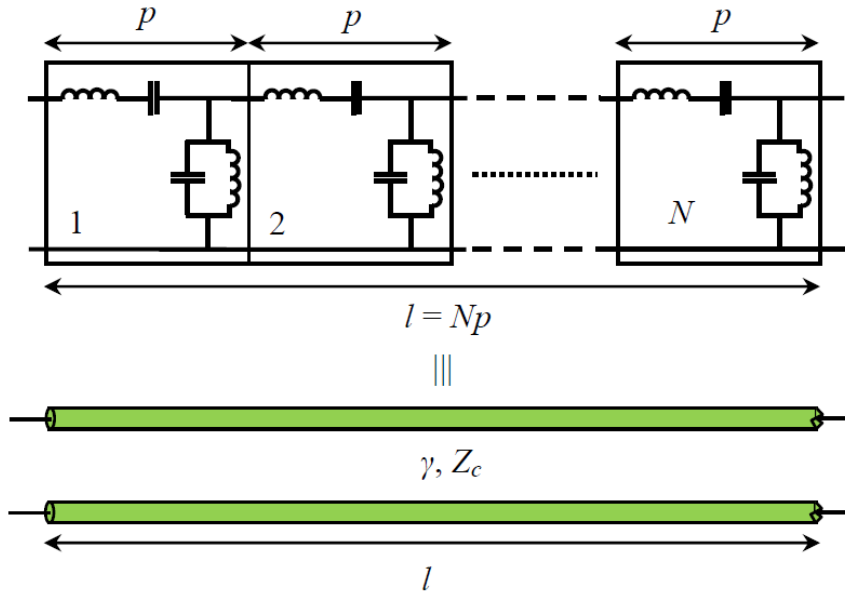
Figure 3.6 Equivalent periodic LC network for an ideal TL with length l assuming effective homogeneity condition; $p = \Delta z \to 0$.

3.3.3 Comparison between conventional bandpass filters and CRLH TLs

Filtering characteristic obtained by the use of CRLH TLs is quite similar to conventional bandpass filters. One important characteristic of filters is the sharp roll-off rate which can be attained by increasing the filter order in conventional filter. Similarly, increasing number of unit cells in CRLH TL has similar effect [1]. However, major differences between these two are obtained when studied thoroughly[1]. These distinctions are mentioned below:

- Homogeneity condition (i.e. $\Delta z << \lambda_g$) is not satisfied in conventional filters, whereas unit cell of CRLH TL must satisfy this condition.

- Conventional filters can be realized only as a 1D structure, while CRLH TL based structures can be 2D or 3D and behave as a bulk media.

- Conventional filters are mainly designed according to magnitude specifications, whereas LH structures are generally designed to meet certain phase specifications. Thus, RH and LH transmission can be only observed in LH structure.

- Finally, identical unit cells are usually employed in LH structures while each unit-cell in conventional filters has a different LC value to meet certain design specifications.

3.4 Metamaterial Filters

Metamaterial transmission lines can be constructed using different types of sub-wavelength resonator such as split ring resonator (SRR) [27] or complementary split ring resonator (CSRR)[33]. Size reduction is one of the main advantages of such resonators since the dimension of these resonators are much smaller than signal wavelength at resonance. This can be explained by considering a half-wavelength ring resonator. The diameter of the ring is $\lambda/2\pi$ at resonance frequency. To further reduce the size of the split ring, an inner ring with an opening on the opposite side can be added. Due to the mutual coupling between the two rings, the resonant frequency of the SRR is lower than the resonant frequency of any of the individual rings which translates to an electrical size smaller than a single ring resonator [34]. A propagation medium is obtained when electrically small resonators are combined with series capacitance or shunt inductance to load a transmission line [35]. The impedance and phase of such lines can be modified which is useful for designing RF and microwave passive components such as filters, couplers, and power divider.

Conventional filters suffers from spurious harmonics which can be suppressed using CSRR as mentioned in [36]. By properly tuning the CSRRs, wide upper stopband can be realized while maintaining similar filter size due to the possibility of etching CSRRs in the ground plane. It is true that CSRRs are widely used as stopband filter but it is also useful for BPF design and a good example is presented in [37]. The unit cell of the resonant-type MTM TL contains CSRRs etched on the bottom layer and capacitive gaps etched on the top layer as shown in Figure 3.7(a). Obtaining an equivalent circuit model for this unit cell is beneficial in understanding its

electrical characteristics. In [38], an equivalent circuit model for this unit cell is obtained as shown in Figure 3.7(b) where L denotes the inductance of the microstrip line and CSRR is represented by L_c and C_c. A transmission zero is generated at DC frequency due to the effect of the capacitor C_s which represents series capacitance.

Combining both right/left-handed unit cells is one of the approaches to design narrowband BPF as mentioned in [39-41]. Sharp selectivity is obtained when two left-handed unit cells are combined with one right-handed unit cell as shown in Figure 3.8.

(a)   (b)
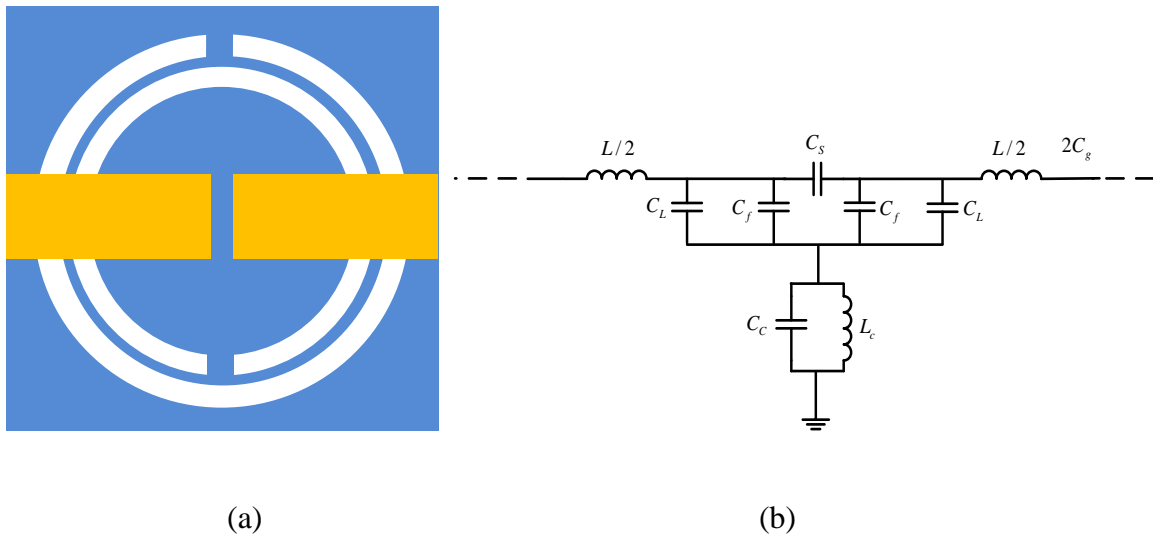
Figure 3.7 Layout of a MTM TL unit cell based on CSRR [37]. (b) Equivalent circuit model for the MTM TL unit cell based on CSRR [38].
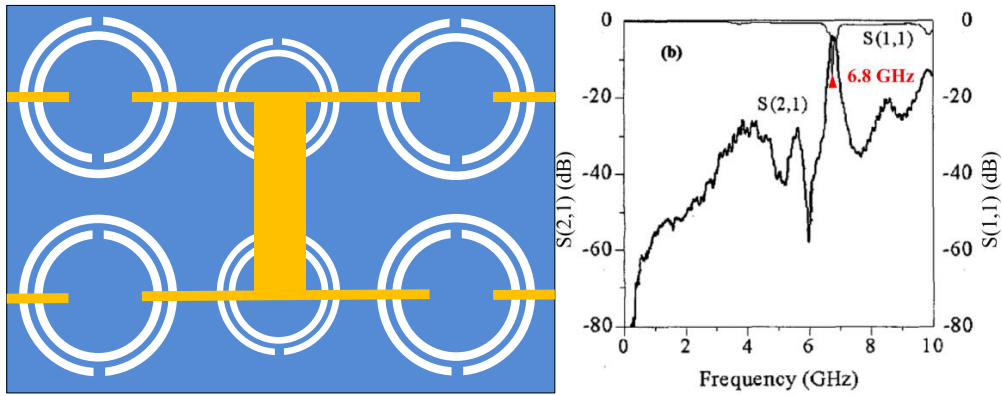
Figure 3.8 (a) Layout of the BPF combining one RH and two LH SRR-based coplanar unit cells. (b) Measured S_{11} and S_{21} for the bandpass filter [39].

Compared to conventional parallel coupled-line filter, the proposed filter in Figure 3.8(a) has a narrowband frequency response and compact size. CSRR-based balanced transmission line can be employed to design ultra-wideband (UWB) BPF [42, 43] since broad-band response can be obtained. Three CSRR unit cells are utilized to design an UWB BPF in [35] which is suitable for UWB communication systems operating at frequency range from 3.1 to 10.6 GHz. Since poor upper stopband performance can be obtained using these unit cells, additional small CSRRs are needed to improve the rejection profile within the upper stopband as shown in Figure 3.9(a). The simulation results show that the filter has a broad bandpass response with acceptable insertion loss but poor rejection level within the upper stopband as seen in Figure 3.9(b).

(a)
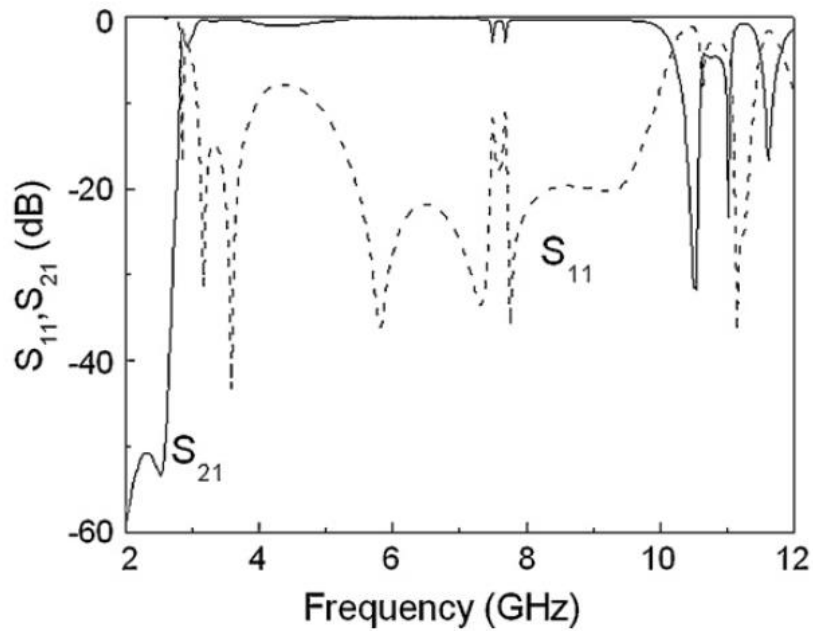
(b)

Figure 3.9 (a) A layout of an UWB bandpass filter based on CSRR balanced unit cells. (b) Simulated results of the UWB BPF mentioned in (a)[35].

Many wireless communication systems operate within the UWB passband and radio signals from such systems are considered as interfering signals that need to be rejected. Unwanted signals are rejected using complementary spiral resonators (CSRs) shown in Figure 3.10 [24] without increasing the circuit size by etching CSRs in the ground plane. There are many different kinds of MTM TL, other than SRR based resonators, that can be utilized to design compact and high performance filters. CRLH TL based structure is another approach that can be employed in filter design. Dual-band BPF design using CRLH TL is presented in [44].

Conventional BPF was firstly designed using quarter-wave grounded stubs which operate at the designed centre frequency and its odd harmonics. Passband separation by a factor of three is not useful for dual-band BPF design and this limitation can be tackled by replacing the grounded stubs with CRLH TL. Two arbitrary frequencies can be chosen using CRLH TL where the separation between them is determined according to the nonlinear phase response of the CRLH TL.
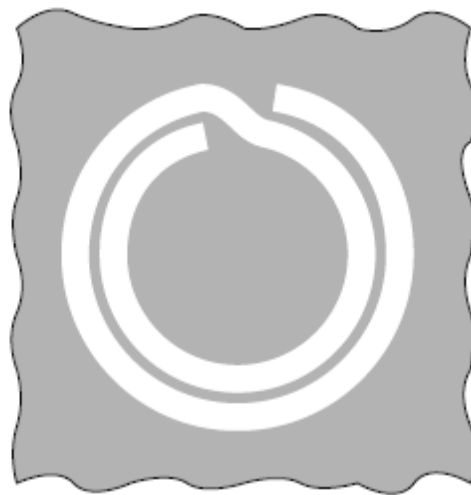
Figure 3.10 layout of complementary spiral resonator (CSR) [45].

3.4.1 Miniaturized UWB BPF Based on CRLH TL-TL Unit Cell.

UWB BPF design caught the attention of many researchers from academia and industry since the U.S federal communication commission (FCC) allowed the unlicensed use of the frequency band (3.1-10.6) GHz. The desired specifications for UWB BPF design are: low insertion loss, sharp passband selectivity, high rejection level within the stopbands, and compact size. Small circuit size is needed to guarantee compatibility with the UWB unit. Different methods and structures have been proposed to design UWB BPF. Stub-loaded multi-mode resonator (MMR) was utilized in [46] to construct an UWB BPF. Stepped impedance resonator in parallel with

the three open stubs was used to distribute the resonant modes of the MMR evenly and obtain a broad passband. Moreover, a wide upper stopband is achieved employing two interdigital parallel coupled feed-lines. The proposed filter has low insertion loss and good return loss, but it lacks sharp roll-up and roll-down rates. Combining low pass and high pass structure is one of the approaches suggested to realize UWB BPF [47]. Low pass filter (LPF) was constructed using stepped impedance structure while quarter-wave short circuited stubs are used to realize the high pass filter (HPF). Although the designed filter has good in-band performance, it has large circuit size and poor frequency selectivity. One of the approaches to reduce the circuit size of UWB BPF is presented in [48] where Bridged-T coil was used instead of conventional TL sections required for MMR design. This approach was validated by fabricating the proposed design using glass-based integrated passive device (IPD) technology. Although measurement results of this very compact UWB BPF design show low insertion loss, it suffers from low roll-on/off rates and high fabrication cost when compared to microstrip UWB BPF design.

In this section, an UWB BPF is designed using single CRLH TL unit cell which is cascaded with a LPF based on symmetrical split ring resonators (SSRRs) defected ground structure (DGS) [7, 8]. Interdigital capacitor and grounded stubs were used to realize the series capacitance and shunt inductance of the CRLH TL, respectively as shown in Figure 3.11. Voltage gradient, electric field E, between the TL conductor and the ground accounts for the shunt capacitance and series inductance is realized by the current across the interdigital capacitor [1].
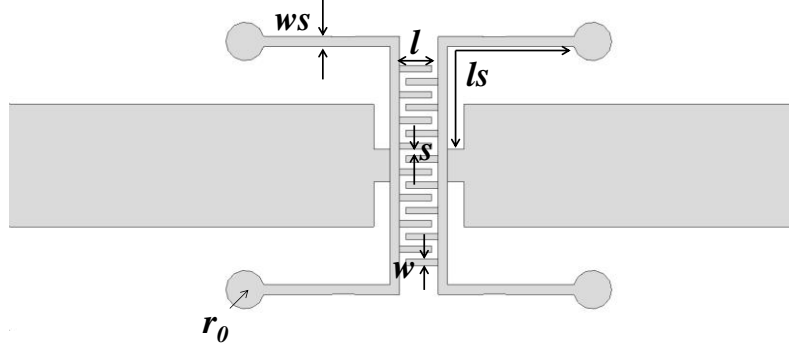
Figure 3.11 layout of the CRLH TL unit cell using interdigital capacitor and four grounded stubs.

Geometric parameters for the CRLH TL unit cell are optimised to meet desired effective capacitance and inductance. The geometry of the interdigital capacitor can be represented by the finger width *(w)*, finger length *(l)*, spacing between fingers *(s)*, and number of fingers *(n)*. The capacitance of the interdigital line can be obtained using the following formula [30]:

$$C(pF) = \frac{\varepsilon_{re} 10^{-3}}{18\pi} \frac{K(k)}{K\prime(k)} (n-1)\lambda \tag{3.4a}$$

$$k = tan^2 \left(\frac{a\pi}{4b}\right), a = \frac{W}{2}, b = \frac{W+S}{2} \tag{3.4a}$$

where ε_{re} refers to the effective relative permittivity of the microstrip finger sections and *K(.)* and *K'(.)* represent the complete elliptic integral of the 1st kind and its complement. The inductance of the short-circuited stubs and each finger can be approximated as [30]:

$$L(nH) = 2 \times 10^{-4} l \left[\ln\left(\frac{l}{W+t}\right) + 1.193 + 0.224\frac{W+t}{l}\right].K_g \tag{3.5a}$$

$$K_g = 0.57 - 0.145\ln(\frac{W}{h}) \tag{3.5b}$$

where *h* and *t* indicate the thickness of the substrate and copper cladding used, respectively. The filter was simulated using Rogers RO3003 substrate with a thickness of 1.52 mm, dielectric constant $\varepsilon_r=3$, and loss tangent = 0.001. CST microwave studio was used to conduct 3D EM simulation. The goals was to design an UWB BPF with $S_{11}=15$ dB, $S_{21}= 1$ dB, f0=6.85 GHz,

71

3dB fractional bandwidth of 100%. The optimised dimensions for the coupled-line are (mm): $ls = 7.2$, $ws = 0.3$, $l=1$, $s=0.2$, $w=0.2$, $r_o=0.6$, $n=16$. The simulation results for the CRLH TL unit cell are presented in Figure 3.12.
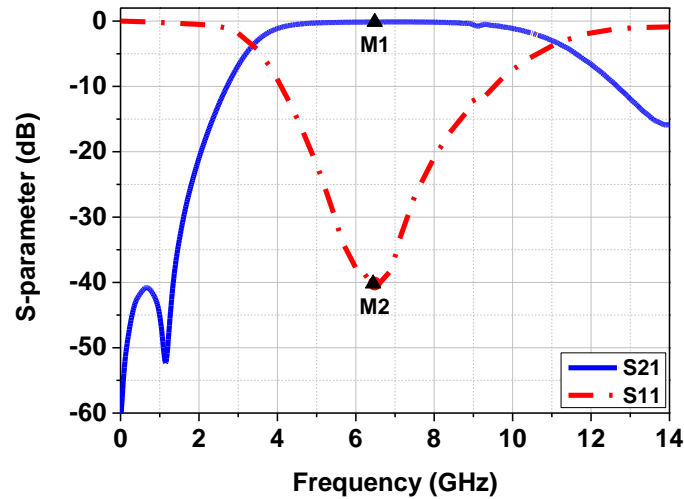
Figure 3.12 Simulated S11 and S21 for the interdigital coupled line where M1= 0.13 dB and M2= 40 dB at 6.46 GHz.

The simulations results shown in Figure 3.12 confirm that the structure has a broad passband from 3.4 to 11 GHz with an insertion loss of 0.3 dB at a centre frequency of 7.2 GHz. The lower cut-off frequency is controlled by varying either the capacitance or the inductance of the CRLH TL. Capacitance of the interdigital capacitor can be varied by changing the number of fingers, spacing between fingers, or the length of the fingers. Similarly, the inductance of the shorted stub depends upon its width and length. Substrate relative permittivity will also have an effect on the interdigital capacitor capacitance. In general, increasing ε_r will reduce the overall circuit size, as higher relative permittivity reduces the guided wavelength of the waves propagating in the microstrip line and reduces the line width required for the same characteristic impedance. Metallization thickness only affect the loss terms, reducing the line thickness increases the attenuation constant of the line. Tuning the lower cut-off frequency is critical in UWB BPF design since most of the frequencies below 3 GHz are licensed by mobile

operators and any violation in fulfilling the rejection level within the lower stopband can cause interference. It is worth mentioning here that the four grounded stubs can be replaced by capacitive patches as shown in Figure 3.13. These patches can provide virtual ground and replace the connection to ground needed in CRLH TL. Fabrication complexity will be reduced when these patches are used which is suitable for large-scale and cost-effective production. The dimensions of the patch can be determined by calculating the quarter wave open stub length first. The stopband should be wide enough, so the stub width should be optimized accordingly. The dimensions for the via-less version of the CRLH TL are (mm): $ls = 6.6$, $ws= 4.3$, $l=2.2$, $s=0.2$, $w=0.2$, $wg=0.4$, $n=14$. One of the drawbacks of using these capacitive patches is the increment of circuit size. Another drawback is the low rejection level within the lower stopband since these capacitive patches act as wide open stubs with a modified shape to obtain proper frequency response at higher frequencies. These capacitive patches are limited in size to obtain a compact UWB BPF design and this restriction degrades the performance of these patches at lower frequencies. The simulation results presented in Figure 3.14 show that the via-less version of the CRLH TL unit cell has similar performance within the passband when compared to the CRLH unit cell presented in Figure 3.11. In this section, the unit cell that utilizes four grounded stubs shown in Figure 3.11 will be used to realize a compact UWB BPF design.
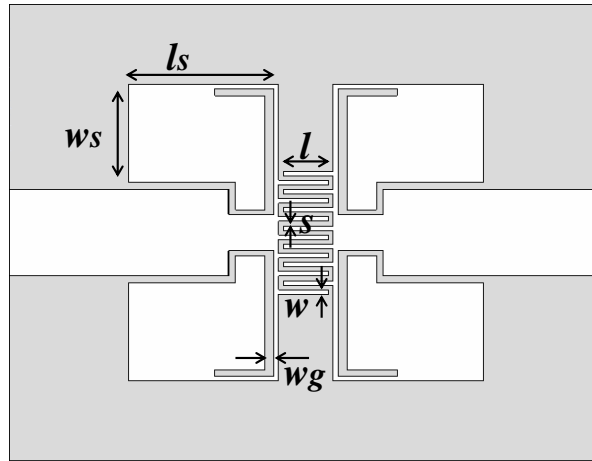
Figure 3.13 Layout of the via-less CRLH TL unit cell.
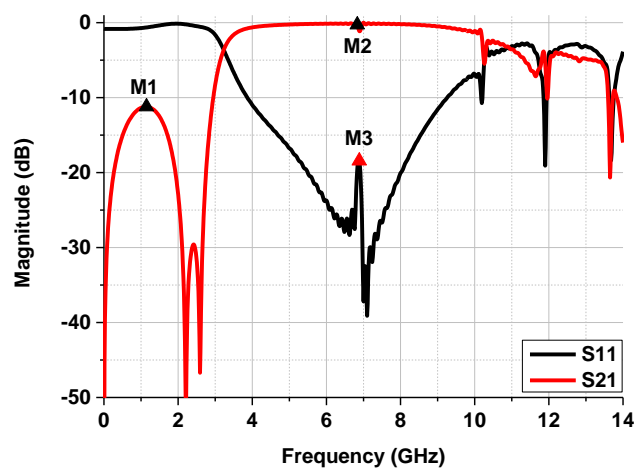
Figure 3.14 Simulation results for the proposed via-less CRLH TL unit cell where M1= 11.22 dB at 1.13 GHz, M2 = 0.28 dB and M3 = 18.43 dB at 6.8 GHz.

Sharp roll-off rate and suppression of harmonics can be attained using LPF based on DGS [49, 50]. Smaller circuit size, sharper roll-off rate, and wider rejection band with two transmission zeros are some of the advantages of SSRR DGS over conventional ones such as dumbbell and SRR [51]. Moreover, broad out-of-band rejection can be achieved by cascading two or three units of the SSRR DGS. This can be easily observed by simulating first a single unit cell of SSRR DGS where a simple microstrip TL was used in the top layer as seen in Figure 3.15. The SSRR DGS based filter was simulated using Rogers RO3003 substrate with a thickness of 1.52

mm, dielectric constant $\varepsilon_r=3$, and loss tangent = 0.001. CST microwave studio was used to conduct 3D EM simulation.
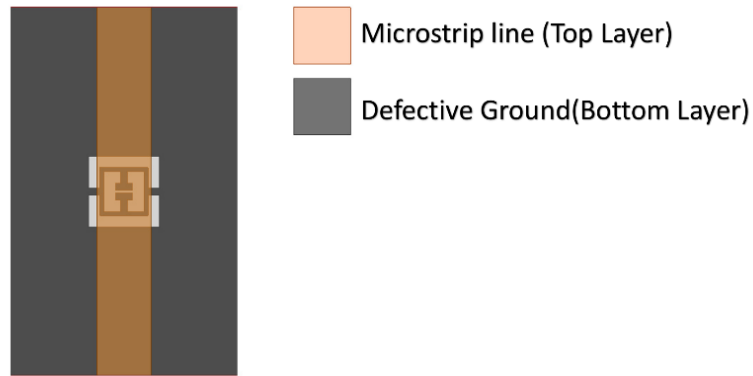
Figure 3.15 Layout of microstrip line with single SSRR DGS unit cell.
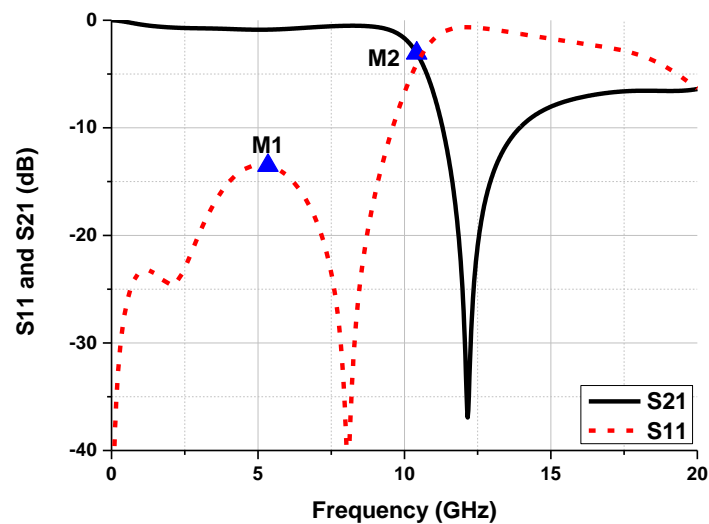
Figure 3.16 Simulated S_{21} for a single SSRR DGS unit cell where M1= 13.48 dB at 5.3 GHz and 3dB cut-off frequency is marked by M2 at 10.4 GHz.

For an UWB bandpass filter application, cascading the CRLH unit cell with SSRR DGS has several benefits. As the upper stopband of CRLH structure does not roll off as sharp as needed,

one can use the bandstop property of SSRR DGS to improve the upper stopband rejection of the overall filter frequency response. Moreover, the band-rejection property of SSRR can also help in rejecting the unwanted bands from the passband, such as rejecting the 5.2 GHz WiFi band. Providing stopbands at the unwanted frequency bands for an UWB bandpass filter has the benefits of reducing gain compression and reciprocal mixing due to high powered unwanted signals, thereby increasing the overall receiver performance[52]. The optimisation goals for the SSRR are : cut-off frequency of 10.6 GHz, S21 less than 1 dB, S11 more than 12 dB and rejection level of 15 dB between 11 GHz and 12 GHz.

The simulation results for a single SSRR DGS unit cell are shown in Figure 3.16 where it can be seen that relatively low roll-off rate and poor out-of-band rejection is obtained. The performance of the LPF can be improved by using two DGS unit cells as seen in Figure 3.17. The passband performance is kept the same where S21 is less than 1 dB and S11 is more than 12 dB. The rejection profile is significantly improved where a sharp roll-off rate is achieved and a rejection level of more than 15 dB is obtained between 11 GHz and 16 GHz.

The optimised dimensions of the SSRRs are (mm) : $a= 5$, $g_1=g_2= 0.5$, $a_1= 2.8$, $s_1= 0.2$, and $w_1=0.8$. It can be concluded from the simulation results shown in Figure 3.18 that the proposed LPF has an in-band insertion loss of less than 1dB with a 3dB cut-off frequency of 9.7 GHz.
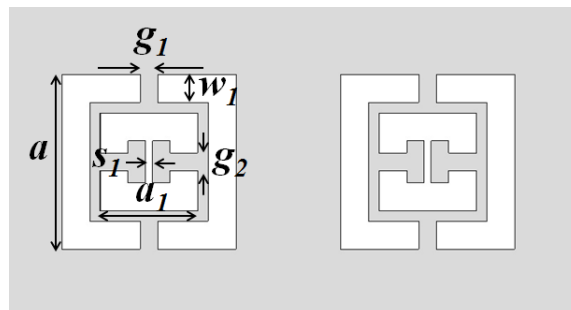
Figure 3.17 Layout of the LPF based on SSRR DGS.
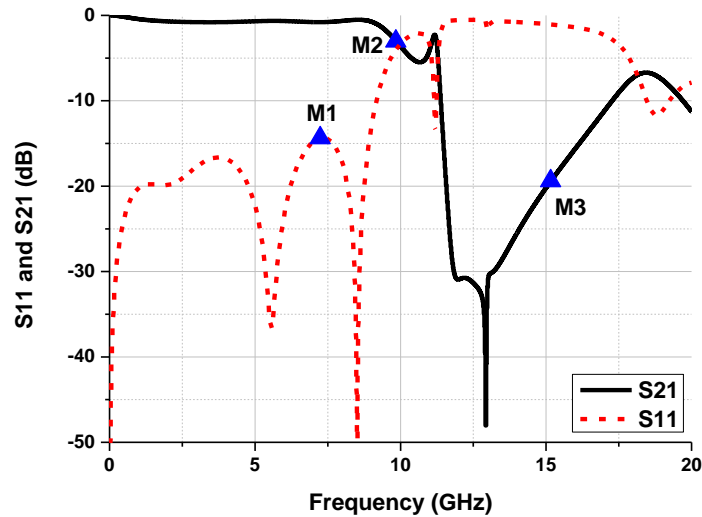
Figure 3.18 Simulated S11 and S21 for the proposed LPF based on SSRR DGS where M1= 14.3 dB at 7.2 GHz, 3dB cut-off frequency is marked by M2 at 9.88 GHz and M3= 20 dB at 15.12 GHz.

The LPF DGS was embedded within the interdigital coupled-line structure to form the proposed UWB BPF as shown in Figure 3.19. A photograph of the fabricated UWB BPF is presented in Figure 3.20. The fabricated filter was measured using Agilent 8510C vector network analyser. Figure 3.21 shows the simulated and measured frequency response of the proposed UWB filter where wide passband is obtained with low insertion loss of 1 dB and good return loss of 13 dB. The proposed design has compact physical size of 13 x 8.5 mm^2, sharp selectivity, and a FBW of more than 100% at centre frequency of 6.85 GHz. The slight difference between simulation and measurement results is mainly attributed to fabrication tolerance. Moreover, constant group delay was obtained across the passband as seen in Figure 3.22. The simulated group delay within the 3.1-10.6 GHz passband varies between 0.1 and 0.5 ns. Sharp transition between passband and stopbands causes large fluctuation in group delay as seen near the passband edges. Table 3.1 shows a comparison of the proposed UWB BPF with other designs available in the literature which indicates that the proposed design has smaller circuit size and superior performance.
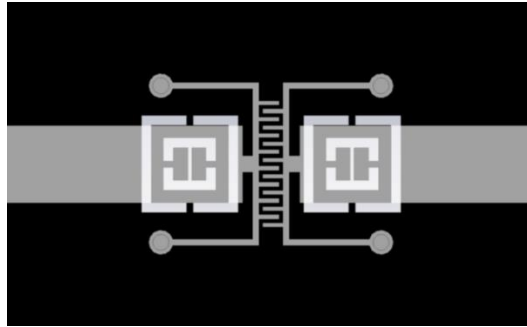
Figure 3.19 Layout of proposed UWB BPF.
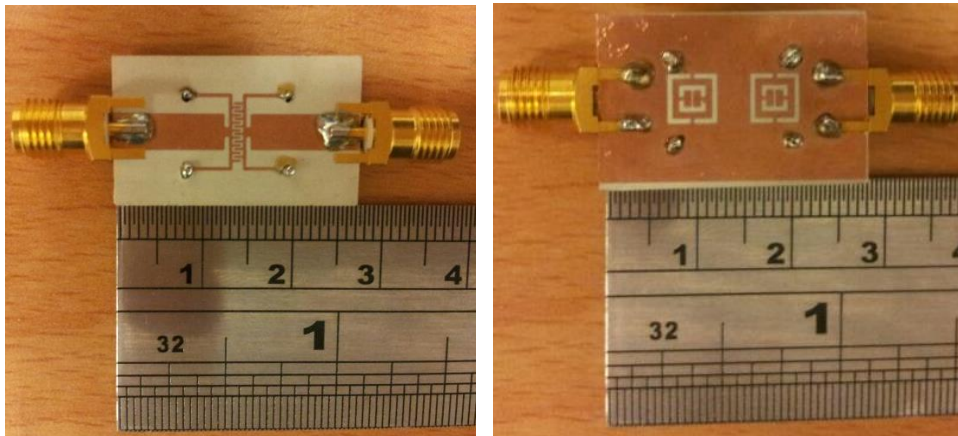
(a)   (b)

Figure 3.20 Photo of fabricated UWB BPF (a) Top view (b) bottom view.
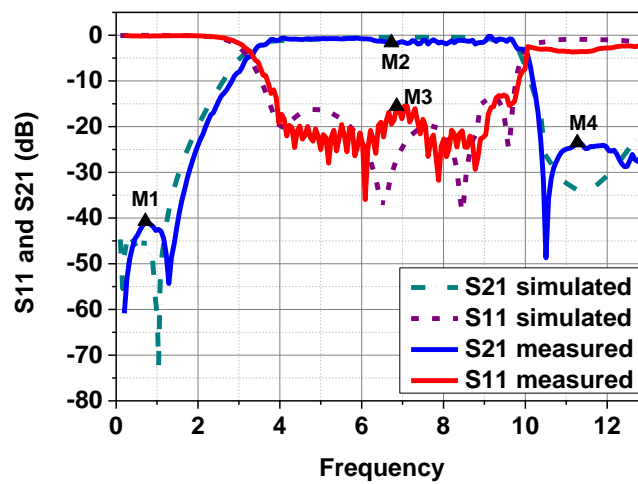
Figure 3.21 Simulated and measured S_{11} and S_{21} for the proposed UWB BPF (M1= 40 dB at 0.71 GHz, M2=

0.4 dB at 6.77 GHz, M3= 15.5 dB at 6.86 GHz, M4= 23.49 dB at 11.272 GHz).
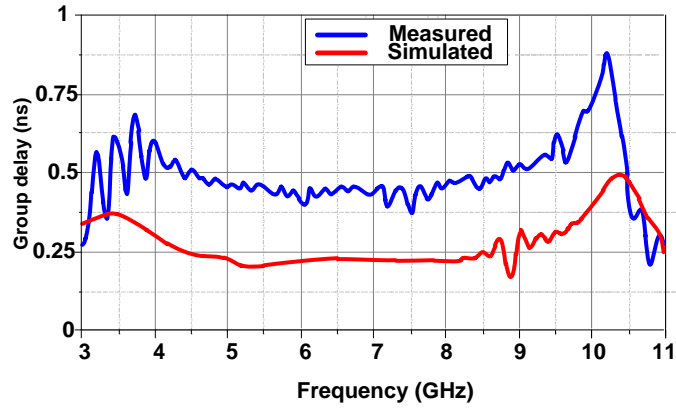
Figure 3.22 Simulated and measured group delay of the proposed UWB BPF.

Table 3.1 Comparison of the proposed BPF with other reported UWB BPF designs.

Ref.	S_{21} (dB)	S_{11} (dB)	FBW (%)	Group-delay (ns)	Size (λ_g^2)* (mm^2)
[53]	1.5	10	88	Not shown	0.619
[54]	1	<14	120	0.2	1.685
[55]	2	10	110	0.7	1.327
[56]	>2.5	>15	106	0.54	0.694
[57]	>1	11	110	0.72	3.967
[58]	>0.65	10	108	Not shown	0.587
[59]	1	10	109	Not shown	0.205
This work	1	13	104	<0.87	0.168

* λ_g denote the guided wavelength at the center frequency.

As shown in the table 3.1, different approaches have been suggested in the literature to design UWB BPF. It can be seen that these approaches have similar performance where insertion loss is varied from 0.65 dB to less than 2.5 dB. Also, most of these UWB designs achieve required 100% fractional bandwidth for UWB communication systems. The challenge was to design an UWB BPF with smaller size and similar filtering performance. The proposed UWB BPF has similar performance and 18% reduction in size when compared to the filtering structure mentioned in [60].

3.5 Chapter summary

A short review of fundamental properties of metamaterial is discussed in this chapter. Definition and history of metamaterial are presented first and then followed by explanation of the main concepts and MTM realisation approaches. Transmission line approach to realize CRLH TL structure was described using related equations and graphs. Combining thin wires and split ring resonators (SRRs) is another approach to realize metamaterial structures. It was proved that SRRs can produce $-\mu$ and thin wires produce $-\varepsilon$. The analysis and discussion mentioned here for CRLH TL are the building blocks for the design for many filters mentioned in this research work. It can be concluded that one of the distinguished characteristic of LH MTM is the antiparallel phase and group velocity which enable the realization of compact RF/microwave components with superior performance. As proof of concept, an UWB BPF was designed using CRLH TL unit cell. Due to the intrinsic high pass properties of CRLH TL, a low pass filter (LPF) was needed to improve the selectivity and realize a wide upper stopband. Hence, a LPF based on SSRR was designed on the bottom layer to ensure the compactness of the UWB BPF design. The measurement results show that the fabricated compact UWB BPF has low insertion loss, high selectivity, and wide upper stopband. The proposed UWB BPF can

be easily converted to via-less design by replacing the grounded stubs with capacitive patches to reduce fabrication complexity and cost.

Chapter 4: Dual-Band Bandpass Filters

4.1 Introduction

Many modern communication systems operate within different frequency bands which require multi-band bandpass filters (BPFs). The basic requirements of such filters are low insertion loss, high band-to-band isolation, compact size, planar configuration and low fabrication cost. Many research projects are focused on meeting such challenging requirements for multiband BPFs.

Dual-band filters can be designed using different approaches. The first approach is to use two or many more resonators where the fundamental and higher order resonant modes can be controlled to form the first and second passband [60, 61]. In [60], two short-circuit centre stepped impedance resonators (SCSIRs) are used to design a compact dual-band BPF with improved stopband characteristics. The proposed filter has good passband selectivity but suffers from high insertion loss in the second passband. Moreover, the approach used is limited to dual-narrowband BPF design.

The second approach is to connect two BPFs centred at different frequencies with common input/output ports [62, 63]. Folded open-loop ring resonators (OLRR) were used in [62] to design a dual-band BPF at 2.4/5.2 GHz for WLAN application as shown in Figure 4.1.
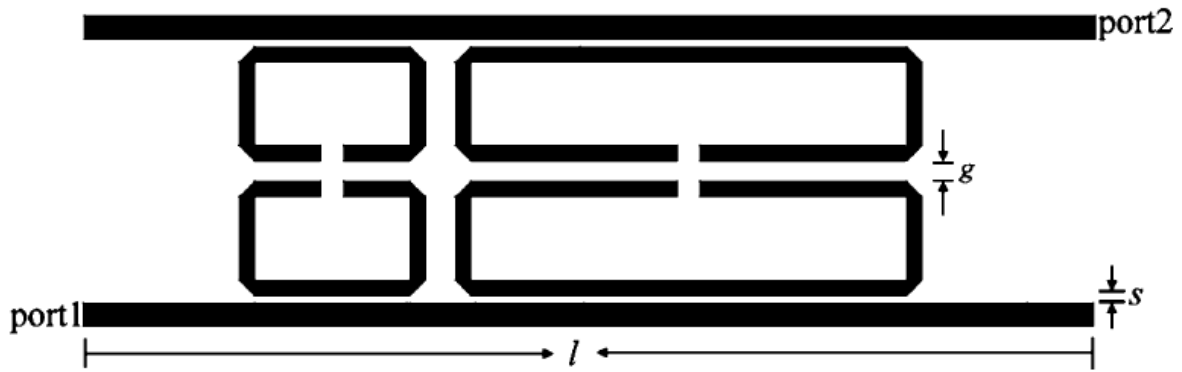
Figure 4.1 Suggested dual-band BPF based on OLRR in [64].

High performance frequency response was obtained using both electric and magnetic coupling structure. By changing the physical dimension of the OLRR, both passbands can be tuned to the desired frequency band. The main drawbacks of such approach are the large circuit size and small fractional bandwidth for each passband. The filter circuit size in [62] is 0.66 λg × 0.20 λg where λg is the guided wavelength at the centre frequency of first passband, and the fractional bandwidth for each passband is less than 7%.

The dual-band BPFs presented in [64-66] are designed using a single multimode resonator (MMR). Two passbands can be realised by arranging the resonant modes of MMR into two mode groups, TM_{01} and TM_{10}. In [64], a microstrip ring resonator is used to design a dual-band dual-mode BPF as shown in Figure 4.2. The first passband is constructed by exciting and splitting the two first order degenerate modes while the second passband is formed by the second order degenerate mode and one of the third order degenerate mode. Degenerate modes refer to the resonant modes that has the same wavenumber, i.e. they share the same resonant frequency. In the general sense, this indicates coupling between modes. However, either by out of phase excitation, or circuit modification, one can arrange the modes to be orthogonal to each other in mathematical terms. This orthogonality assures that no mode-coupling occurs between these modes. This way, one transmission zero is separated to be two transmission zeros. Two

transmission zeros are introduced between the passband using the common two-port excitation angle of 90° and the third zero is realised using the coupled-line section to have a wide upper stopband. Measurement results show that the filter has two passband centred at 2.3 and 4.1 GHz as depicted in Figure 4.3. The revised simulation results were obtained after the fabrication of the design. Due to fabrication tolerance, the fabricated filter has slightly different dimensions. Hence, the authors re-simulated the design taking into account the dimension of the fabricated filter which clearly has better agreement to the measured results. Moreover, the results show more than 30 dB band-to-band isolation and 26 dB rejection within the upper stopband. The circuit size of the filter is 0.46 λg × 0.46 λg which is very large when compared with other dual narrowband filters available in the literature.
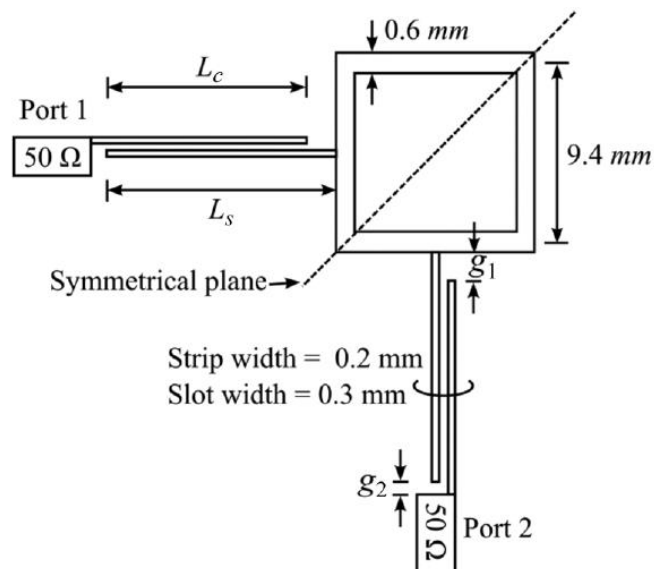
Figure 4.2 Suggested dual-band dual-mode BPF in [64].
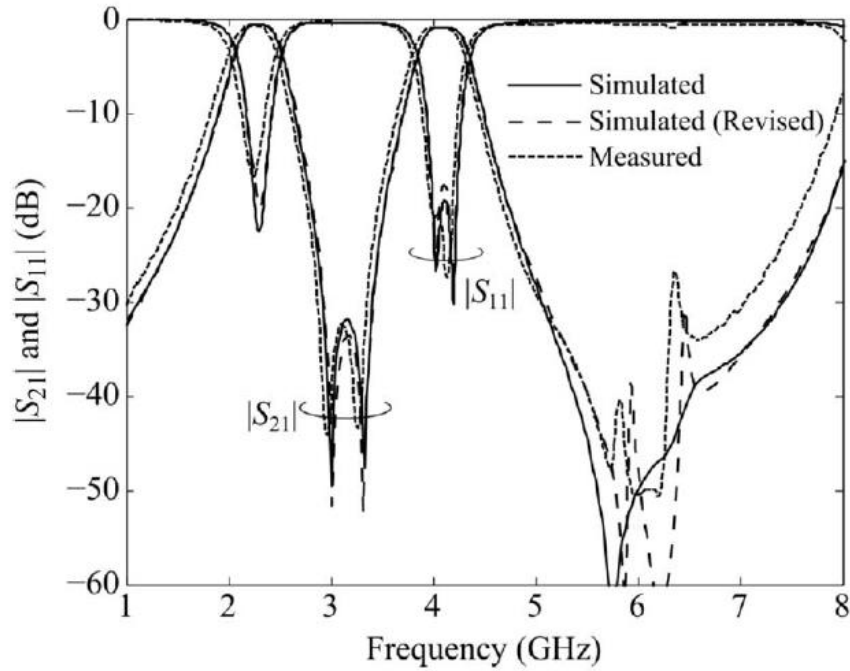
Figure 4.3 Simulation and measurement results of dual-band BPF presented in [64]

Another approach that will be discussed in this section uses bandstop structures or transmission zeros (TZs) to split a wide passband into multiple passbands [67, 68]. Authors in [67] cascaded a bandstop filter with a wide-band bandpass filter to design a dual-band BPF that operates in the unlicensed industrial-scientific-medical (ISM) 2.4/5.2 GHz bands . Coupled-serial-shunted line structure is used to construct the bandstop filter while the wideband bandpass filter is implemented using serial-shunted line structure. The bandwidth of both passbands can be controlled by varying both the central frequency of the bandstop filter and the bandwidth of the bandpass filter. The total length of the filter is 124.5 mm which is the main disadvantage of such filter design approach.

Signal interference concept was exploited in [69-71] to design dual-band BPF planar filters. In [71], dual-band BPF with widely separated passband is designed using directional couplers with loaded stubs as seen in Figure 4.4.
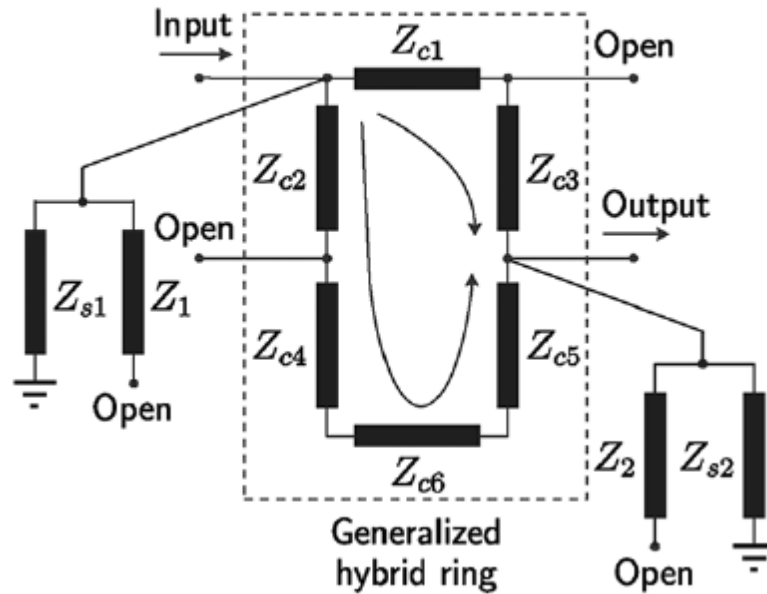
Figure 4.4 Dual-band BPF using signal interference concept presented in [71].

Due to different electrical paths provided by the structure, multiple TZs can be generated to obtain high rejection within the stopbands and high selectivity within the passbands. Dual-band BPF with superior performance can be realized using this approach at the expense of large circuit size since all of the lines used is either quarter-wavelength or half-wavelength long at the centre frequency of the second stopband.

In the following section, a super compact dual-wideband BPF design is presented. The proposed dual-wideband bandpass filter is designed using band-stop and high-pass structures to divide a wide passband into multiple passbands. Quarter-wavelength open circuited open stubs are used as band-stop structure to define the second and third stopbands at 3 and 9 GHz respectively. Both stubs are separated by a quarter-wavelength impedance transformer. Unlike conventional quarter-wavelength impedance transformers, it has a meandered line shorted to ground that forms additional stopband at zero frequency. Using this approach, a dual-wideband bandpass filter is designed, fabricated and measured. The measured results show that the fabricated dual-wideband BPF has two passbands with a fractional bandwidth of 117% and

36% at centre frequencies of 1 GHz and 6.65 GHz respectively. The first passband is designed to cover GSM 900 MHz and most of the frequencies in the L1 band while the second passband can be used for both 5.8 GHz WLAN system and 6.8 GHz RFID system. The filter is of a compact size ($0.09 \lambda_g \times 0.05 \lambda_g$) and exhibits an attenuation level greater than 20 dB up to 12 GHz.

4.2 Miniaturised dual-wideband BPF using slotted open stubs and interdigital capacitor

4.2.1 Design Analysis

The proposed filter design is based on conventional band-stop filter with a quarter-wavelength open-circuited stub [10]. This open stub is located between unit elements that are quarter-wavelength long at the centre frequency of the stopband as shown in Figure 4.5. The performance of such filter depends on the characteristic impedance of the open-circuited stub, unit elements and the two termination ports.
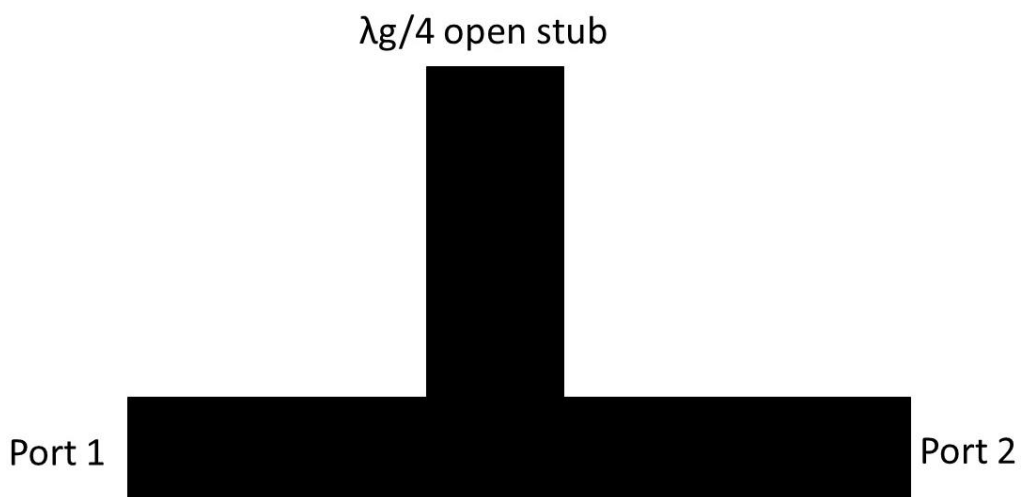
Figure 4.5 Conventional band-stop filter [10].

The design procedure of a conventional band-stop filter is mentioned in [72]. First, the ladder-type low pass prototype should be chosen. Then, the frequency response of the filter can be determined using the following frequency mapping formulas:

$$\Omega = \Omega_c \alpha \tan(\frac{\pi}{2} \frac{f}{f_0}) \tag{4.1}$$

$$\alpha = \cot(\frac{\pi}{2} \left(1 - \frac{FBW}{2} \right)) \tag{4.2}$$

where Ω and Ω_c are the normalised frequency variable and the cutoff frequency of a lowpass prototype filter, f and f_0 are the frequency variable and the centre frequency of the corresponding band-stop filter. Fractional bandwidth (FBW) of the band-stop filter is given by

$$FBW = \frac{f_2 - f_1}{f_0} \tag{4.3}$$

where f_1 and f_2 are the band edge frequencies in the band-stop response. The frequency response of this type of band-stop filter shows that spurious stop bands are centred at an odd multiple of the centre frequency f_0. The existence of such spurious stop bands can be attributed to the fact that shunt open-circuited stub is the odd multiple of $\lambda_g/4$, where λ_g is the guided wavelength at f_0. Richard's transformation is used in the frequency mapping of the band-stop filter to convert the capacitive elements of the low pass prototype to shunt open stubs while the inductive elements become series short-circuited stubs. Using Kuroda's identities, the shunt capacitor can be replaced by an open circuited transmission line, i.e. open stub, as shown in Figure 4.5. This conventional band-stop filter can be modified by introducing a slot within the quarter-wave length open stub. This modification proved to be very useful for dual-band BPF design as seen in the following analysis.

Figure 4.6 introduces the design of a slotted quarter-wave open stub (SOS), where L_s is the full length of the resonator and L_g is the length of its slotted segment. Except the slot in the open stub, the design in Figure 4.6 is the same as the one in Figure 4.5. The resonance properties of the slotted stub with variation on slot length, can be reached by analysing the mode frequencies. In the slotted stub, there are several allowed propagation configurations. These configurations can be divided into two groups: (a) those having a zero voltage plane dividing the stub along its symmetrical plane (i.e. odd modes) and (b) those having the current parallel to that plane (even modes). The current density for some of these modes is shown in Figure 4.7. These simulation results were obtained using CST microwave studio. Frequency domain simulator was used to obtain the current density at different frequency modes.
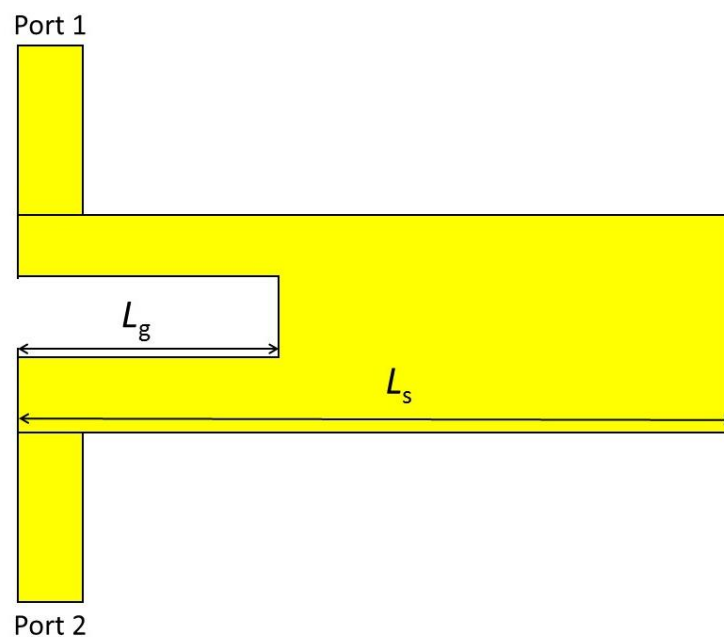
Figure 4.6 SOS with port voltage and current definitions.
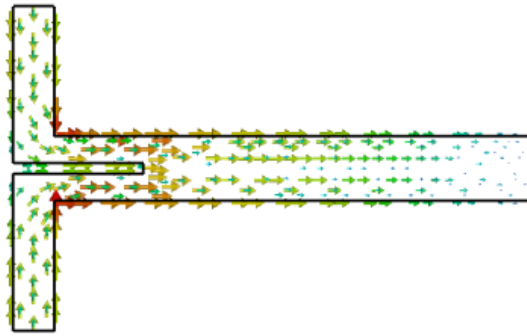
(a) First even mode
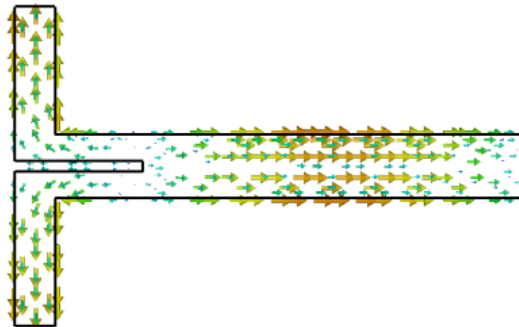
(b) Second even mode
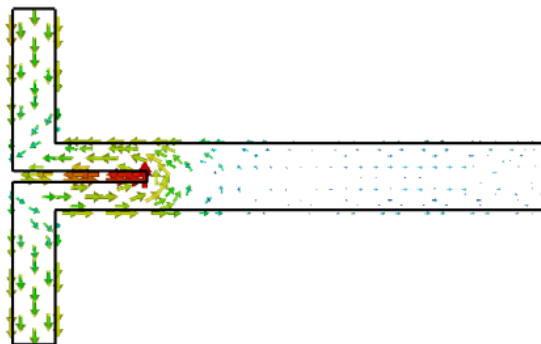
(c) First odd mode

Figure 4.7 Current density for selected even and odd modes of the SOS.

The frequencies at which these modes are excited depend on the geometry of the stub . As seen in Figure 4.8, the frequency at which the first and second even modes are excited is independent of the slot length, whereas the odd mode decreases its frequency as L_g gets bigger where L_s is kept constant at 17 mm. Hence, the SOS is a resonator that possesses the known advantages of relatively low insertion loss and compact size, usually associated with a multimode resonator.

Furthermore, the slotted open stub allows the control of resonant frequencies without the necessity of increasing the filter circuit size, which is a useful feature in multi-band filter design.
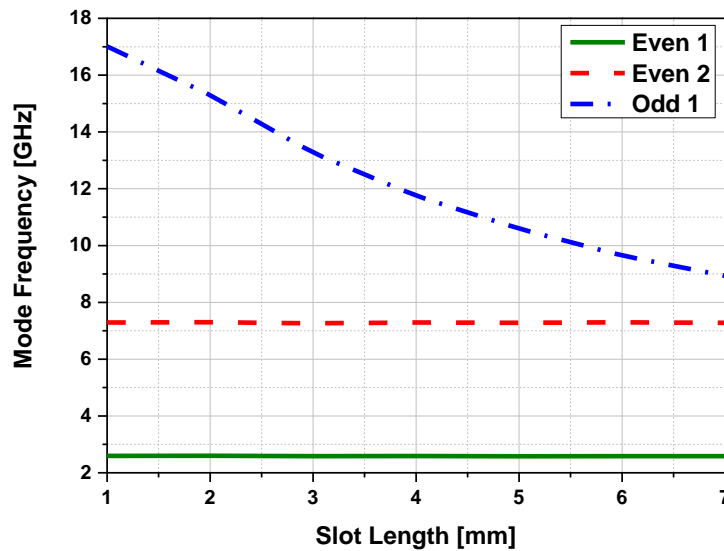
Figure 4.8 Selected mode frequencies for the slotted open stub for different slot length.

The impedance matrix for this two-port network can be derived by considering the superposition of even- and odd-mode excitations as shown in Figures 4.9(a) and 4.9(b), respectively. In the even mode, the SOS can be seen as a parallel coupled-line section, loaded with an open circuit stub or it can be seen as stubs with different width cascaded in series. However, in the odd mode it can be regarded as a parallel coupled- line section, terminated by a short circuit. Hence, current i_1 drives the SOS in the even-mode and current i_2 drives it in the odd-mode and by superposition, the total port currents I_i can be expressed as:

$$I_1 = i_1 + i_2$$

$$I_2 = i_1 - i_2 \tag{4.4}$$

91
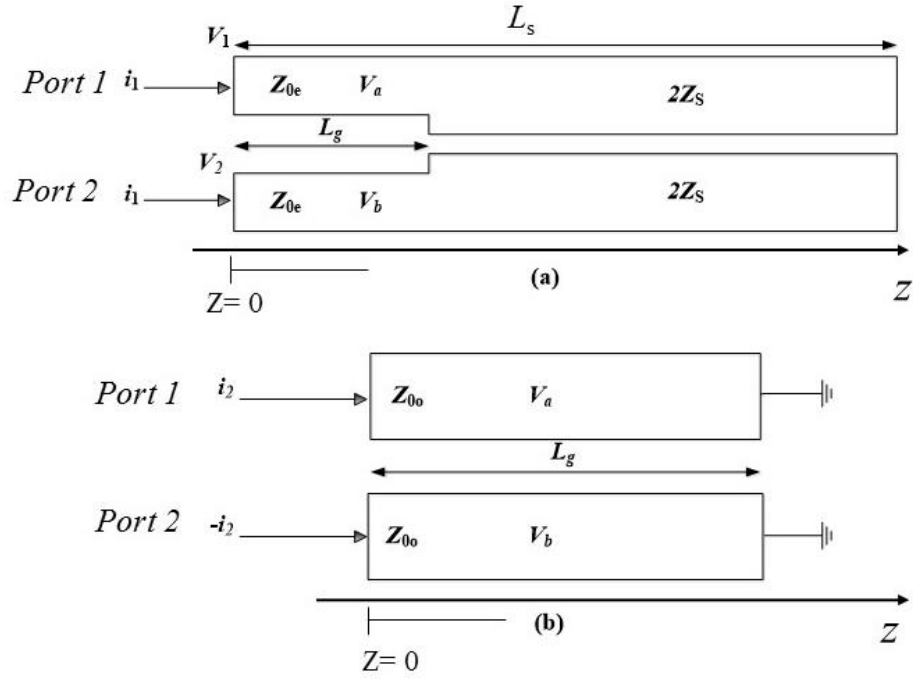
Figure 4.9 (a) SOS with even-mode current source (b) SOS with odd-mode current source.

In the even-mode, we have a line of impedance Z_{0e} terminated in an open stub with the reflection coefficient Γ expressed as [11]:

$$\Gamma = \frac{Z^{oc} - Z_{0e}}{Z^{oc} + Z_{0e}} \tag{4.5}$$

Z^{oc} is the input impedance of the open circuited stub and can be defined as:

$$Z^{oc} = j2Z_s \tan \beta_s (L_s - L_g) \tag{4.6}$$

where $Z_s, \beta_s, L_s - L_g$ are the impedance, propagation constant and length of the open circuited stub. The voltage on either conductor can be expressed as:

$$v_a^1(z) = v_b^1(z) = V_e^+ \left(e^{-j\beta_e(z - L_g)} + \Gamma e^{j\beta_e(z - L_g)} \right) \tag{4.7}$$

where β_e is the propagation constant of the coupled parallel line in even-mode and z represents the distance from the input port. The input impedance seen from the port is:

92

$$Z_{in} = Z_{0e} \frac{1 + \Gamma e^{-2j\beta_e(z - L_g)}}{1 - \Gamma e^{-2j\beta_e(z - L_g)}} \tag{4.8}$$

Therefore, the voltage at ports 1 and 2 is:

$$v_a^1(z = 0) = v_b^1(z = 0) = V_e^+ \left(e^{j\beta_e L_g} + \Gamma e^{-j\beta_e L_g} \right) = i_1 Z_{in} = i_1 Z_{0e} \frac{1 + \Gamma e^{-2j\beta_e(z - L_g)}}{1 - \Gamma e^{-2j\beta_e(z - L_g)}} \tag{4.9}$$

Solving for V_e^+ gives:

$$V_e^+ = i_1 Z_{0e} \frac{1}{e^{j\beta_e L_g} - e^{-j\beta_e L_g}} \tag{4.10}$$

Finally, after substituting (4.10) into (4.7), the expression for voltages along the conductors, when excited with even-mode current, can be written as:

$$v_a^1(z) = v_b^1(z) = Z_{0e} \frac{e^{-j\beta_e(z - L_g)} + \Gamma e^{-j\beta_e(z - L_g)}}{e^{j\beta_e L_g} - e^{-j\beta_e L_g}} i_1 \tag{4.11}$$

For odd-mode excitation, the reflection co-efficient is set to $\Gamma = -1$ in (4.11) and the voltages along the conductors can be expressed as:

$$v_a^1(z) = -v_b^1(z) = Z_{0o} \frac{e^{-j\beta_o(z - L_g)} - e^{-j\beta_o(z - L_g)}}{e^{j\beta_o L_g} - e^{-j\beta_o L_g}} i_2 \tag{4.12}$$

By superposition of even and odd modes, the total voltage at port 1 can be calculated as:

$$V_1 = Z_{0e} \frac{e^{-j\beta_e(z - L_g)} + \Gamma e^{-j\beta_e(z - L_g)}}{e^{j\beta_e L_g} - e^{-j\beta_e L_g}} i_1 + Z_{0o} \frac{e^{-j\beta_o(z - L_g)} - e^{-j\beta_o(z - L_g)}}{e^{j\beta_o L_g} - e^{-j\beta_o L_g}} i_2 \tag{4.13}$$

Solving for i_1 and i_2 in (4.4) and substituting those in (4.13) gives:

$$V_1 = \frac{1}{2} \left[Z_{0e} \frac{e^{j\beta_e L_g} + \Gamma e^{-j\beta_e L_g}}{e^{j\beta_e L_g} - e^{-j\beta_e L_g}} + Z_{0o} \frac{e^{-j\beta_o L_g} - e^{-j\beta_o L_g}}{e^{j\beta_o L_g} - e^{-j\beta_o L_g}} \right] I_1$$

$$+ \frac{1}{2} \left[Z_{0e} \frac{e^{j\beta_e L_g} + \Gamma e^{-j\beta_e L_g}}{e^{j\beta_e L_g} - e^{-j\beta_e L_g}} + Z_{0o} \frac{e^{-j\beta_o L_g} - e^{-j\beta_o L_g}}{e^{j\beta_o L_g} - e^{-j\beta_o L_g}} \right] I_2 \tag{4.14}$$

This result can be used to obtain the impedance matrix Z that describes the coupled-line section terminated in an open stub:

$$Z = \begin{pmatrix} Z_{11} & Z_{12} \\ Z_{21} & Z_{22} \end{pmatrix} \tag{4.15}$$

with:

$$Z_{11} = Z_{22} = \frac{1}{2}\left[Z_{0e} \frac{e^{j\beta_e L_g} + \Gamma e^{-j\beta_e L_g}}{e^{j\beta_e L_g} - e^{-j\beta_e L_g}} + Z_{0o} \frac{e^{-j\beta_o L_g} - e^{-j\beta_o L_g}}{e^{j\beta_o L_g} - e^{-j\beta_o L_g}} \right]$$

$$Z_{12} = Z_{21} = \frac{1}{2}\left[Z_{0e} \frac{e^{j\beta_e L_g} + \Gamma e^{-j\beta_e L_g}}{e^{j\beta_e L_g} - e^{-j\beta_e L_g}} - Z_{0o} \frac{e^{-j\beta_o L_g} - e^{-j\beta_o L_g}}{e^{j\beta_o L_g} - e^{-j\beta_o L_g}} \right]$$

The transmission co-efficient S_{21} can be calculated using the impedance matrix Z and compared to the simulated S_{21} for a slot length $L_g = 3$ mm as shown in Figure 4.10. The 3D electromagnetic simulation results was obtained using CST microwave studio. It can be observed that good agreement is obtained between calculated and simulated results.
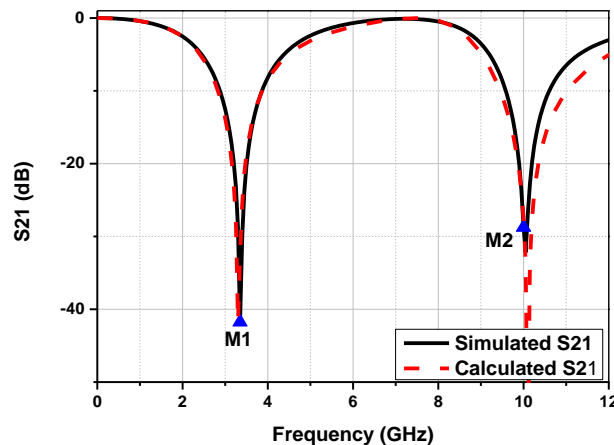
Figure 4.10 Comparison between simulated and calculated S21 for proposed SOS (M1= 41.73 dB at 3.3 GHz, M2= 28.72 dB at 10.05 GHz.

The inner open stub resonator can be embedded within the SOS, as shown in Figure 4.11. The dimensions for the SOS with inner open stub are (mm): L1= 20.7, L2= 4.85, L3= 5.65, W1= 1.7, W2= 4.22, and the inner open stub width is 0.7 mm. The introduction of such a resonator is used to: (i) control the second passband bandwidth (ii) improve roll-off rate at the upper edge of the second passband and (iii) realise wider upper stopband, without increasing the circuit size as presented in Figure 4.12. Since the inner stub is embedded into the SOS structure, there exists many coupling paths, which complicate the process of equivalently representing the structure with lumped elements. The addition of the inner stub means opening a slot in its place, which increases the current path length flowing along the upper strip of the SOS, representing an inductance. The inner stub acts as a regular open stub, but calculation of its length should take into account the coupling effects with the SOS. Overall, this inner stub acts as the second ladder elements of the low pass prototype, which then adds a new stop-band (hence, a new TZ) to the overall frequency response. The dimensions of the inner open stub need to be optimized to obtain the required stopband performance. It can be seen from Figure 4.12 that there are two TZs at 9.1 GHz and 10.8 GHz. The TZ located at 9.1 is due to the inner open stub and the second TZ is generated due to the effect of the SOS. Its worth to point out that the slot affected the location of the TZ for the SOS without inner open stub which is designed to have a bandstop response at a f_0 =3.4 GHz. It can be observed that the second TZ appears at 3.24 f_0 and not 3 f_0 as seen in conventional bandstop filter. Controlling the harmonic response of the filter is yet another useful feature of SOS structure.
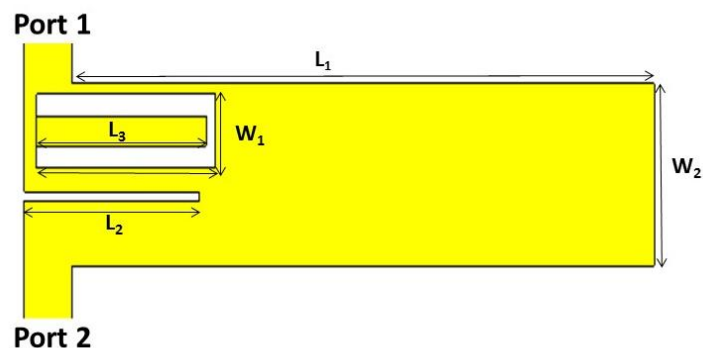
Figure 4.11 Layout of SOS with inner open stub.
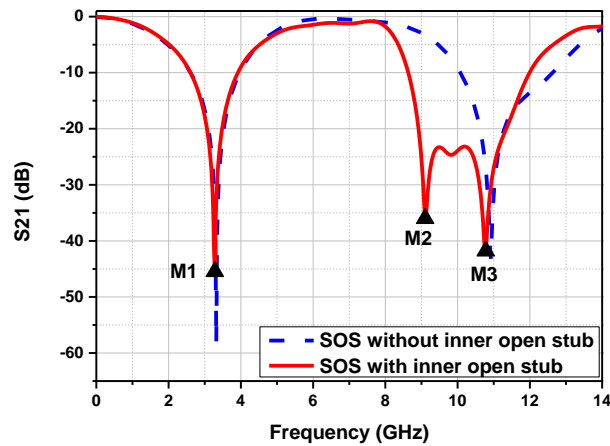
Figure 4.12 Comparison of simulated S21 for SOS with and without inner open stub (M1= 41.39 dB at 3.29 GHz, M2= 35.99 dB at 9.1 GHz, and M3= 42.04 dB at 10.89 GHz)**.**

4.2.2 Design Procedure

The dual-wideband bandpass filter was firstly designed using slotted quarter-wavelength open stubs, as shown in Figure 4.13. These slotted open stubs are used to define the second and third stopbands at 3 and 9 GHz, respectively. Both stubs are separated by a quarter-wavelength impedance transformer, which has a high-pass meandered line, shorted to ground, forming an additional stopband at zero frequency.
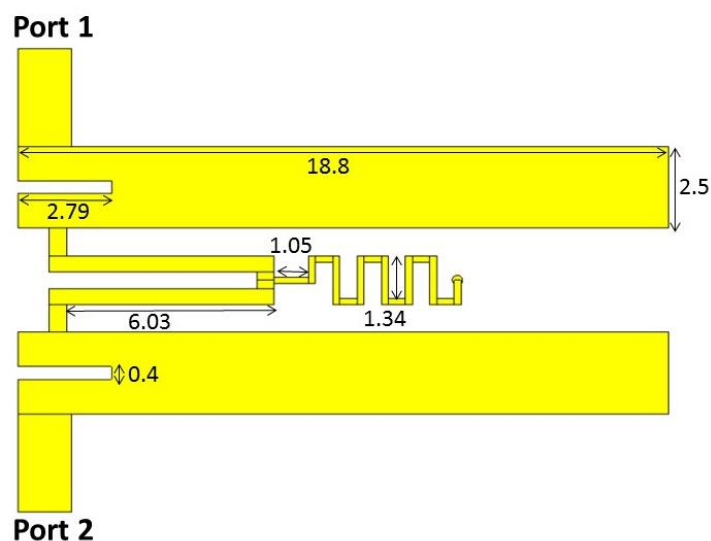
Figure 4.13 Preliminary design of the dual-wideband BPF with dimensions in mm.

The simulation results of the preliminary design of the dual-wideband BPF is presented in Figure 4.14. These results show that the two passbands are centred at 1.2/6.4 GHz, with 3dB fractional bandwidths of 103% and 42%, respectively. The simulated IL at the centre frequencies are 0.1/0.2 dB, while the return loss within the two passbands is better than 18/20 dB respectively. The isolation between passbands can be calculated by observing the rejection level within the second stopband. It can be seen that the rejection level is around 30 dB between 3 GHz and 3.6 GHz. Hence, it can be concluded that the isolation between the first and second passband is better than 30 dB between 3 GHz and 3.6 GHz. There is only one transmission pole at the first passband and two transmission poles at the second passband. Increasing number of poles can further increase the selectivity of the filter. This can be achieved by employing stepped impedance coupled slotted open stubs as will be seen in the final design structure. The roll-off rate value (ζ) for each passband [73] can be obtained as follows:

$$\zeta = \frac{\alpha_{max} - \alpha_{min}}{f_s - f_c} \tag{4.16}$$

where α_{max}, α_{min}, f_s and f_c are, respectively, the 20-dB attenuation point, the 3-dB attenuation point, the 20-dB stopband frequency and the 3-dB cut-off frequency. The first passband has roll-on/off rates of 38 dB/GHz and 26 dB/GHz at the lower and upper passband edges, while the second passband has roll-on/off rates of 16 dB/GHz and 20 dB/GHz at the passband edges. To improve the selectivity of the dual-wideband BPF, mode splitting is employed to obtain two transmission zeros within the second stopband at 3 GHz, by utilizing coupling interdigital capacitors at the end of the open stubs as seen in Figure 4.15. In addition, inner open stubs are used to obtain a sharp roll-off rate at the upper edge of the second passband. By stepping the impedance of the slotted quarter-wave open stubs, dual-mode response is achieved within the first passband. Fine tuning stubs are used to prevent parasitic

passband between the first and second passband. The final simulation results are shown in the following section.
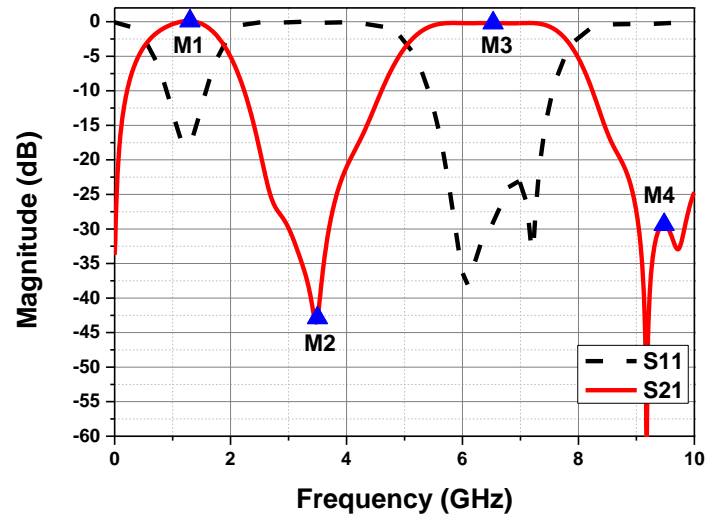
Figure 4.14 Simulated results of the preliminary design of the dual-wideband BPF (M1= 0.1 dB at 1.29 GHz, M2= 41.6 dB at 3.15 GHz, M3= 0.19 dB at 6.53 GHz, M4= 29.45 dB at 9.5 GHz).

4.2.3 Experimental results and discussion

Figure 4.13 shows the layout of the proposed dual-band BPF, in which the structure was optimized using the full-wave electromagnetic simulator (CST Microwave Studio).The layout dimensions of the fabricated filter are presented in Table 4.1.

Table 4.1 Dimensions of the proposed dual-wideband BPF (mm)

W_1	W_2	W_3	W_4	W_5	W_6	W_7	L_1	L_2	L_3	L_4	L_5	L_6	L_7
1.56	0.15	0.7	0.18	2.8	0.12	1.1	14.42	5.4	3.1	13.97	2.8	7.36	1
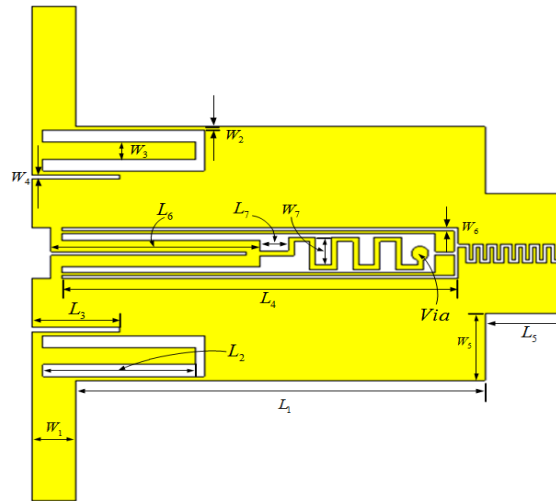
Figure 4.15 Layout of proposed dual-wideband BPF.

The interdigital capacitor has the following dimensions: finger width = 0.125 mm, spacing between fingers = 0.125 mm and number of fingers = 14. Figure 4.16 shows a photograph of the fabricated dual-wideband BPF. The inner conductor of the SMA connector is soldered to the top layer of the board, which contains the filter, and the connector chassis is soldered to the bottom layer containing the ground plane of the microstrip structure. The filter was fabricated using a Taconic TLY-5 substrate, with a thickness = 0.508 mm, dielectric constant = 2.2, and loss tangent = 0.0009.
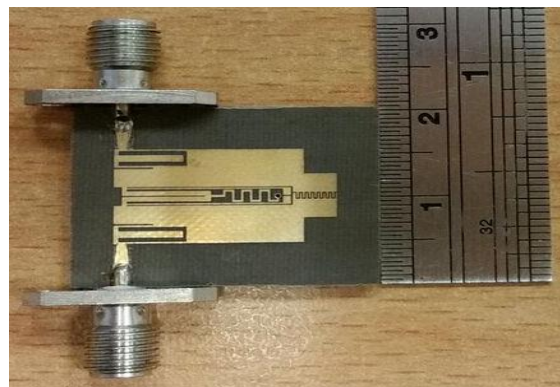
Figure 4.16 Photo of the fabricated dual-band BPF.
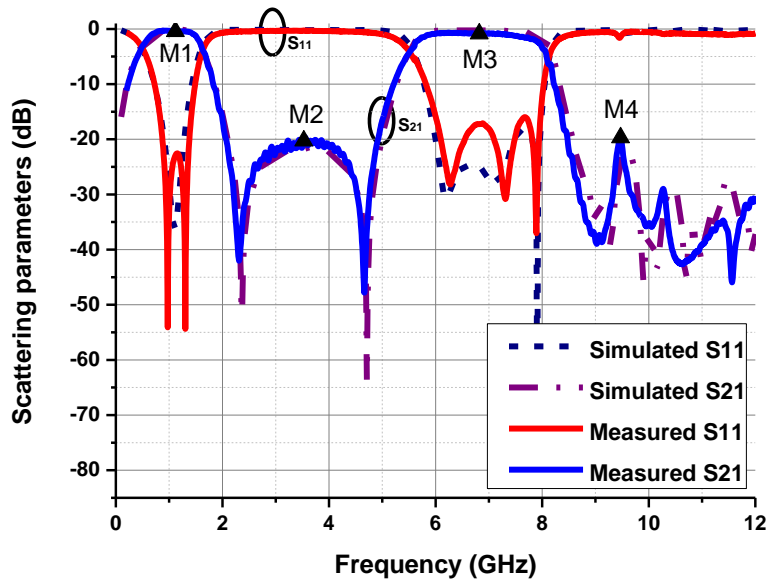
Figure 4.17 Simulated and measured results of proposed dual-wideband filter (M1= 0.3 dB at 1 GHz, M2= 20.11 dB at 3.44 GHz, M3= 1 dB at 6.8 GHz, M4= 19.86 dB at 9.47 GHz).

Figure 4.17 presents the simulated and measured results of the proposed filter, which demonstrate that a very good agreement has been achieved between simulation and measurement results. The measured results show that the two passbands are centred at the design frequencies which are 1/6.65 GHz with 3dB fractional bandwidths (FBWs) of 117% and 36%, respectively. The measured insertion loss at the centre frequencies is 0.3/1 dB, while the return loss within the two passbands is better than 20/15 dB respectively. The isolation between the first and second passband is better than 20 dB from 2.0 to 4.9 GHz. The filter also exhibits a rejection level of more than 20 dB from 8.5 to 12 GHz and sharp roll-up/down rates are obtained at the edges of both passbands. The roll-off rate at the upper edge of the first passband is increased to 36 dB/GHz, while roll-up/down rates for the second passband are increased dramatically to 33 dB/GHz and 41 dB/GHz, respectively. The proposed filter has better performance and smaller size in comparison with other dual-band BPFs reported in the literature, as shown in Table 4.2.

Table 4.2 Performance comparison with reported dual-band BPFs.

Ref.	CFs (GHz)/ FBW (%)	ILs at CFs (dB)	Isolation (dB)	Circuit size $(\lambda_g{}^2)$
[74]	2.4 / 13.7, 5.16 / 6.3	0.6, 1.4	> 11	0.193
[75]	2.3/54, 5.25/20	0.8, 0.8	> 25	0.09
[76]	1.53/48.5, 6.52/ 54.2	0.1, 0.8	> 25	0.012
[77]	0.58 / 39.6, 1.31 / 18.3	0.3, 0.9	> 20	0.021
[78]	1.96/57.1, 5.58/20.8	0.1, 0.8	> 30	0.02
[79]	1.63/28.8, 2.42/22.7	0.86, 0.97	> 15	0.213
[80]	2.43/4.5, 3.73/6.1	2.5, 1.3	> 18	0.296
[81]	0.61/32.3, 1.36/10.5	0.45, 0.75	> 30	0.0159
[82]	2.41 / 10.8, 3.51 / 6.4	1.45, 1.74	> 15	0.301
[83]	0.58 / 34.1, 1.41 / 12.5	0.65, 0.95	> 20	0.01
[71]	0.63/69, 2.37/18.4	0.14,1.07	> 40	0.08
This work	1/117, 6.65/36	0.3, 1	> 20	0.004

λ_g denotes the guided wave-length at the centre frequency (CF) of the 1st passband.

Filter designers achieved good filtering performance for the dual-band BPF designs mentioned in Table 4.2 using different techniques. Stub-loaded patch resonator is used in [74] to design a dual-band BPF with centre frequencies of 2.4 GHz and 5.2 GHz. By using cross slot within the patch, the patch size can be reduced and two orthogonal modes can be excited in the passbands. Even and odd modes within the passband can be controlled using two sets of open stubs. Moreover, these opens stubs can be used to adjust the filter's input impedance. Large circuit

size and poor isolation between the passband are some of the major drawbacks of this design approach.

In [75], a dual band BPF design technique is suggested where the two passbands can be controlled. Using short-circuited stepped impedance resonators (SIRs), the centre frequencies and fractional bandwidth can be adjusted. Measured results show that up to 54% can be achieved within the first passband with good passband performance but poor rejection level is observed at both first and third stopbands.

The filter used in [76] is a dual, tri or quad band BPF with open and short stubs that are loaded with SIRs. Stubs are used to divide the multiple resonant modes of the filter. Measurements indicate that in the dual-band topology, FBW of 54.2% is achieved. It is pointed out, though, that it is quite difficult to set the resonant frequencies for each band as desired, and with the quad-band topology, FBW is significantly reduced for each band.

Asymmetrical frequency transformation is used in [77] in order to obtain a dual-band BPF. Authors used eighth-wavelength unit elements and applied a modified Richard's transformation, which enables creating an asymmetrical dual-band response. Measured FBW for a 4th order filter is found to be as 39.6% for the widest band, with good IL values as low as 0.3 dB at the lowest band.

In [78], a single quadruple-mode microstrip resonator is used to design a dual-band BPF. This filter design contains two symmetrical pairs of TZs, which are used to widen the two passbands. This way, a 57.1% FBW is obtained at the lower band, with a high (>30 dB) isolation compared to other works. IL is also one of the lowest of the other reported BPFs.

Another dual-band BPF is designed in [79] by applying transversal signal-interaction with a T-shaped microstrip structure. This BPF contains short and open stubs, as well as coupled lines

to obtain multiple TZs at the desired frequency bands. Measurement results indicate that a maximum of 28.8% FBW is achieved in the low pass-band, however, circuit size is too large compared to the other reviewed dual-band BPF designs.

In [80], a dual-band BPF is realized by using a single circular slotted patch. Utilizing the uncoupled degenerate modes, authors were able to design a dual-band BPF with very high selectivity. The FBW of the filter is measured to be 6.1% at the upper band. However, due to the low FBW, higher IL is observed compared to other dual-band BPFs. Physical size of the filter is another downside; it is the one of the largest of the reviewed dual-band BPFs.

Coupled SIRs are implemented in [81] to design a dual-band BPF. These SIRs are placed very close to each other to create a coupling structure, which are then solved by even and odd mode analyses. The resulting filter has five TZs, which are utilized to improve the stop-band performance. Measured FBW is 32.3% at most in the lower band, and a very high rejection level is observed within the stopbands.

A novel approach to a compact dual-band BPF design is found in [82], in which, authors implemented a substrate integrated waveguide (SIW) as part of the resonators. Instead of a fully closed waveguide, a half-mode, slotted SIW is designed, which are then used as part of the coupling network. However, the resulting filter's physical size is the largest of the reviewed dual-band BPFs. With a measured FBW of 10.8% in the lower band, this BPF provides a narrow pass-band. The rejection level is at least 15 dB between the pass-bands, which is also lower than most of the reviewed BPFs.

In [83], open and shorted SIRs are once again used to develop a dual-band BPF filter synthesis approach. The equivalent circuit of the SIRs are expressed as a transversal structure, and a source-load coupling circuit. Additional TZs are used to increase the rejection ratio at the stop-

bands. The realized filter provided 34.1% FBW at the lower band, and rejection level is found to be at least 20 dB within the second stopband, with an IL of 0.65 dB at the lower band.

The last dual-band BPF mentioned in Table 4.2, has sharp rejection level within the stopbands with widely separated passbands [71]. This impressive filtering performance is achieved using transversal signal interference concept. Due to different electrical paths, several TZs can be generated and placed according to design requirements. Measurement results indicate that this filter provides two pass-bands, the lower band having a FBW of 69% and centred at 0.63 GHz, with an IL of 1.14 dB. The second passband is centred at 2.37 GHz with FBW of 18.4% while the rejection level within the second stopband is around 45 dB.

4.3 Chapter summary

In this chapter, different approaches to design dual wideband BPF are discussed. Most of these approaches offer low IL, good selectivity, and wide upper stopband bandwidth with high rejection level at the expense of large circuit size. Here, a miniaturized dual wideband BPF is realized using both short and slotted open stub resonators. The band-stop structure is realized by the coupled slotted open stub while the high pass structure is realized by the quarter-wave length impedance transformer that is shorted to ground. Moreover, inner open stubs are used within the slotted open stubs to improve the selectivity of the second passband and obtain higher rejection level at the upper stopband. It can be seen that the proposed design has better performance that the dual-band BPF reported in [76] and smaller size by almost 66%.

Chapter 5: Filter Based Oscillator

5.1 Introduction

The tremendous growth of today's telecommunications market has brought an increasing demand for high performance, low power consumption and low cost radio frequency (RF) integrated circuits (ICs). A huge amount of effort has been reported to design voltage controlled oscillators (VCOs), which generate the local oscillator (LO) carrier signal. Oscillator design has remained a major challenge to many researchers and manufacturers and thus has received considerable attention in recent years.

A very important and critical building block of almost any transceiver in wireless communication is the LO. In communications, calibration and instrument signal sources are required for some carriers for increasing baseband information. Local oscillators are needed to achieve frequency up-conversion/down-conversion in wireless communication system. Significant advances have been made in the last ten years in terms of phase noise reduction for LO design. They are required whenever heterodyning is employed in receivers to convert high-frequency signals to an intermediate-frequency (IF) spectrum to simplify the processing.

Local oscillators are described as an important electronic device which is used to generate a signal for the application of converting a signal of interest by using mixers to a different frequency. This process produces the sum and difference of the frequency of the LO and frequency of the input signal of interest or the required intermediate frequency conversion. LOs are widely used in applications of frequencies ranging from a few kilohertz (kHz) to many gigahertz (GHz). It seems that the most critical parameter for any oscillator is phase noise. It is widely used to characterise the spectral purity of an oscillator as well as the frequency

stability. For example, in receivers, the phase noise of the oscillator limits the capability to detect a weak signal in the existence of a strong signal in an adjacent channel, while a transmitter's phase noise outcomes in energy are being transmitted outside of the required bandwidth.

There are three major sources of communication system performance degradation due to LO phase noise [84]:

1. Coherence or correlation error

2. Signal loss due to phase modulation (PM) spreading

3. Additive noise effect

Coherence error applies to coherent demodulation only. Noise in the demodulator carrier tracking loop (i.e., phase noise estimation loop) causes a phase error which results in a loss in BER (bit error rate) performance. The usual assumption is that the bandwidth of phase estimation loop is small in comparison with the data rate. The resultant phase error may then be considered as constant during each bit interval. In an M-ary transmission with M>2, this effect also produces inter-channel interference. Demodulator phase error causes a cross coupling between, for example, the two orthogonal channels of a Quadrature Phase Shift Keying (QPSK) transmission.Signal loss due to PM spreading leads to the degradation in signal to noise ratio. Additive noise effect is the increase in received noise floor due to the LO noise characteristics. LO noise is integrated in the detection bandwidth and added to integrated thermal noise.

5.2 Feedback oscillator

The most common type of harmonic oscillator is the feedback oscillator which mainly consists of an amplifier and frequency selective element such as BPF or resonator as shown in Figure 5.1. It is worth mentioning here that feedback circuit could contain either series or parallel LC circuit as series or shunt resonator. An amplifier with voltage gain *A* is connected in a feedback loop with its output fed back into its input through a feedback network to generate a continuous wave signal.
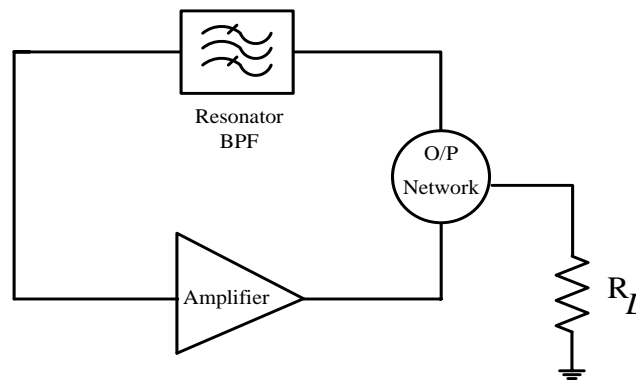
Figure 5.1 Feedback oscillator system [85].

According to Barkhausen criterion [85], steady-state oscillation will be sustained by the circuit at certain frequencies where:

1- The absolute magnitude of the loop gain $|\beta A| \geq 1$, where β is the transfer function of the feedback circuit.

2- The phase shift around the loop is zero or an integer of 2π.

The feedback network can be replaced with a simple parallel RLC tank circuit shown in Figure 5.2. The parallel resistance R represents the overall loss within the tank circuit. In this model, the inductor and capacitor are ideal and have no loss; reactive energy is transferred between these passive devices.
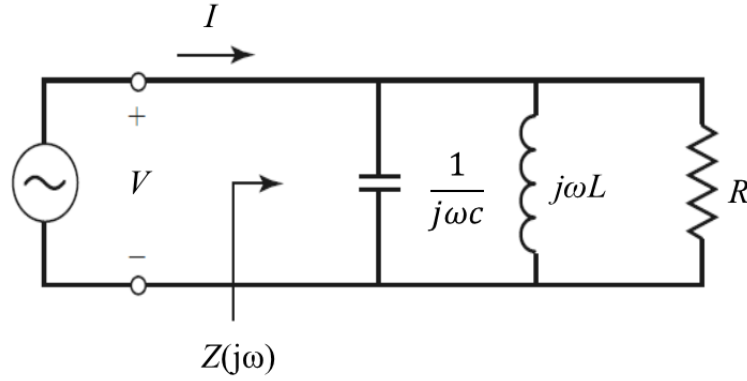
Figure 5.2 A Parallel RLC resonant circuit [11].

The magnitude and phase of Z(jω) for a parallel resonant circuit are:

$$|Z(j\omega)| = \frac{R}{\sqrt{1 + Q_0^2 \left[\frac{\omega}{\omega_0} - \frac{\omega_0}{\omega} \right]^2}} \qquad \angle Z(j\omega) = -\tan^{-1} \left[Q_0 \left(\frac{\omega}{\omega_0} - \frac{\omega_0}{\omega} \right) \right]$$

(5.1)

Where ω_0 is resonance or oscillation frequency and can be defined as:

$$\omega_0 = \frac{1}{\sqrt{LC}}$$

(5.2)

The frequency response of a linear time-invariant filter, such as the parallel RLC circuit in Figure 5.2, can be described with a complex transfer function, which is a function of frequency. Phase response then refers to the angle between the real and imaginary parts of the transfer function, with respect to the frequency.

The quality factor (Q) of resonant circuit is an important design parameter that affects the oscillator performance as mentioned in Leeson's oscillator model [86]. The output oscillation spectrum $S_\phi(\delta\omega)$ can be defined as:

$$S_\emptyset(\delta\omega) = S_{\Delta\theta} \left[1 + \left(\frac{\omega_0}{2Q\delta\omega} \right) \right]$$

(5.3)

108

where $\delta\omega$ is the offset frequency from the oscillation frequency ω_0, $S_{\Delta\theta}$ is the additive noise component, and Q is the quality factor of the oscillator. Q accounts for the loss in the resonant circuit and general definition for Q is:

$$Q = \omega \frac{average\ energy\ stored}{energy\ loss/second} \tag{5.4}$$

and can be measured by applying a step input and observing the decay of oscillations at the output. The effect of resistance (R) on the Q will be contributory to the denominator of Eq. 5.4, thereby reducing the Q of the resonator. This general definition for Q cannot be applied if the circuit has no inductor which indicates the need for more accurate definition for Q in oscillator design [87]. The general definition of Q is based on RF oscillation cycle and without an inductor, no oscillation can be observed. By considering the phase response of the resonator used in oscillator design, the quality factor of the resonator can be defined as:

$$Q_r = \frac{\omega_0}{2} \left| \frac{d\emptyset(\omega_0)}{d\omega_0} \right| = \frac{\omega_0}{2} \tau_d \tag{5.5}$$

where ω_0 is the oscillation frequency, $\emptyset(\omega_0)$ is the phase response of the resonator, and τ_d is the group delay. This definition proved to be more accurate for oscillator design and phase noise was reduced in many oscillator designs by increasing Q_r [88, 89]. As mentioned earlier, frequency selective element in the feedback network is not restricted to resonator and BPF can be utilized as shown in Figure 5.3 [90].
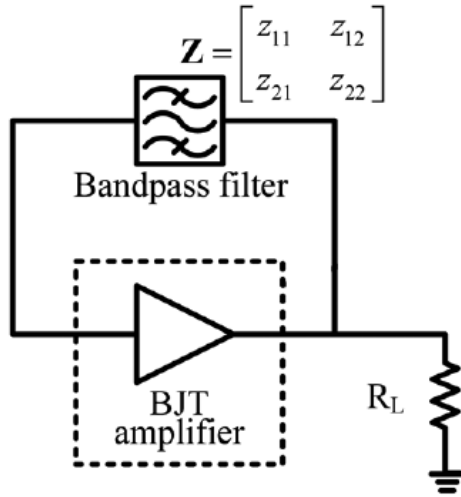
Figure 5.3 Block diagram of filter-based feedback oscillator [90]**.**

The frequency response of the BPF can be represented by the impedance matrix, Z. In [91], spectrum based quality factor Q_s is introduced which takes into account the derivative of both the amplitude and phase response of the BPF with respect to the frequency and is defined as:

$$Q_s = \frac{\omega_0}{2} \left| \frac{d}{d\omega} \ln \left| \frac{Z_{11}}{Z_{12}} \right| + j \frac{d}{d\omega} \left(\angle(Z_{11}) - \angle(Z_{12}) \right) \right| \tag{5.6}$$

Q_s accounts for the effects of amplitude and phase response of the BPF and is more precise than Q_r. Phase noise will be defined in the next section to understand how it relates to the oscillator noise performance. In section 5.3, a feedback oscillator will be designed using CRLH TL unit cells at Q_r peak and Q_s peak frequencies to compare the phase noise results.

5.2.1 Phase Noise in Oscillators

An ideal signal generator would be able to produce a pure signal which could be represented as a single spectral line. In the real world, signal generators may produce a signal with unwanted amplitude or contain some small random perturbations in the phase of the output signal [84]. These phase-modulated components are defined as phase noise.

Considering the following noise-free signal:

$$v(t) = A\cos(2\pi f_0 t) \tag{5.7}$$

where A and f_0 denote the amplitude and frequency of the signal, respectively. Phase noise is added to this signal by adding a stochastic process denoted by φ as follows:

$$v(t) = A\cos(2\pi f_0 t + \varphi(t)) \tag{5.8}$$

Oscillator noise performance is characterized as a jitter in the time domain and as phase noise in the frequency domain. The importance of each one depends on the application. Therefore, RF/microwave engineers try to minimize phase noise while the digital signal processing specialist goal is to minimize the jitter. Phase noise and jitter are related to a noisy oscillator and, in general, as the phase noise increases in the oscillator, so does the jitter.

For an ideal oscillator, the frequency response is only on a single frequency, which can be shown as a single line in a frequency plot. In practice, however, oscillators include the phase noise frequency components in the frequency domain as well. Therefore, the actual oscillator frequency response includes "skirts" around the centre or "carrier" frequency, as illustrated in Figure 5.4.
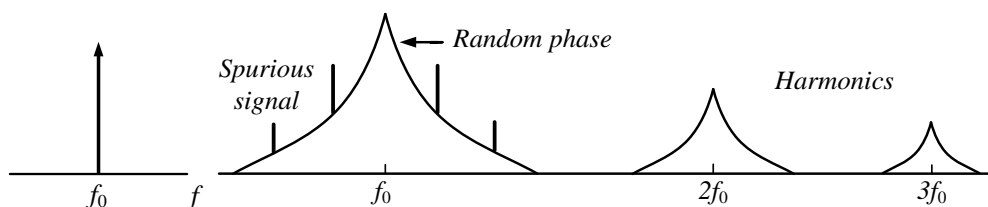
Figure 5.4 An ideal signal (left) and actual signal with additional phase noise (right).

Discrete spurious signal and random phase both can contribute to the noise within the output signal. The discrete spurious signals appear as distinct components in the spectral density and

the random phase fluctuations are the main source of phase noise [92]. The significance of phase noise can be understood by assuming a local oscillator (LO) which generates the carrier signal to a mixer situated in a frequency synthesizer. If the LO output contains phase noise, both the down converted and up converted signals are corrupted and great amount of interference can be observed at the adjacent frequencies Moreover, two overlapping spectra can be observed at the down-converted band when two signals are mixed with the output of the LO due to phase noise.

The performance of communication systems will degrade when noisy signal are generated from local oscillators. An oscillator's phase noise can be explained using the single-sideband (SSB) phase noise, shown in Figure 5.5, which equals to the ratio of noise power in a 1 Hz bandwidth at an offset, f_m, to the signal power. SSB phase noise is calculated in dBc/Hz at a certain frequency offset from the signal frequency [93] as:

$$L(f_m) = 10 \log \left[\frac{P_{noise}(f_m)}{P_{signal}} \right] \tag{5.9}$$

Variations in the amplitude or phase of the signal source are the main reason for SSB phase noise.
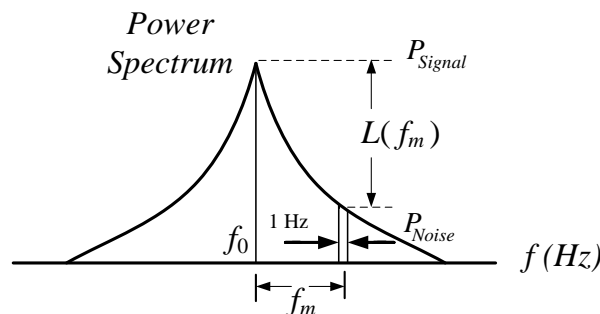
Figure 5.5 Definition of phase noise.

5.3 Low phase noise feedback Oscillator design using LH TL unit cells

Oscillators are considered an integral part of almost all wireless communication systems. Researchers tried many design approaches [88, 94-96] to satisfy oscillator design requirements, specifically low phase noise, low power consumption and low cost. Temperature stabilized dielectric resonator with a very high loaded Q (8000) is employed in [88] to develop an ultra-low phase noise oscillator. Moreover, the design can be converted to a voltage controlled oscillator (VCO) with a bandwidth of over 1500 KHz by using a tunable varactor. Although, excellent phase noise performance is achieved using this approach, dielectric resonator is difficult to integrate with other planar circuits which complicates the design and increases the fabrication cost.

Planar RF and microwave oscillator [94, 95, 97] is considered a good alternative to oscillator designs based on dielectric resonator. In [95], a planar oscillator is designed using four-pole elliptic microstrip BPF. High group delay peaks can be achieved using elliptic BPF due to the existence of TZs near the passband which can be easily translated to high Q_r values. It is worth mentioning here that Leeson derived an approximate formula for phase noise in feedback oscillator that shows higher group delay peaks results in lower phase noise [95]. The single-sideband noise power (P_{SB}) is defined relative to the oscillator output power (P_C) as:

$$\frac{P_{SB}}{P_C} = \left(\frac{LFKT}{P_C} \right) \cdot \left(\frac{\omega_c}{\omega_m . \tau_d} + \frac{1}{\omega_m} + 1 \right) \tag{5.10}$$

where L is the insertion loss for the frequency stabilization element utilized in the feedback, F is the amplifier noise figure, T is the ambient temperature, K is the Boltzman constant, ω_c is the flicker noise corner frequency, ω_m is the offset frequency and τ_d is the group delay of the

feedback network. Authors in [98] used an active filter to further reduce the phase noise of the oscillator achieved in [95]. The measurement results show a phase noise improvement of 6.5 dB at 1 MHz offset frequency at the expense of increasing the manufacturing cost due to the need of two microwave transistors. In [90], the authors explained that the Q_r peak frequency value might not match the oscillator Q value. Therefore, best phase noise performance might not be obtained and suggested using the frequencies at Q_s peak.

Using the design approach mentioned in [90], a novel narrowband BPF is designed using two CRLH TL unit cells. Q_r and Q_s are both calculated and utilized to construct the proposed low phase noise oscillator. The simulation results indicate that significant improvement in phase noise is achieved at the frequency of Q_s peak.

5.3.1 Filter design using LH TL unit cells

LH TL based structure can be realized using different design approaches [33, 40, 99, 100]. The hybrid approach is one of them where resonators are combined with series capacitive gaps and shunt grounded inductances [101]. One intriguing features of this LH structure is the generation of TZ due to the presence of CSRR, which enables the design of compact BPF with good stopband rejection level [102]. The layout of the hybrid unit cell consist of CSRR, series gaps, and shunt grounded stub as presented in Figure 5.6 (a). The equivalent circuit for this unit cell is shown in Figure 5.6(b) where CSRR is represented by L_c and C_c and coupled to the line by C. The coupling of the CSRRs to the TL is mainly controlled by its total area. The high-pass characteristic of the BPF is represented by the capacitor C_g . The length of the series gaps located at the input and output is directly related to the value of C_g and optimization is needed to achieve the required frequency response. A narrow-band BPF is designed using one hybrid unit cell with a centre frequency of 2 GHz and a fractional bandwidth of 3%. The simulated s-

parameters results of the filter are presented in Figure 5.7. The simulated group delay results

show that the filter has group delay peak = 3.8 ns at 1.98 GHz as shown in Figure 5.8.

(a)

(b)
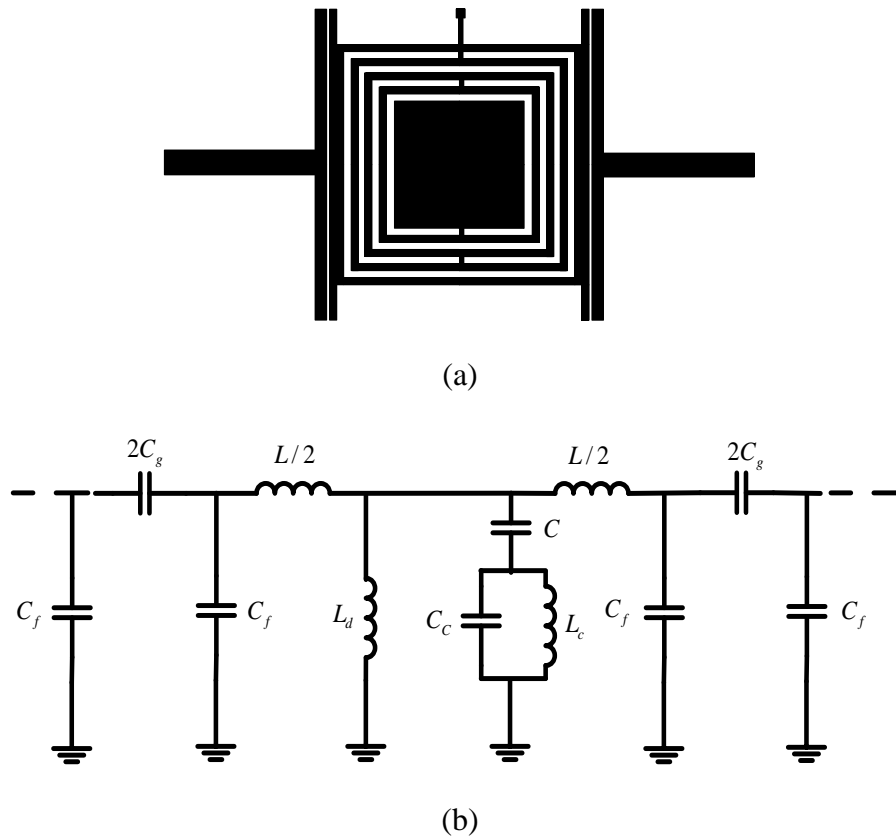
Figure 5.6 Layout of left-handed basic hybrid unit cell (a), and its equivalent circuit model (b) [101]
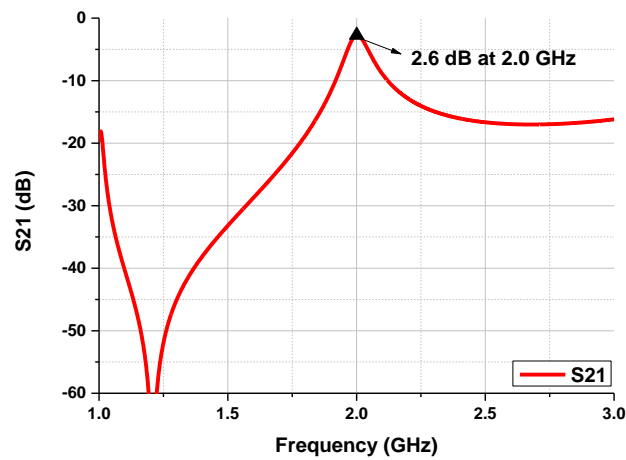
Figure 5.7 Simulated S21 results for the hybrid unit cell**.**
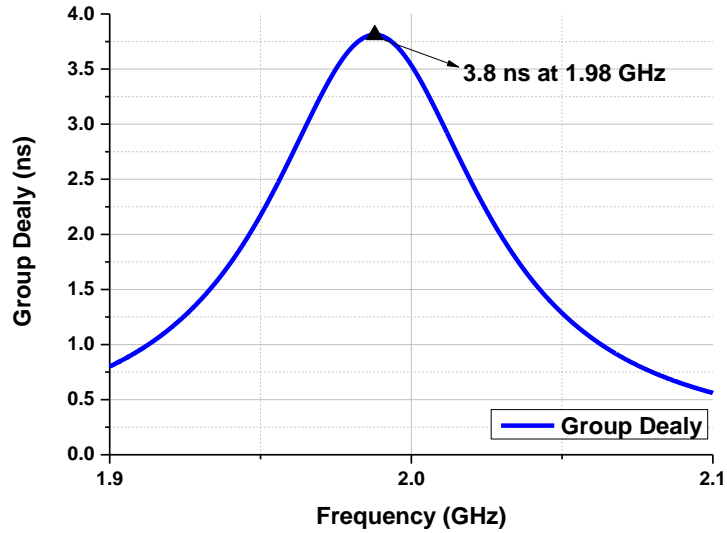
Figure 5.8 Simulated group delay results for the hybrid unit cell.

The sharp selectivity obtained by the CSRR based BPF is mainly attributed to the induced current loops in the rings at the resonance frequency [96]. These current loops are closed through the distributed capacitance between concentric rings. The split-ring resonators can be modelled as resonant tanks (parallel LC) that can be externally driven by a magnetic field.

CSRR resonators of different shapes and numbers of ring slots have different values of equivalent C and L when compared to conventional SRR unit cell. These C and L values will define specific values of Q, loss, and parasitic elements in equivalent network representation. Increasing number of rings will not alter the basic equivalent circuit for CSRR and it can still be considered as parallel LC (LC tank). The confinement of the induced current is due to the effective capacitance between the gaps. The number of the rings in the unit cell can be optimised to achieve the required effective inductance and capacitance. Large group delay is obtained at the passband edge due to the TZ located at 1.75 GHz which suggests that CSRR-based BPF is capable of providing high quality factor. S-parameter retrieval method mentioned in [103] can be used to verify the existence of RH/LH region within the passband, where the sum and difference of scattering coefficients are defined as:

$$V_1 = S_{21} + S_{11}$$

116

$$V_2 = S_{21} - S_{11} \qquad (5.11)$$

V_1 and V_2 are introduced for compactness to simplify the mathematical analysis. The transmission parameter, Z, can be defined as :

$$Z = e^{-jkd} \qquad (5.12)$$

Considering a metamaterial unit cell which has an electrical size smaller than a quarter of guided wavelength, it can be assumed the exponent of Z could be expanded in Taylor series which gives $Z \sim 1 - jkd$ for the first approximation. Permeability and permittivity can be determined using the following approximate formulas:

$$\mu_r \sim \frac{2}{jk_0 d} \frac{1-V_2}{1+V_2} \qquad (5.13)$$

$$\varepsilon_r \sim \frac{2}{jk_0 d} \frac{1-V_1}{1+V_1} \qquad (5.14)$$

where k_0 is the free space complex wave number and *d* is the thickness of the substrate. The results shows that the proposed BPF exhibit a left handed region from 2 to 2.05 GHz and right handed region from 1.96 to 2 GHz as depicted in Figure 5.9.
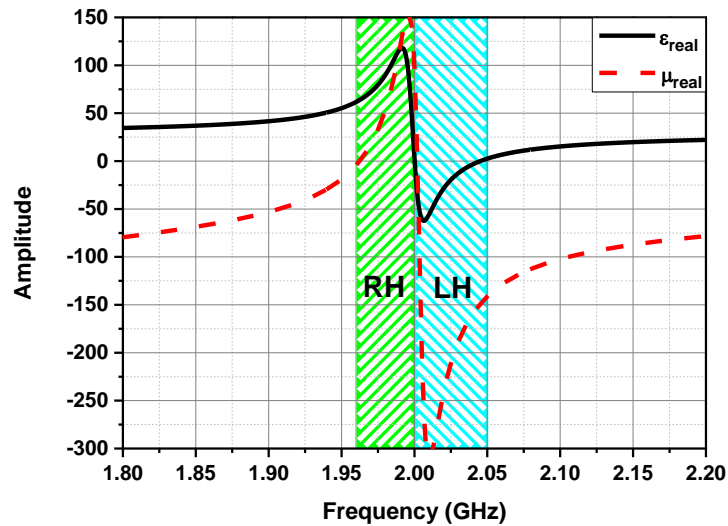
Figure 5.9 Real part of permittivity (ε) and permeability (μ) for CSRR based BPF.

Selectivity improvement of the proposed BPF can be achieved by utilizing two unit cells instead of one which translate to larger group delay peak value assuming weak capacitive coupling exist between the two unit cells as can be seen in Figure 5.10. The simulated S_{21} results show that insertion loss for the one unit cell is -2.6 dB whereas the two unit cells structure has an insertion loss of -3.1 dB. The slight increase in signal losses can be easily compensated by the amplifier used in feedback oscillator design. As amplitude and phase responses in Figure 5.10 and 5.11 reveals, the two unit cell design has a sharper roll-on/off rate compared to the single unit cell, thereby having a higher frequency selectivity. The two unit cell structure layout is shown in Figure 5.12.

There is always a trade-off between group delay, bandwidth and insertion loss for any BPF based on multi-resonators. Group delay can be increased by decreasing the coupling between resonators at the cost of other factors. In oscillator design, insertion loss is more crucial parameter than bandwidth, since insertion loss is directly related with the Q of the resonator, which defines the phase noise performance of the oscillator. It also restricts the minimum allowable coupling between the resonators.
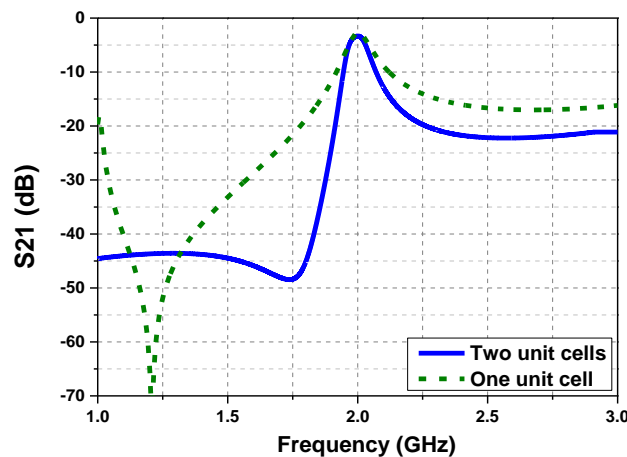
Figure 5.10 Simulated results for S21 for the proposed BPF with one and two unit cells.
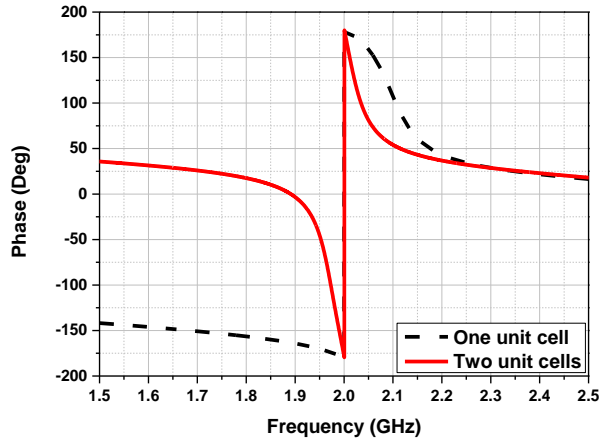
Figure 5.11 Simulated phase response for the proposed BPF with one and two unit cells.

As seen in Equation 5.6, Q_s is based on the derivative of amplitude and phase response of the BPF and high Q_s values are attained where rapid changes in amplitude and phase occur. Simulated group delay and calculated Q_s are plotted in Figure 5.13. It can be seen that high Q_s values coincide with the rapid change in amplitude and phase of the filter response as seen in Figure 5.10 and 5.11. The results show that group delay peak appears very close the first Q_s peak at 1.975 GHz. At 2.05 GHz, where Q_s peaks again, the group delay doesn't peak. These results confirm that Q_s is more accurate definition for the quality factor than Q_r since it account for the combined effects of amplitude and phase change. These two Q_s peaks are related to the derivative of amplitude and phase response of the filter. Using Matlab to calculate Q_s, it can be seen that these peaks are located where amplitude and phase change more rapidly. Q_r takes into account only the group delay of the filter and minimize the phase noise in oscillator design by designing the oscillation frequency at the group delay peak frequency.
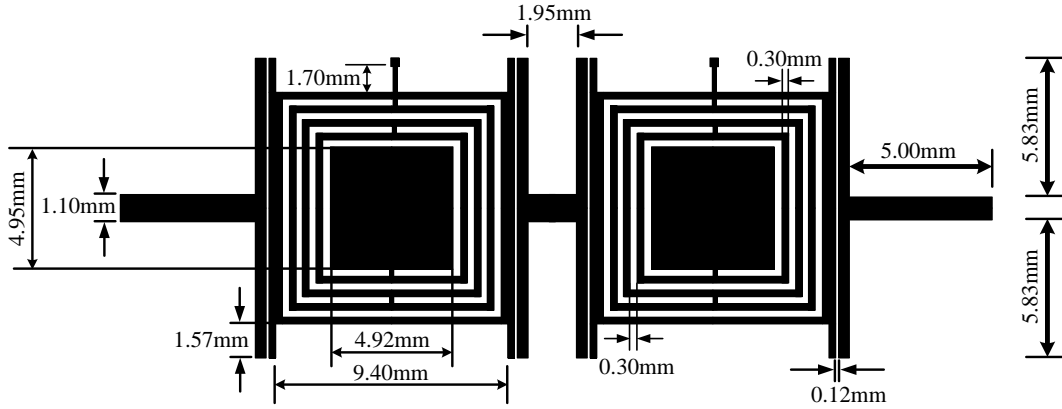
Figure 5.12 Layout of the proposed CSRR based BPF.
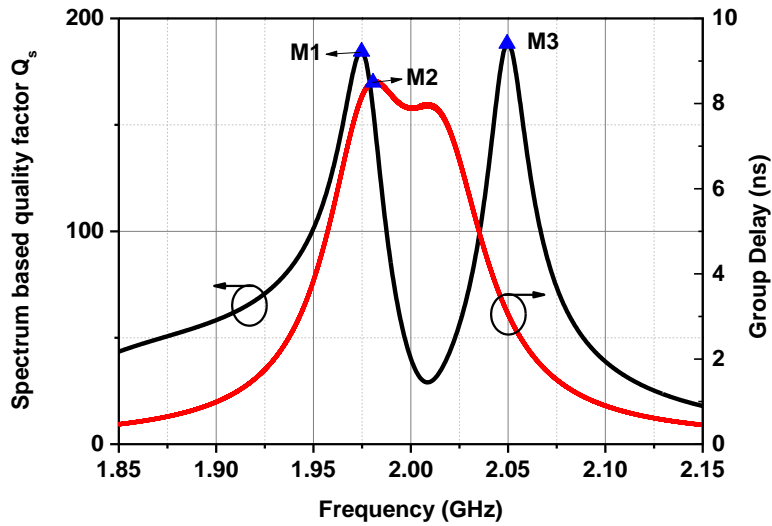
Figure 5.13 Simulated spectrum based quality factor and group delay for the proposed BPF (M1= 184 at 1.975 GHz, M2= 8.6 ns at 1.98 GHz, M3= 188 at 2.05 GHz).

At the edge of the LH region of the BPF, slightly higher Q_s peak is observed which can be clarified by deriving an approximate formula for Q_s in terms of S-parameters. Assuming the proposed BPF is reciprocal and symmetrical 2-port network, the magnitude of Q_s can be defined [90] as

$$|Q_s| = \frac{\omega_0}{2} \left| \frac{d}{d\omega} \left(\ln \frac{Z_{11}}{Z_{12}} \right) \right| \tag{5.15}$$

and the Z parameters of the 2-port network are expressed as

$$Z_{11} = \frac{\left[(1+S_{11})(1-S_{22})+S_{12}S_{21}\right]Z_0}{\left[(1-S_{11})(1-S_{22})+S_{12}S_{21}\right]} \quad (5.16)$$

$$Z_{12} = \frac{2S_{12}Z_0}{\left[(1-S_{11})(1-S_{22})+S_{12}S_{21}\right]} \quad (5.17)$$

where S_{21} and S_{11} are the insertion loss and return loss of the BPF. For a reciprocal 2-port network, it can be assumed that $S_{11}=S_{22}$ and $S_{12}=S_{21}$ and the impedance ratio Z_{11}/Z_{12} is calculated as

$$\frac{Z_{11}}{Z_{21}} = \frac{1-S_{11}^2+S_{21}^2}{2S_{21}} \quad (5.18)$$

Applying equation 5.18 to the proposed BPF, S_{11} and S_{21} can be calculated at $\omega=\omega_0$ as

$$S_{11}(\omega) = S_{11}(\omega_0) + \frac{d}{d\omega}S_{11}(\omega_0) \quad (5.19)$$

$$S_{21}(\omega) = S_{21}(\omega_0) + \frac{d}{d\omega}S_{21}(\omega_0) \quad (5.20)$$

where ω_0 denote the centre frequency of the BPF and by assuming the following conditions:

$$|S_{11}|(\omega_0) \square\ 1, \ \frac{d}{d\omega}|S_{11}|(\omega_0) \square\ 1$$

$$|S_{21}|(\omega_0) = \text{Insertion loss=IL}, \ \frac{d}{d\omega}|S_{21}|(\omega_0) \square\ 1$$

$$\frac{d}{d\omega}\arg(S_{21}) at \omega_0 = \text{-group delay=-}\tau_g$$

Using equations (5.15) and (5.18), Q_s can be defined as

$$|Q_s| = \frac{\omega_0}{2}\left|\frac{d}{d\omega}\left(\ln\frac{1-S_{11}^2+S_{21}^2}{2S_{21}}\right)\right| \quad (5.21)$$

Since both S_{11} and S_{21} are complex numbers, the derivative for these coefficients can be calculated as

$$S'_{11} = e^{-(jArg(S_{11}))}.|S_{11}|' + j.e^{(Arg(S_{11}))}.|S_{11}|.(Arg(S_{11}))'$$

$$S'_{21} = e^{-(jArg(S_{21}))}.|S_{21}|' + j.e^{(Arg(S_{21}))}.|S_{21}|.(Arg(S_{21}))'$$

Assuming $|S_{11}| \ll 1, |S_{11}|' \ll 1, |S_{21}| \ll 1$ (*low insertion loss*), S'_{21} is reduced to

$$S'_{21} = j.e^{(Arg(S_{21}))}.|S_{21}|.(Arg(S_{21}))'$$

Now, we take the derivative of (5.20), we have

$$Q_s = -\frac{\omega_0}{2}\frac{S'_{21}}{S_{21}} = -\frac{\omega_0}{2}\frac{j.e^{(Arg(S_{21}))}.|S_{21}|.(Arg(S_{21}))'}{|S_{21}|.e^{(Arg(S_{21}))}} = \frac{\omega_0}{2}.(Arg(S_{21}))'$$

$(Arg(S_{21}))'$ is basically the group delay [104] which is related to group velocity by the following formula

$$(Arg(S_{21}))' = \frac{L_T}{v_g} \tag{5.22}$$

where v_g is the group velocity and L_T is the electrical length of the 2-port network.

Hence, an approximate formula for Q_s is derived as:

$$|Q_s| \cong \frac{\omega_0}{2}\frac{L_T}{v_g} \text{ at } \omega = \omega_0 \tag{5.23}$$

Low group velocity is usually associated with electromagnetic propagation within the LH region in CRLH TL based structures [105]. Thus, higher Q_s value is obtained at the edge of the LH region of the proposed BPF.

5.3.2 Oscillator design at group delay and Q_s peak frequencies

The basic elements needed to construct a filter based oscillator are an amplifier and a BPF. An Infineon BFP405 bipolar transistor biased at $V_{cc}= 2.135$ V with a collector current $I_c= 2.85$ mA was used to realise the amplifier as seen in Figure 5.14. This kind of transistor is suitable for oscillator design up to 12 GHz [106]. DC blocking is provided by the two 560pF capacitors, while a third capacitor of the same value is utilized within the shorted stub for low impedance pass to ground. Biasing resistors with the values of 51 Ohm and 5 KOhm are used for the DC biasing circuit. These bias resistors are selected to be similar to [90] so that similar gain characteristics are obtained from the oscillator. Moreover, the effect on phase noise performance can be easily observed when similar biasing circuit is used while replacing only the conventional BPF used in [90] with CRLH TL based BPF. The width of the connecting microstrip transmission line is easily determined by considering the analytical line impedance at the centre frequency of the LH BPF. Using Taconic RF-35 substrate, with a thickness of 0.508 mm and a loss tangent of 0.0018 and dielectric constant of 3.5, the width of the connecting lines is chosen to be 1.1 mm to reach 50 ohm characteristic impedance.
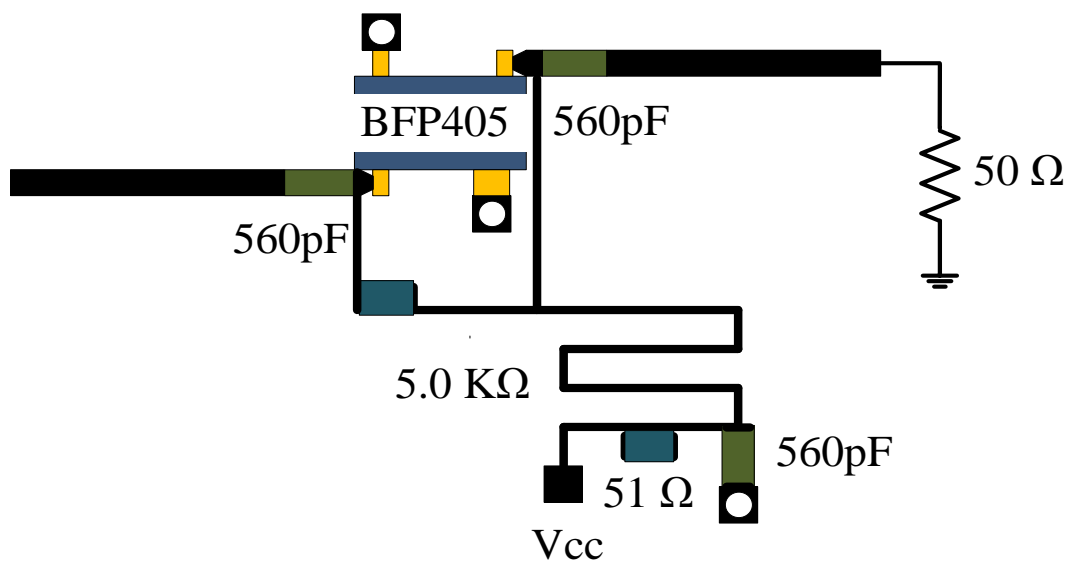
Figure 5.14 Amplifier used in the oscillator design.

To ensure oscillation, the total loop phase should be 0° or multiple of 360° as stated earlier. Thus, the total phase response from port 1 to port 2, phase (S21), should be determined first by connecting the BPF, the amplifier and parts of the connecting lines as shown in Figure 5.15.
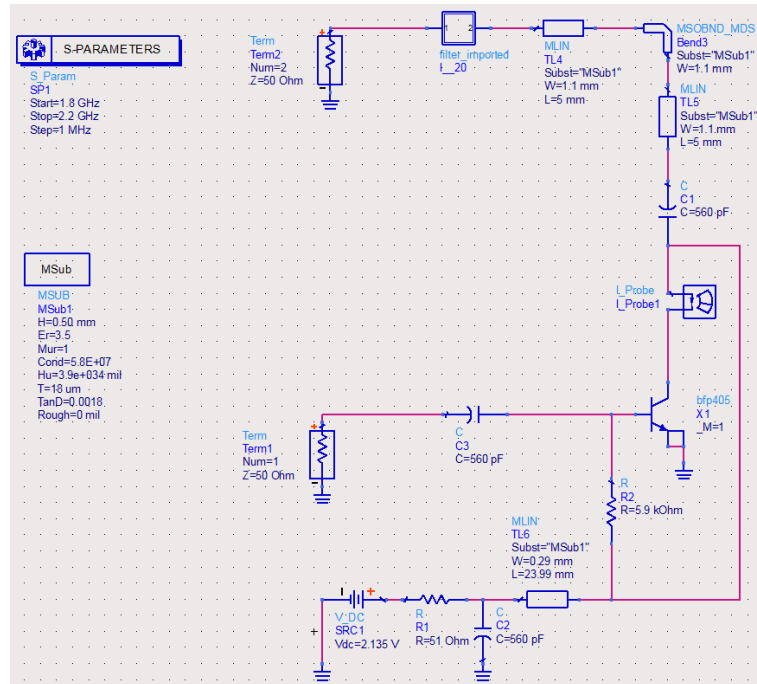
Figure 5.15 Schematics of the BPF with the amplifier, parts of connecting lines.

Figure 5.16 shows the phase response of the amplifier, including the BPF and part of the connection lines. The phase values at Q_s and group delay peak frequencies are used to determine the length of TL needed to connect port 1 to port 2. This can be easily calculated by subtracting 360° from each phase value to ensure Barkhausen oscillation condition for total phase loop is met.
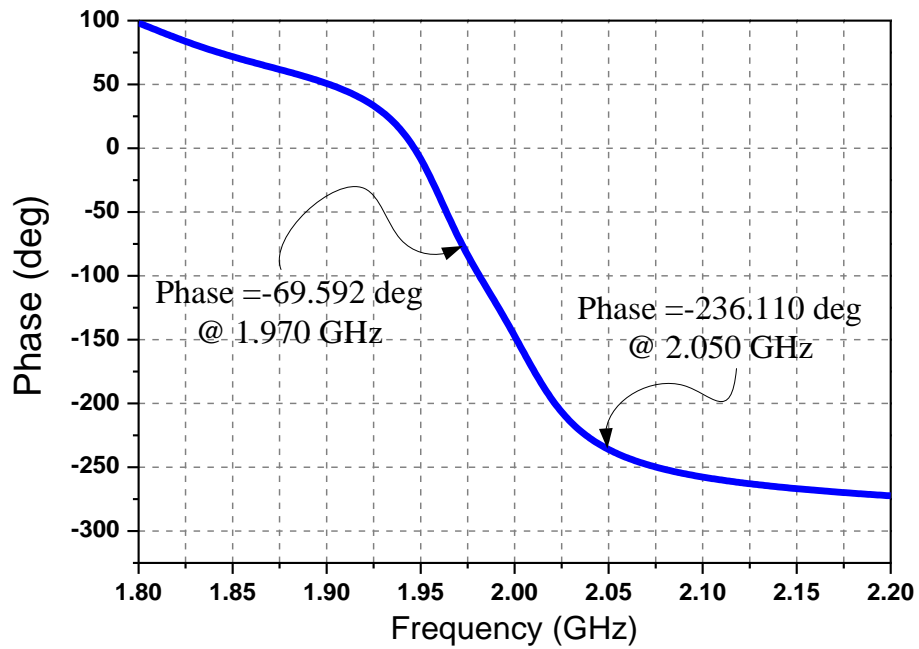
Figure 5.16 Phase response of the amplifier with the BPF and parts of connecting lines.

The schematic of the proposed oscillator at Q_s peak frequency, 2.05 GHz, is presented in Figure 5.17. Circuit simulation was obtained using Advanced Design System (ADS) oscport module within Harmonic balance (HB) solver [107], as seen in Figure 5.18. HB solver is based on both time and frequency domain analysis used to simulate distortion in nonlinear systems. RF/microwave engineers can use this solver to simulate oscillators and acquire useful results such oscillation frequency, power spectrum, and phase noise.
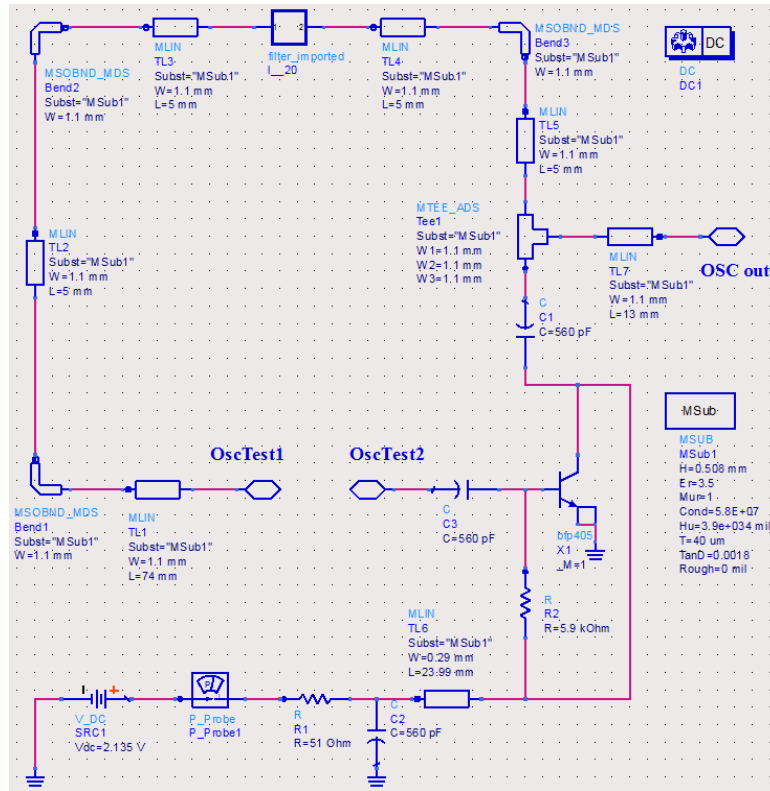
Figure 5.17 Schematic of the proposed oscillator**.**
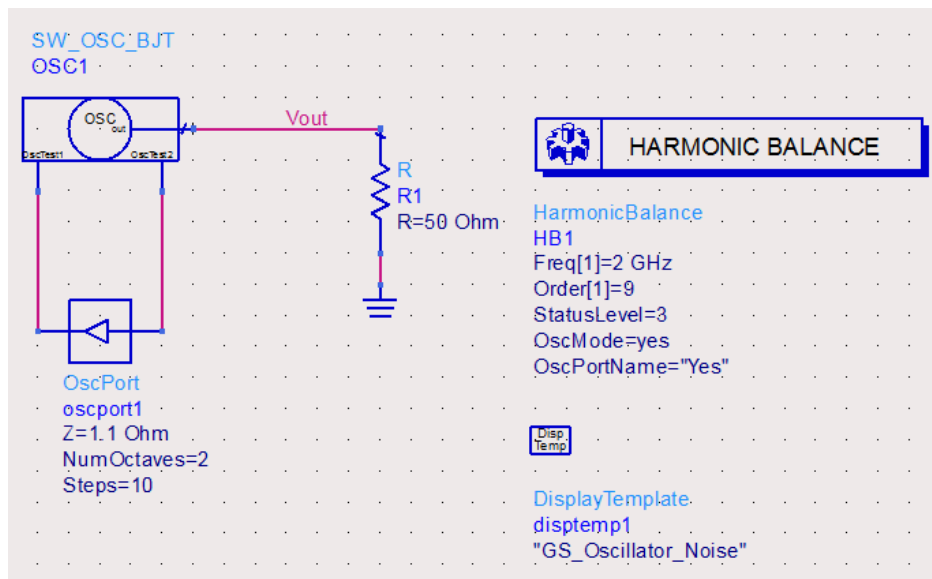
Figure 5.18 Schematic of oscport module using Harmonic balance (HB) solver.

The proposed oscillator was firstly designed at Q_s peak where an output power of 4.8 dBm is

obtained as shown in Figure 5.19. Using 2.135 V DC supply, the total DC power consumption

is 6.1 mW. The simulated phase noises are – 126 dBc/Hz and -152.1 dBc/Hz at 100-kHz and

126

1-MHz offset frequencies, respectively, as indicated in Figure 5.20. In order to assess the performance of the oscillator, a performance figure called figure of merit (FOM) is defined, according to [108]. This number is the combination of phase noise, frequency and the power output of the oscillator. The FOM of an oscillator can be calculated by:

$$FOM = L(\Delta f) - 20 \log\left(\frac{f_0}{\Delta f}\right) + 10 \log\left(\frac{P_{dc}}{1\,mW}\right) \qquad \text{(dBc/Hz)} \qquad (5.24)$$

where $L(\Delta f)$ is the phase noise at the offset frequency Δf, f_0 is the oscillation frequency, and P_{dc} is the DC power consumption (in milliwatts). The FOM of the proposed oscillator at 1-MHz offset frequency is -207 dBc/Hz. These simulation results show promising phase noise results which confirms that high Q_s value is achieved by utilizing CRLH TL based BPF.
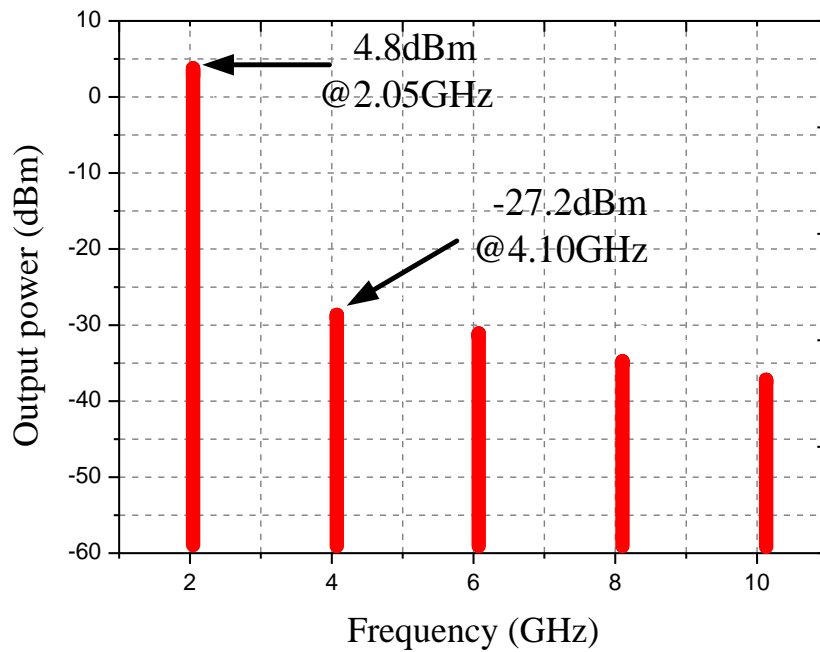
Figure 5.19 Simulated output power for the proposed oscillator at Qs peak frequency.
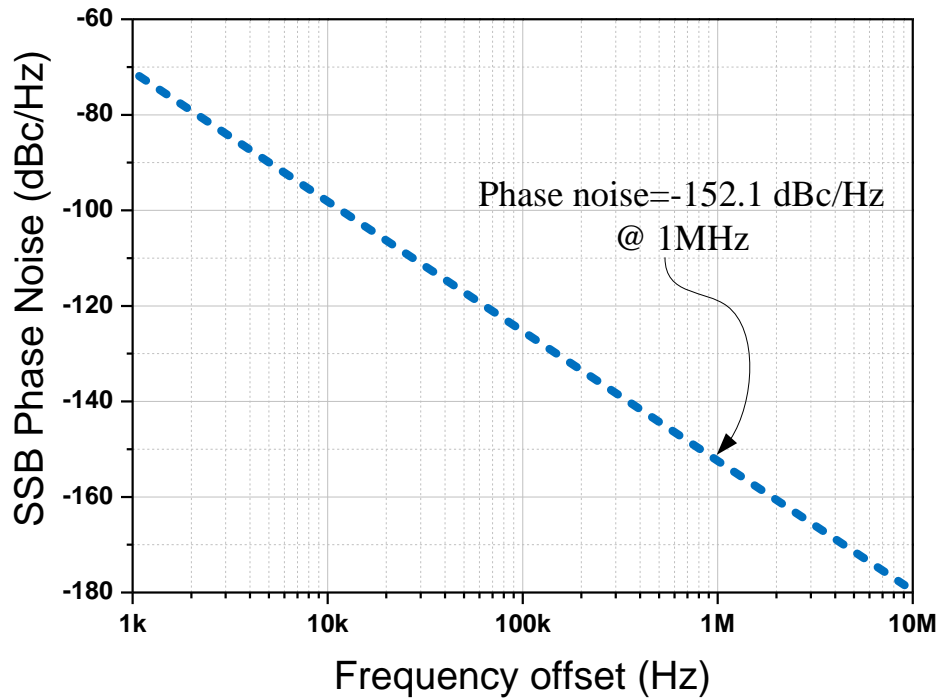
Figure 5.20 Simulated phase noise for the proposed oscillator at Qs peak frequency.

For completeness, the oscillator was designed to oscillate at group delay peak, namely 1.971 GHz, by modifying the length of the connecting TL between port 1 and port 2 as shown in Figure 5.21. The simulation results show that the output power is reduced to 2.168 dBm at group delay peak frequency as shown in Figure 5.22.
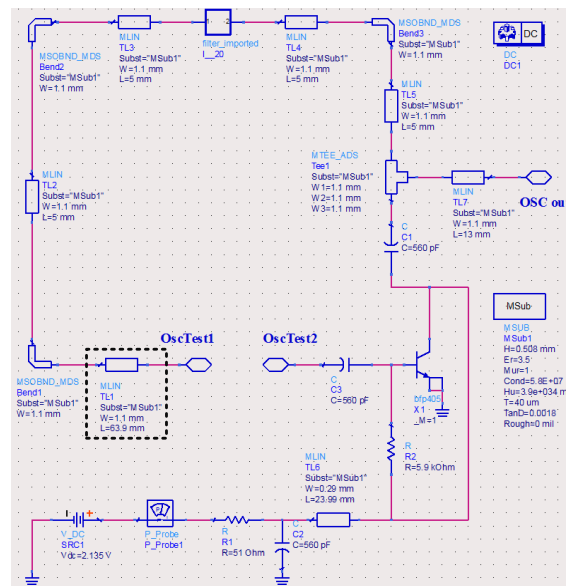
Figure 5.21 Schematic of proposed oscillator at group delay peak frequency.
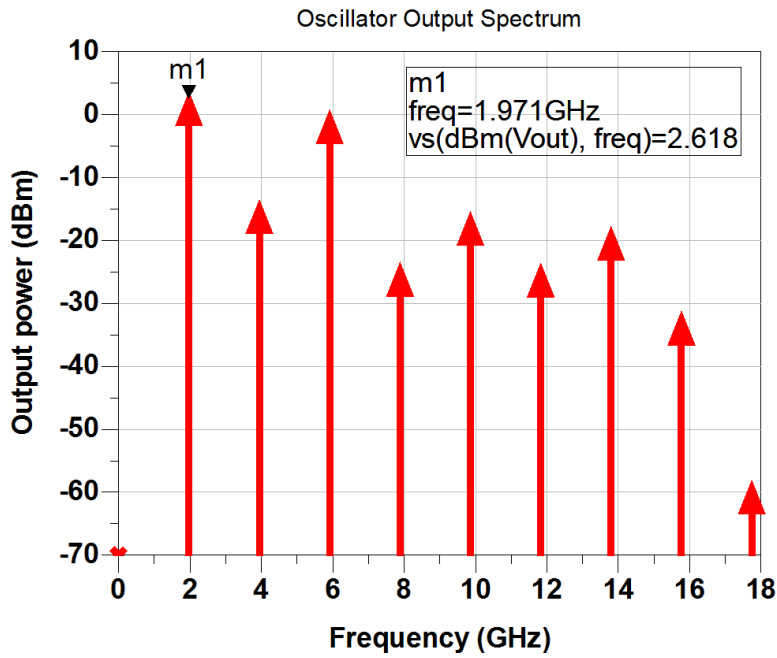
Figure 5.22 Simulated output power for the proposed oscillator at group delay peak frequency.

The simulated phase noises are -116.1 dBc/Hz and -142.5 dBc/Hz at 100-kHz and 1-MHz offset frequencies, as presented in Figure 5.23. It can be concluded that designing the oscillator at Q_s peak frequency can improve the phase noise results by 10 dB as compared with the oscillator designed at the group delay peak frequency.
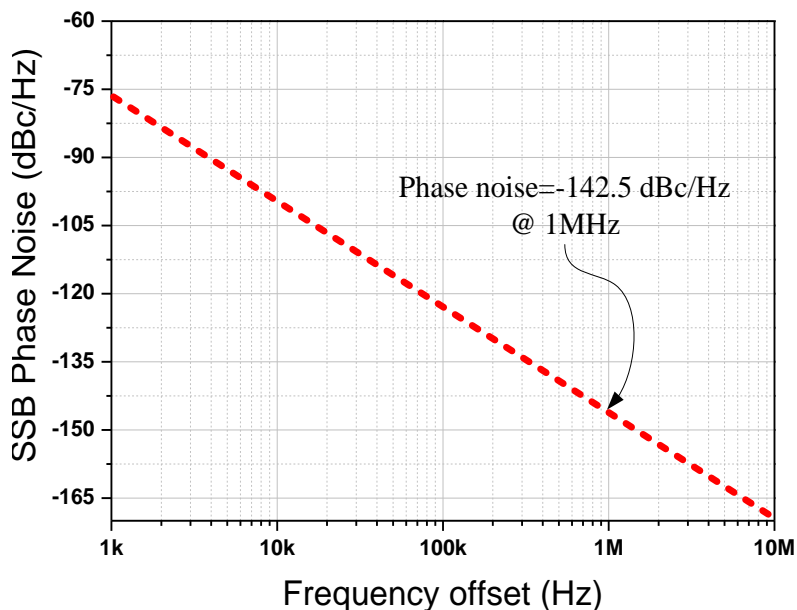
Figure 5.23 Simulated phase noise for the proposed oscillator at group delay peak frequency.

The layout of the proposed oscillator is presented in Figure 5.24. The substrate used to fabricate the BPF and connecting lines is Taconic RF-35 substrate, with a thickness of 0.508 mm, a loss tangent of 0.0018 and a dielectric constant of 3.5. The fabricated oscillator is shown in Figure 5.25. Agilent E5052B source signal analyzer was used to measure the oscillator's performance. The measured output power of the proposed oscillator is 3.4 dBm at an oscillation frequency of 2.05 GHz, as presented in Figure 5.26. The overall DC power consumed is 6.1 mW from a 2.135V DC supply. The measured phase noise of the filter based oscillator is -126 dBc/Hz at a 100-kHz offset frequency, as shown in Figure 5.27. The FoM of the oscillator at a 1 MHz offset frequency is -207.2 dBc/Hz.
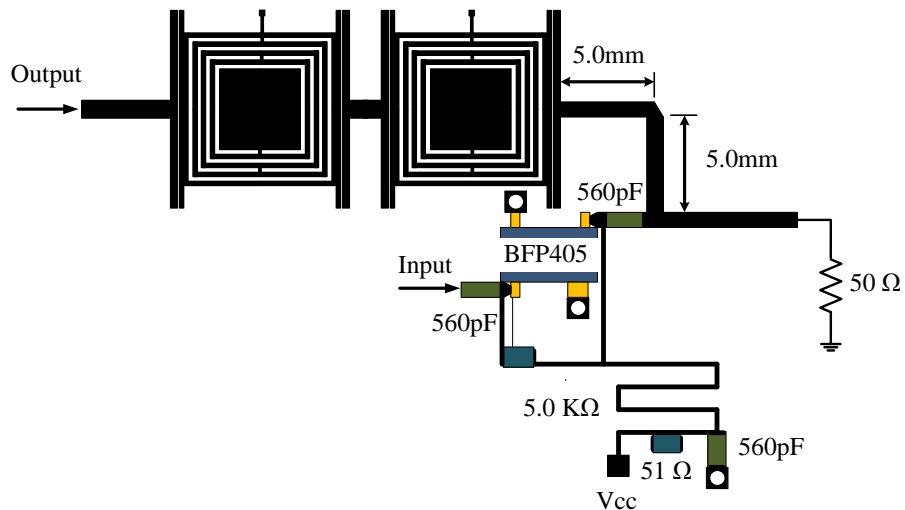
Figure 5.24 Layout of proposed filter based oscillator.
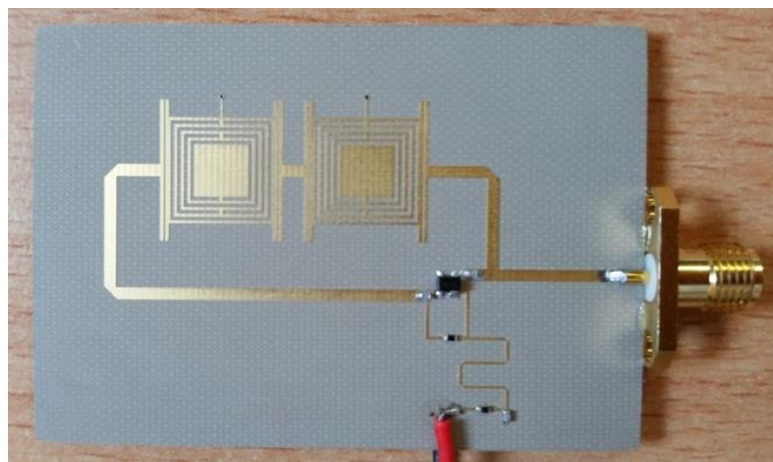
Figure 5.25 Photograph of fabricated filter based oscillator.
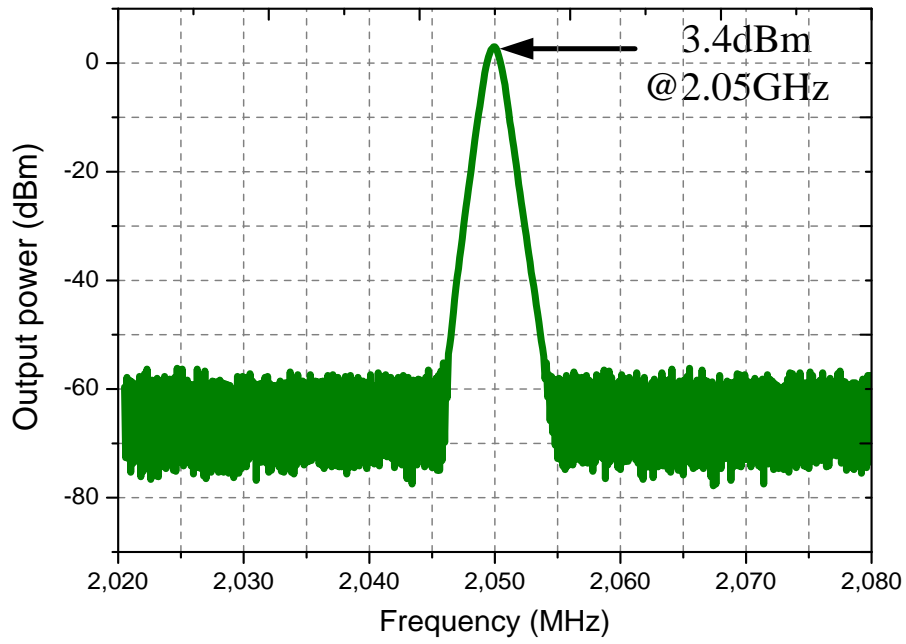
Figure 5.26 Measured output spectrum of the proposed oscillator.
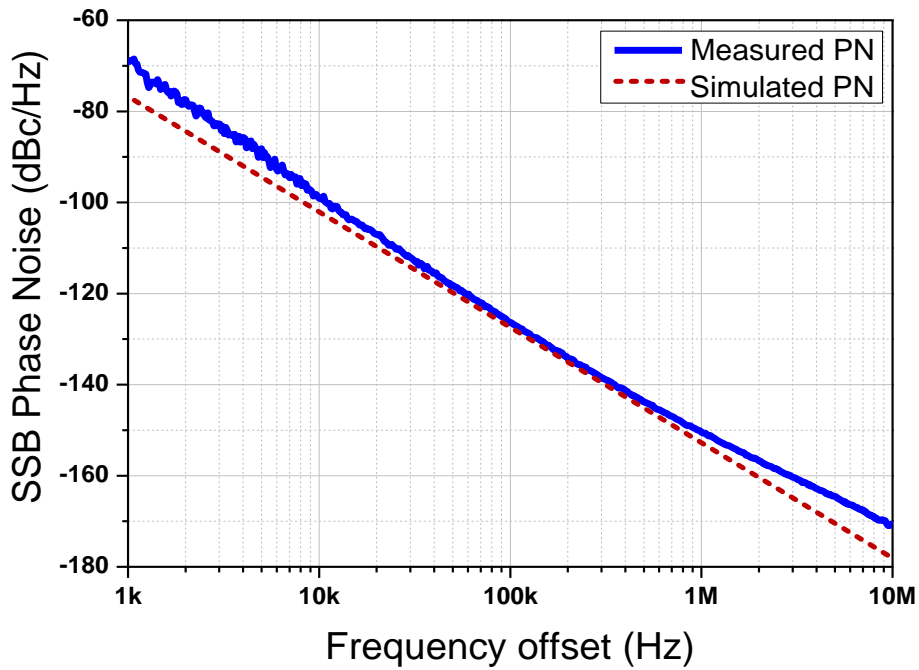
Figure 5.27 Phase noise simulation and measurement results for the L-band oscillator.

To the best of the author knowledge, currently there are no published planar filter based oscillator designs attaining similar performance with similar DC bias level. Table 5.1 compare the performance of the proposed oscillator design with other state-of-the-art designs. It shows clearly that the proposed design is the best in terms of phase noise and FoM.

In [109], high Q-tunable substrate integrated waveguide (SIW) resonator is used to design a low phase noise VCO. The high Q-tunable SIW resonator was constructed using a simple coupling varactor structure to avoid the use of bonding wire. The suggested resonator has unloaded Q variation from 286 to 299 with almost 500 MHz tuning range at X-band. Using such resonator, the authors were able to obtain a low phase noise of -93 to -95.6 dBc/Hz at 100 kHz offset frequency while changing the oscillation frequency from 11.16 GHz to 11.62 GHz.

Microstrip trisection bandpass filter is employed as a frequency stabilization element to design a feedback oscillator in [110]. Single group delay peak is obtained using this filter since it can generate single transmission zero near the passband. By designing the oscillation frequency at the group delay peak, the phase noise of the oscillator is significantly reduced. The measured phase noise of the trisection BPF based oscillator is -120 dBc/Hz at an offset frequency of 100 kHz with an oscillation frequency of 2.46 GHz.

An X-band low phase noise oscillator is constructed using SIW dual-mode BPF with circular cavity in [97]. BPF based on SIW technology can provide higher quality factor than microstrip BPFs which is a major factor in reducing phase noise in oscillator design at microwave frequencies. Moreover, one large group delay peak is achieved near the upper passband to eliminate the design uncertainty introduced within elliptic-response BPF since two group delay peaks are attained at the passband edges. Insertion loss of the SIW BPF is another parameter that influences the phase noise performance in oscillator design. Group delay is enlarged at the cost of increasing the insertion loss of the filter. Hence, the proposed SIW BPF was optimized to achieve acceptable level of insertion loss and largest group delay value to reduce the phase noise.

One unit cell of CRLH TL is used in to design a hairpin-shaped resonator in [111] to construct a low phase noise oscillator. Slow wave propagation property of the CRLH TL allows the reduction of the radiation loss to increase the Q-factor. Compact circuit size and high Q-factor

are two of the main requirements in planar oscillator design to reduce the fabrication cost and obtain low phase noise level. The proposed oscillator design was fabricated and the measurement results show that it oscillate at a frequency of 4.95 GHz and phase noise of -120.5 was attained at 100 kHz offset frequency with FOM of -206.3.

Table 5.1 Performance comparison between proposed oscillator and published oscillators.

Reference	Resonator/ Filter	F (GHz)	P_{DC} (mW)	P_0 (dBm)	PN (dBc/Hz)	FoM (dBc/Hz)
[109]	SIW	11.4	20.00	2.60	-95.6	-193.1
[110]	Trisection	2.46	6.40	6.39	-120.4	-195.8
[90]	Combline	2.04	22.00	-0.68	-125.6	-201.1
[97]	Dual Mode SIW	11.6	11.40	-2.30	-117.3	-206.2
[111]	Hairpin	4.95	6.40	4.93	-120.5	-206.3
This work	CRLH TL	2.05	6.10	3.40	-126.7	-207.2

5.4 Chapter summary

In this chapter, high selectivity CRLH TL based BPF was utilized to design a novel low phase noise free-running oscillator. The CRLH TL BPF is constructed using CSRRs with capacitive gaps and short circuited stub. Presence of TZ within the lower stopband and the use of two unit cells instead of one facilitated the selectivity improvement of the proposed BPF.

The spectrum based quality factor Q_s for CRLH TL based BPF was explored and thoroughly studied. Both amplitude and phase response of the BPF is taken into account in Q_s which is more rigorous definition than conventional Q-factor definition. 3D EM Simulation results show that higher Q_s peak is achieved within the LH region when compared to the RH region.

133

An expression for Q_s in terms of S-parameters was derived and it was found that Q_s is inversely related to group velocity. Due to slow-wave property of LH TL, high Q_s peak value is obtained within the LH region. Based on the analysis of Q_s for the proposed BPF, a free-running oscillator has been designed to provide the lowest phase noise performance among latest planar BPF based oscillators reported in the literature working in the L-band with similar DC bias level.

The measured results reveal that the fabricated oscillator has better performance and significantly decreases phase noise compared to other reported BPF based oscillator. The proposed design has measured phase noise of -126.7 dBc/Hz at an offset frequency of 100 KHz away from 2.05 GHz, an FoM of -207.2 dBc/Hz, while the oscillator core's total power consumption is 6.1 mW from a 2.135V DC supply.

Chapter 6: Bandpass Filter Design Based on Feedback Signal Interference

6.1 Introduction

Bandpass filters with exceptional performance and compact size are essential in existing and next generation wireless front ends. Due to the crowded microwave frequency spectrum, sharp skirt and wide stopband are two crucial features needed in BPF design. Conventional BPFs using edge coupled-lines [23] are widely used because of their simple designing procedures using microstrip and stripline technologies [10, 112]. However, the selectivity of a conventional coupled-line BPF can be only improved by increasing the order of the filter which introduces additional insertion loss and enlarge circuit size. Moreover, it suffers from harmonic responses generated at multiple of the centre frequency due to the inherent nature of the distributed resonators used in any TL based BPFs [113].

Different approaches have been suggested by researchers to achieve wide harmonic suppression [52, 114-118]. In [114], the second harmonic resonance of a parallel coupled microstrip BPF is suppressed by using the over-coupled end stage approach. Cascading a low-pass filter (LPF) with a cross-coupled BPF is proposed in [115] to suppress the second and third harmonics. Good rejection level is achieved using the proposed LPF at the expense of higher insertion loss and larger circuit size. In [52], a stepped impedance edge-coupled microstrip BPF is constructed using three coupled-line sections with different electrical lengths and coupling factors to obtain a wide upper stopband. To reduce the filter footprint, a quarter-

wavelength stepped coupled-line coupler is used in [116] where different coupling strengths provided by the proposed structure enabled the suppression of third and fifth harmonics. Moreover, two short-circuited stubs are utilized at the input and output port to improve the selectivity of the filter. Even though these methods provide good stopband performance, the physical size of these BPFs are relatively large since additional circuitry is required. In [118], discriminating coupling between feeding lines and resonators is employed to design wide-stopband BPF using low-temperature co-fired ceramic (LTCC) technology. Although, third and fifth harmonics are suppressed, a complicated design process is required with 10 metal layers.

Other works focused on selectivity improvement of BPF design without increasing insertion loss to mitigate the drawback of conventional BPF design [119-121]. The filtering structure presented in [119] consisted of two TL sections connected in parallel and coupling is avoided to minimize the insertion losses. Hence, multiple TZs within lower and upper stopbands are generated due to destructive signal interference to improve the selectivity of the BPF. Moreover, constructive signal combination at the passband limits the degradation of passband performance and low insertion loss is achieved. The theory behind the proposed BPF was validated through a design example with a center frequency of 5 GHz and 3-dB fractional bandwidth of 27.6%. High selectivity with an insertion loss of less than 1 dB can be achieved using this approach but the circuit size is relatively large. In [120], transversal signal-interaction concept is used to design fifth-order high selectivity BPF with multiple TZs in the lower and upper stopband. The BPF is constructed using two electrical paths which consist of a shorted stub and two open coupled-lines. Due to the two transmission paths, ten TZs are realized within the stopbands which mainly contributed to selectivity improvement of the BPF at the expense of moderate upper stopband bandwidth.

High selectivity wideband BPF is presented in [121] where composite short- and open-circuited stubs are utilized to generate two pairs of TZs within lower and upper stopband. Stepped impedance multi-mode resonator (MMR) and composite stubs are used to construct the proposed BPF. TZs can be generated at multiple integer of π using grounded stubs at both sides of the MMR which can be shifted near the passband using two section open circuited stubs. Although good selectivity is achieved, relatively large circuit size is needed due to the use of different kind of stubs.

In this chapter, two new BPF designs are presented based on the feedback signal interference concept. Feedback circuitry is usually employed in active components such as oscillators [122], amplifiers [123], and active filters [124]. It is used to control circuit characteristics, reduce signal distortion, and adjust frequency response according to communication system requirements [125]. Signal interference feedback for low-pass filter (LPF) design was introduced in [126] to achieve high stopband rejection. To the best of the authors' knowledge, BPF design based on the signal interference feedback concept has never been reported in the literature. It is worth to point out that the mechanism of signal interference feedback is very different to that of conventional signal interference concept. Filters based on signal interference are constructed using two or more forward electrical paths to enhance passband/stopband performance [71, 127, 128]. The first BPF design proposed in this chapter consists of two broad-side coupled-lines coupler and another coupled-line coupler open circuited at the opposite ends in the feedback circuit. By carefully choosing the appropriate electrical length ratio between the couplers in the main signal path and in the feedback, different number of TZs can be produced to realize a wide-stopband BPF.

The second design that will be discussed in this chapter is a high selectivity microstrip BPF using feedback signal interference where CRLH TL unit cell was used in the feedback circuit. By controlling the coupling factor of the coupled-line utilized in the main signal path, the

selectivity of the BPF is significantly improved without introducing substantial increase in the insertion loss.

 The remainder of this chapter is structured as follows. Section 6.2 covers the theoretical analysis and harmonic suppression mechanism for the first BPF design. Design methodology for the wide-stopband BPF is discussed in section 6.2.4 while a fabricated design example is illustrated in section 6.2.5. The concept of selectivity improvement using CRLH TL unit cell in the feedback is described in section 6.3. Final remarks and conclusions are stated in section 6.4.

6.2 Wide-Stopband BPF Design Using Feedback Signal Interference

The basic structure for the signal interference feedback coupled-line BPF is shown in Figure 6.1, where a pair of coupled-line couplers is used in the main signal path and feedback, respectively. The characteristic impedances (Z_m, Z_f) and coupling factors (k_m, k_f) for the coupled-line couplers [11] can be defined as:

$$Z_m = \sqrt{Z_m^e Z_m^o} \tag{6.1}$$

$$Z_f = \sqrt{Z_f^e Z_f^o} \tag{6.2}$$

$$k_m = \frac{Z_m^e - Z_m^o}{Z_m^e + Z_m^o} \tag{6.3}$$

$$k_f = \frac{Z_f^e - Z_f^o}{Z_f^e + Z_f^o} \tag{6.4}$$
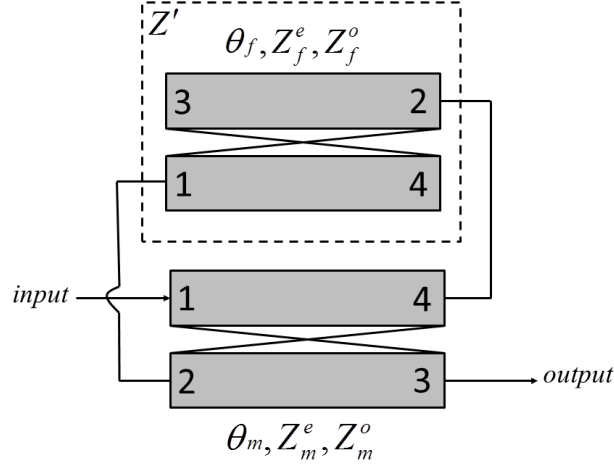
Figure 6.1 Ideal transmission line model for the proposed feedback BPF.

where (Z_m^e, Z_m^o) and (Z_f^e, Z_f^o) are the even- and odd-mode impedances for the main and feedback coupled-line couplers, respectively. Assuming the structure is symmetrical, reciprocal and lossless with non-dispersive propagation, the Z-matrix for the main coupled-line coupler can be expressed as follows [11]:

$$\begin{pmatrix} V_1 \\ V_2 \\ V_3 \\ V_4 \end{pmatrix} = \begin{pmatrix} Z_{11} & Z_{12} & Z_{13} & Z_{14} \\ Z_{21} & Z_{22} & Z_{23} & Z_{24} \\ Z_{31} & Z_{32} & Z_{33} & Z_{34} \\ Z_{41} & Z_{42} & Z_{43} & Z_{44} \end{pmatrix} \begin{pmatrix} I_1 \\ I_2 \\ I_3 \\ I_4 \end{pmatrix} \tag{6.5}$$

And the Z matrix coefficients are

$$Z_{11} = Z_{22} = Z_{33} = Z_{44} = -j\frac{Z_m^e + Z_m^o}{2}\frac{\cos\theta_m}{\sin\theta_m}$$

$$Z_{12} = Z_{21} = Z_{34} = Z_{43} = -j\frac{Z_m^e - Z_m^o}{2}\frac{\cos\theta_m}{\sin\theta_m}$$

$$Z_{13} = Z_{31} = Z_{24} = Z_{42} = -j\frac{Z_m^e - Z_m^o}{2}\frac{1}{\sin\theta_m}$$

$$Z_{14} = Z_{41} = Z_{23} = Z_{32} = -j\frac{Z_m^e + Z_m^o}{2}\frac{1}{\sin\theta_m} \tag{6.6}$$

Where θ_m denote the electrical length for the main coupled-line coupler. The feedback coupled-line coupler that is open-circuited at the opposite ends can be considered as two-port circuit as shown in Figure 6.2.
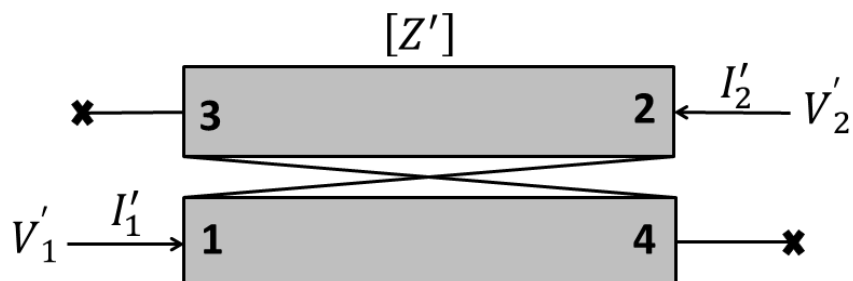
Figure 6.2 Feedback coupled-line coupler.

The Z-matrix for the feedback coupled can be expressed as

$$\begin{pmatrix} V_1' \\ V_2' \end{pmatrix} = \begin{pmatrix} Z_{11}' & Z_{12}' \\ Z_{21}' & Z_{22}' \end{pmatrix} \begin{pmatrix} I_1' \\ I_2' \end{pmatrix} \tag{6.7}$$

Considering that $Z_{11}' = Z_{22}'$ and $Z_{21}' = Z_{12}'$ for reciprocal, symmetrical, and lossless circuit, the Z-parameters can be expressed as follows:

$$Z_{11}' = -j \frac{Z_f^e + Z_f^o}{2} \frac{\cos\theta_f}{\sin\theta_f}$$

$$Z_{12}' = -j \frac{Z_f^e - Z_f^o}{2} \frac{1}{\sin\theta_f} \tag{6.8}$$

where θ_f is the electrical length of the feedback coupled-line coupler. Since two matrices have been obtained for the two couplers, the Z-matrix for the whole structure can be obtained by considering the 2-port circuit shown in Figure 6.3.
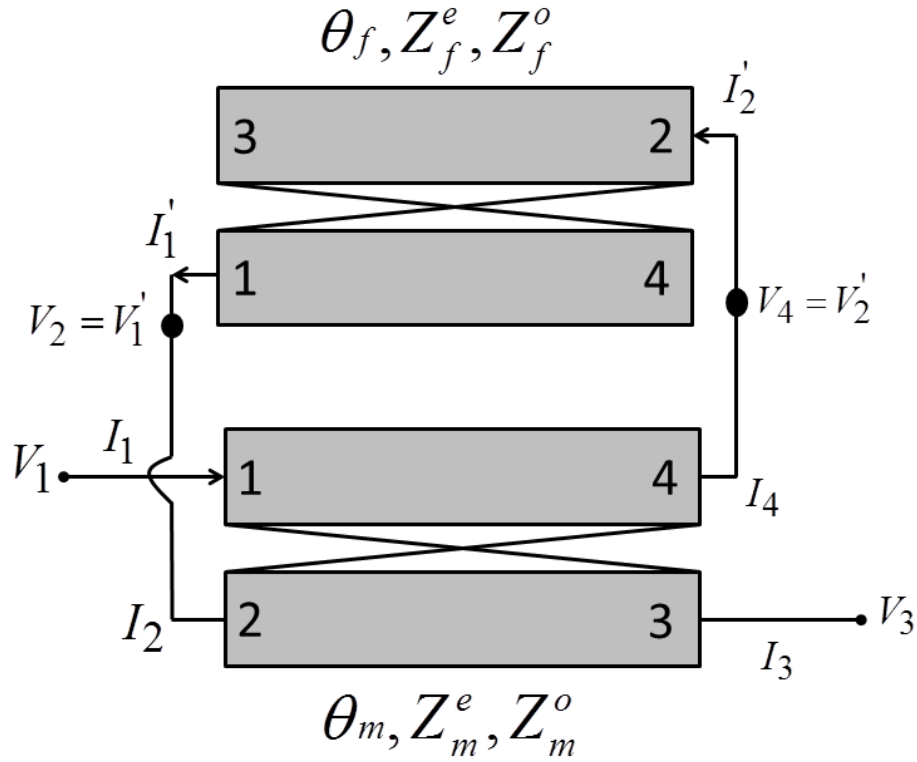
Figure 6.3 BPF design using two coupled-line couplers with currents and voltages definitions.

As shown in Figure 6.2, it can be assumed that:

$$I_1' = -I_2 \qquad V_1' = V_2$$

$$I_2' = -I_4 \qquad V_2' = V_4$$

The equations for the main and feedback couplers can be collected in one set as:

$$\begin{cases} V_1 = Z_{11}I_1 + Z_{12}I_2 + Z_{13}I_3 + Z_{23}I_4 \\ V_2 = Z_{12}I_1 + Z_{11}I_2 + Z_{14}I_3 + Z_{13}I_4 \\ V_3 = Z_{13}I_1 + Z_{14}I_2 + Z_{11}I_3 + Z_{12}I_4 \\ V_4 = Z_{14}I_1 + Z_{13}I_2 + Z_{12}I_3 + Z_{11}I_4 \\ \qquad V_2 = -Z_{11}'I_2 - Z_{12}'I_4 \\ \qquad V_4 = -Z_{12}'I_2 - Z_{11}'I_4 \end{cases}$$

Let's consider a generic passive, symmetrical, reciprocal, lossless, two-port circuit as shown in Figure 6.4.
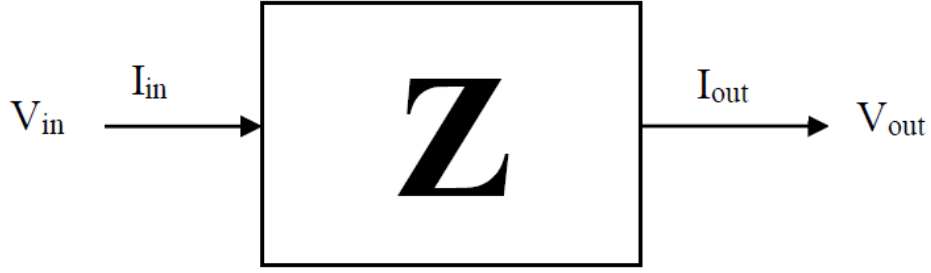
Figure 6.4. Generic passive two-port circuit.

The Z-parameters of the simple structure shown above can be expressed as:

$$Z_{11} = Z_{22} = \left(\frac{V_{in}}{I_{in}}\right)_{I_{out}=0} \tag{6.9a}$$

$$Z_{21} = Z_{12} = \left(\frac{V_{in}}{I_{out}}\right)_{I_{in}=0} \tag{6.9b}$$

Applying (6.9a and 6.9b) to Figure 6.3, we can obtain

$$I_{in} = I_1$$

$$I_{out} = I_3$$

$$V_{in} = V_1$$

$$V_{out} = V_3$$

Using (6.5), (6.7), (6.9a) and algebraic simplification, Z_{11}^T and Z_{21}^T can be obtained for the filtering structure as

$$Z_{11}^T = Z_{22}^T = \left(\frac{V_{in}}{I_{in}}\right)_{I_{out}=0} = \left(\frac{V_1}{I_1}\right)_{I_3=0} = \left(Z_{11} - \frac{(Z_{12} - Z_{14})^2}{2(Z_{11} - Z_{13} + Z'_{11} - Z'_{12})} - \frac{(Z_{12} + Z_{14})^2}{2(Z_{11} + Z_{13} + Z'_{11} + Z'_{12})}\right)$$

$$\tag{6.10}$$

$$Z_{12}^T = Z_{21}^T = \left(\frac{V_{in}}{I_{out}}\right)_{I_{in}=0} = \left(\frac{V_1}{I_3}\right)_{I_1=0} = \left(Z_{13} - \frac{(Z_{12}-Z_{14})^2}{2(Z_{11}-Z_{13}+Z_{11}'-Z_{12}')} - \frac{(Z_{12}+Z_{14})^2}{2(Z_{11}+Z_{13}+Z_{11}'+Z_{12}')}\right)$$

(6.11)

Using two-port network parameter conversion table [11], the scattering parameters can be given by

$$S_{11} = \frac{\left(Z_{11}^T\right)^2 - Z_0^2 - \left(Z_{21}^T\right)^2}{(Z_{11}^T + Z_0)^2 - \left(Z_{21}^T\right)^2}$$

(6.12)

$$S_{21} = \frac{2Z_{21}^T Z_0}{(Z_{11}^T + Z_0)^2 - \left(Z_{21}^T\right)^2}$$

(6.13)

where Z_0 is the reference impedance. In the following sections, the proposed filtering topology will be studied thoroughly in terms of TZs, 3dB- FBW and selectivity.

6.2.1 Transmission Zeros

From (6.13), the TZ conditions are obtained as:

$$\begin{cases} Z_{21}^T = 0 \\ \dfrac{1}{(Z_{11}^T + Z_0)^2 - \left(Z_{21}^T\right)^2} = 0 \end{cases}$$

(6.14)

Due to the complexity of obtaining algebraic solutions for TZs, we resort to ideal transmission line (TL) simulation using Advanced Design System (ADS). Signal interference is produced by the feedback coupled-line coupler which is open-circuited at the opposite ends. Assuming $k_m = k_f$ and impedance ratio ($R_z = Z_f/Z_m = 1$), electrical length ratio ($n = \theta_f/\theta_m$) can be varied to generate a variable number of TZs within the upper stopband as shown in Figure 6.5 where $\theta_m = \pi/2$ at 2.4 GHz.
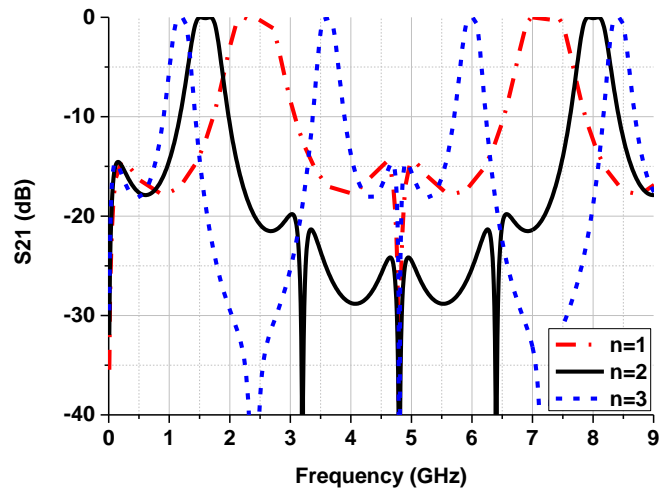
Figure 6.5. S_{21} simulation results for different electrical length ratio (n). ($Z_m = Z_f = 14\,\Omega, k_m = k_f = 0.178, Z_0 = 50\,\Omega$).

It can be seen that a higher rejection level with three TZs as well as wider upper stopband can be obtained when $n = 2$. It can also be observed that the 3-dB FBW is inversely related to n where it decreases from 36% to 24% when n is varied from 1 to 3. This can be easily understood by observing the number of transmission poles and the distance between them within the passband as shown in Figure 6.6. Also, return loss (RL) is improved within the passband as n is increased.
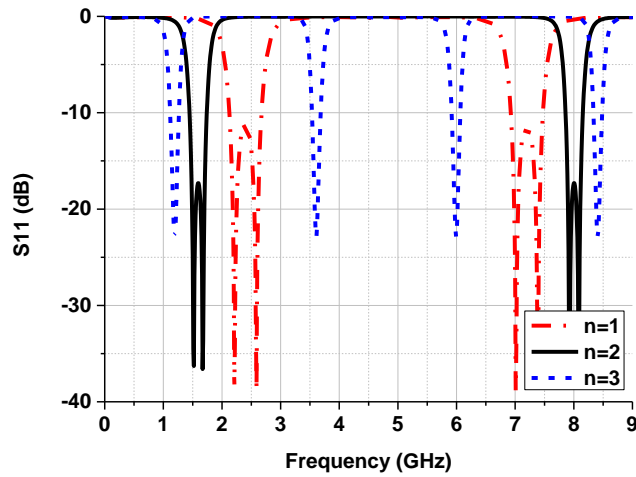
Figure 6.6. S_{11} simulation results for different electrical length ratio (n). ($Z_m = Z_f = 14\ \Omega, k_m = k_f = 0.178, Z_0 = 50\ \Omega$).

Furthermore, the harmonic responses can be controlled by n as seen in Figure 6.5. The second and fourth harmonics appear at around 3.6 GHz and 6 GHz, respectively for $n = 3$, whereas these two spurious responses have been suppressed for $n = 2$. This is very useful feature. It is interesting to notice that n is not restricted to integer values and can be a fraction. The structure was evaluated for different fractional values as seen in Figure 6.7, while keeping the same θ_m assumed for the $n = 2$ case.
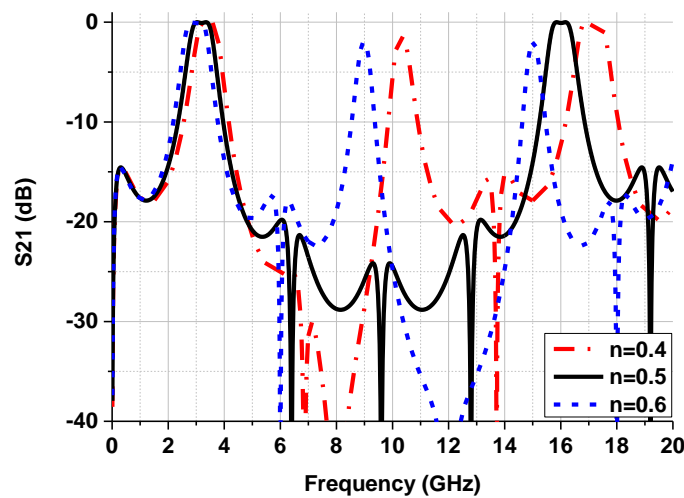
Figure 6.7. S_{21} simulation results for different fractional values of (n). ($Z_m = Z_f = 14\ \Omega, k_m = k_f = 0.178, Z_0 = 50\ \Omega$).

145

The simulation results show that the center frequency is shifted to 3.2 GHz when $n = 0.5$ and a wide upper stopband is achieved resembling the case with $n = 2$. Moreover, the center frequency is shifted from 3.3 GHz to 3.1 GHz and FBW is slightly increased from 27% to 30% as n is increased from 0.4 to 0.6. This is yet another useful feature for the proposed topology where center frequency and FBW can be controlled by the feedback circuit without the need of any modification of the main coupled-line coupler. As it can be seen from Figures 6.5, 6.6, and 6.7, the BPF based on signal interference feedback has some intriguing features worth analyzing further.

-Effects of coupling factor:

The effects of changing coupling factor values for both couplers having the same coupling factor are illustrated Figure 6.8, showing that tighter coupling broadens the FBW from 15% to 47% with $f_o = 1.6$ GHz but reduces the rejection level from 20 dB to 15 dB up to $4.5f_o$. IL is decreased as both coupling factors are increased from 0.1 to 0.2. However, when $k_f = k_m = 0.3$, IL is increased due to over-coupling.
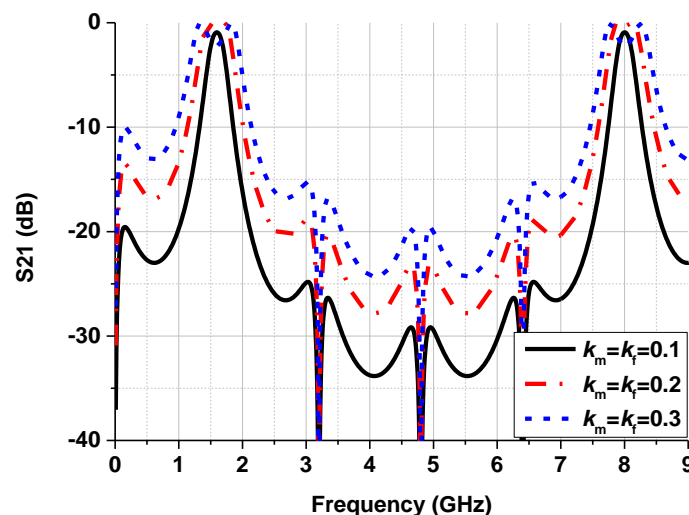
Figure 6.8. S_{21} simulation results for different coupling factors.$(n = 2, Z_m = Z_f = 14\ \Omega, Z_0 = 50\ \Omega)$.

Moreover, increasing k_f while keeping k_m constant will change the location of the first and third TZs with the second TZ unmoved as shown in Figure 6.9. In addition to n, k_f can also be used to suppress spurious responses. For instance, $k_f = 0.1$ can suppress both second and fourth spurious responses.
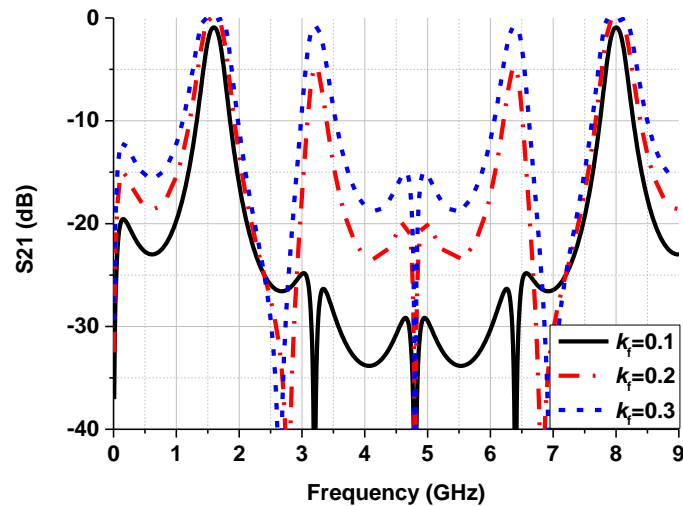
Figure 6.9. S_{21} simulation results for different k_f .($n = 2, k_m = 0.1, Z_m = Z_f = 14 \, \Omega, Z_0 = 50 \, \Omega$).

-Effects of impedance ratio:

The impedance ratio (R_z) is another factor that affects the filter's performance. Keeping k_f and k_m fixed while increasing R_z increases the IL within the passband and shift the centre frequency down from 1.67 GHz to 1.25 GHz but the stopband bandwidth is significantly reduced due to the appearance of undesired spurious passbands as shown in Figure 6.10. Moreover, it can be seen that the number of TZs increases to 5 for $R_z = 3$.
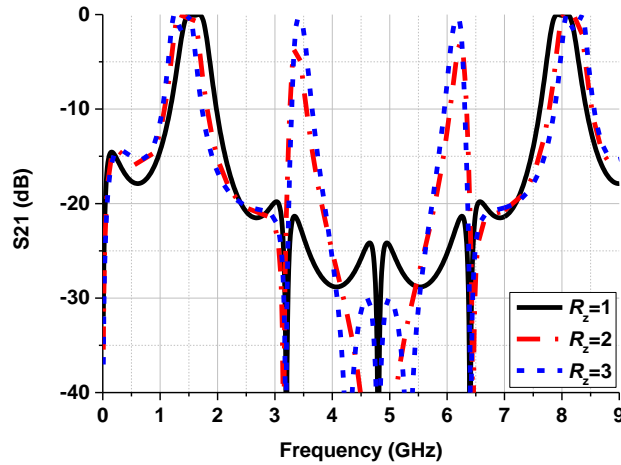
Figure 6.10. S_{21} simulation results for different impedance ratio.$(k_m = k_f = 0.178, Z_m = 14\ \Omega, Z_0 = 50\ \Omega\ )$.

6.2.2 3dB Fractional Bandwidth and Roll-off rate

There is always a trade-off between 3dB FBW and selectivity of a BPF. For a BPF based on signal interference feedback, its 3dB FBW can be designed by properly choosing n, k_m, k_f and R_Z, which can be proved very useful for relaxing fabrication tolerance and increase degree of freedom on filter design. For instance, coupling factors and characteristic impedances of the two coupled-line couplers depend on the odd and even mode impedance values as shown in (1) and (3). The filter 3dB FBW can be easily controlled by changing the coupling factors and the characteristic impedances concurrently while preserving the center frequency and IL as shown in Figure 6.11.
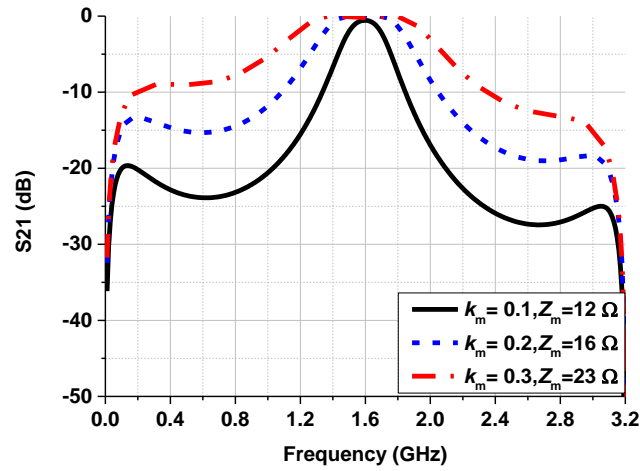
Figure 6.11. S_{21} simulation results for different coupling factors and characteristic impedances.$(n = 2, k_m = k_f, R_z = 1, Z_0 = 50\ \Omega)$.

It can be seen that the selectivity of the BPF is degraded as 3dB FBW is increased. Increasing n is another effective way of improving the roll-off rate of the BPF as illustrated in Figure 6.12. By increasing n, reducing θ_m at 2.4 GHz and keeping θ_f constant , the total electrical size of the BPF is kept constant while roll-off rate is significantly increased from 19 dB/GHz to 35 dB/GHz with minor roll-on rate reduction. Narrowband BPF design usually requires 3dB FBW of less than 10% and higher roll-up/down rates which can be easily provided by the proposed topology. In Figure 6.13, roll-up/down rate of more than 100 dB/GHz is obtained by increasing n to 10 while having $\theta_m = 16.3°$ at 2.4 GHz and maintaining low values for coupling factor and characteristic impedance for both couplers. The 3dB FBW for this case is 5% and more than 20 dB attenuation level is achieved within lower and upper stopband.
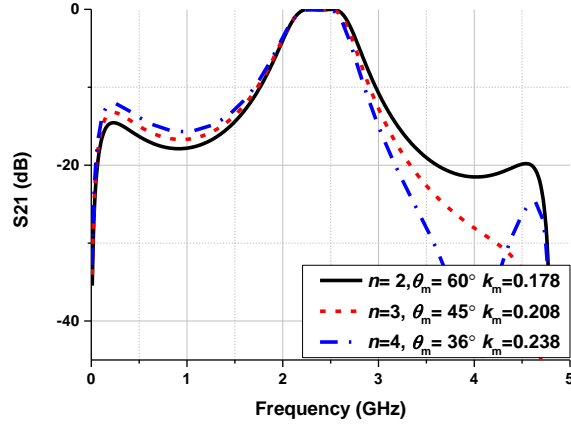
Figure 6.12 S_{21} simulation results for different n and θ_m .($k_m = k_f, Z_m = Z_f = 14\ \Omega$, $Z_0 = 50\ \Omega$).
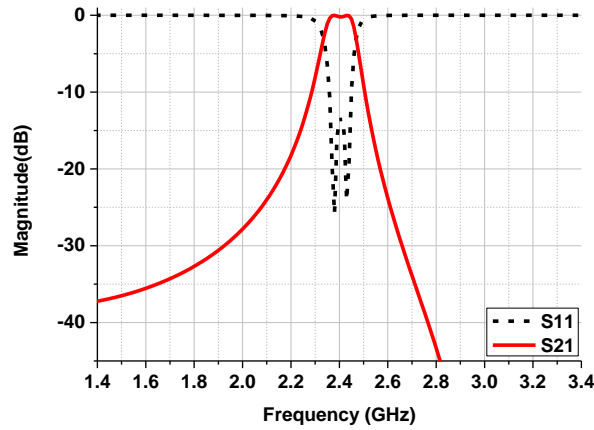
Figure 6.13 S_{21} and S_{11} simulation results for high selectivity narrowband BPF design.($n = 10, \theta_m =$

$16.3°,\ k_m = k_f = 0.11, Z_m = Z_f = 2.5\ \Omega$, $Z_0 = 50\ \Omega$).

6.2.3 Size reduction

The physical realization of the structure depicted in Figure 6.1 can be achieved by using planar

or multilayer technology. In this work, LTCC technology was chosen as proof of concept. The

BPF of very simple structure, shown in Figure 6.14, was designed and fabricated. The physical

length of the feedback coupler l_f was chosen being twice longer than main coupler l_m to

achieve wide stopband. Meandered line coupler was designed to reduce the size.
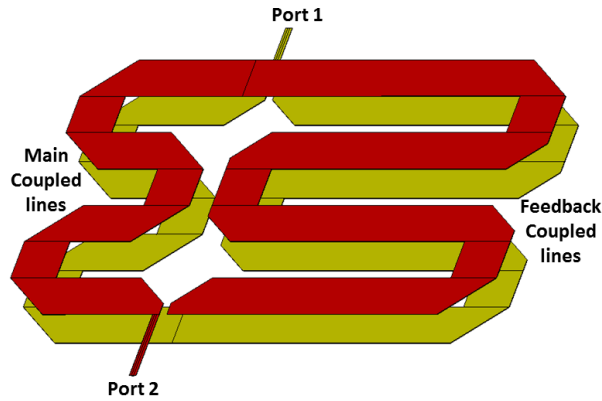
Figure 6.14 3D model of the proposed BPF structure.

6.2.4 Design Methodology

The main parameters that are involved in the design are n, R_z, k_f, and k_m. These parameters are

closely related and can affect each other. The following steps can be used as a design procedure

for the proposed BPF design:

- Determine the required electrical length for the main path coupled-line to satisfy the

  center frequency requirement.

- Using Figures 6.5 and 6.7 as a reference, select n to fulfill the required rejection level

  and stopband bandwidth needed.

- The parameters of both coupled-lines (k_m, k_f, Z_m, Z_f) can be varied to achieve desired

  FBW and roll-off rate as seen in Figure 6.11 and 6.12.

6.2.5 Design Example

As a proof of concept, a design example of the proposed BPF topology is presented in this

section to demonstrate the applicability of the theory discussed earlier. A BPF with center

frequency $f_c = 2.4$ GHz and FBW = 13% was designed using coupled-line BPF in the feedback.

Figure 6.5 shows that f_o is tuned to a different frequency when n is increased while fixing $\theta_m = 90°$ at 2.4 GHz. Hence, a different θ_m needs to be chosen to tune the BPF back to 2.4 GHz. The LTCC substrate used to design the BPF has a dielectric constant $\varepsilon_r = 5.9$ and loss tangent $\tan(\delta_D)= 0.001$. Considering $\theta_m = 59°$ at 2.4 GHz and $n = 2$, the physical lengths l_m and l_f were calculated to be 8 mm and 16 mm, respectively. The next step was to design the coupled-line parameters (k_m, k_f, Z_m, Z_f) to extend the upper stopband to 4.7 f_0 and maintain a -1 dB IL and -18 dB Return Loss (RL) within the passband. Using Figure 6.11 and 6.12 as a reference, it can be observed that the best stopband performance is achieved when $k_m = k_f$ and $R_z = 1$. Therefore, both pairs of coupled-lines were designed with $Z_f = Z_f = 14 \: \Omega$ and $k_m = k_f = 0.178$ to obtain desired performance. The initial design of the BPF using folded coupled strip-line required a physical size of 10.15×5.95 mm² and was reduced to 6.34×4.15 mm² with the use of meandered lines as seen in Figure 6.14.

The final design parameters were optimized using CST microwave studio and plotted in Figure 6.15. The upper, lower, front and rear sides of the outer surface conductors were patterned to form the soldering I/O pads as seen in Figure 6.16. The left and right sides of the outer surface conductors are solid. The soldering pads were interconnected with the feed lines on the inner conductor layers using tapered segments of strip lines to provide wideband coplanar waveguide (CPW) TL-to-strip line impedance transition. The structure used no other interconnections/ vias between layers. The thickness of inner and outer conductor pattern and LTCC dielectric layers was not less than 100 µm to ensure that standard LTCC process with screen print patterning could be used.
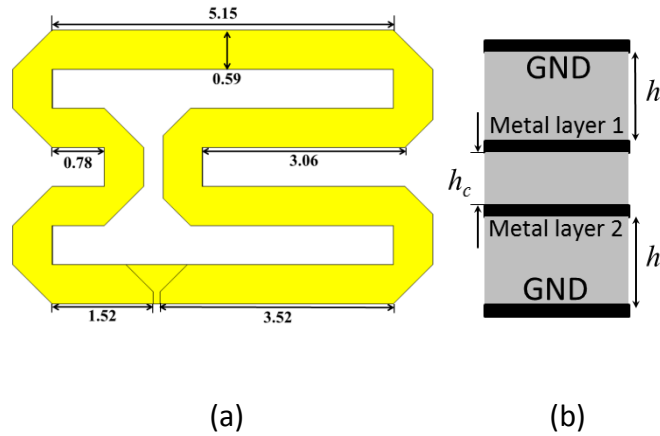
Figure 6.15 Design layout : (a) top view (dimensions in mm); (b) layer distribution (h_c = 0.3 mm, h =0.1 mm).
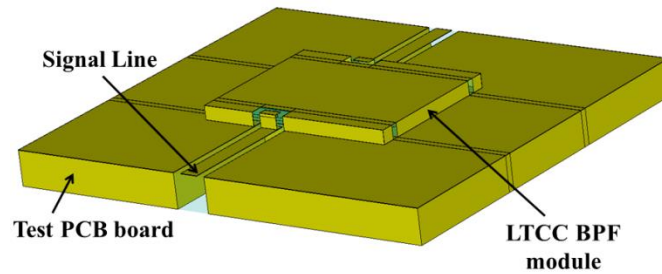
Figure 6.16 3D model of the proposed BPF with mounting PCB board.

To facilitate the measurement, the fabricated LTCC BPF was mounted on the PCB board using Rogers RO3006 substrate with relative dielectric constant of 6.15, thickness of 1.28 mm, and loss tangent $\tan(\delta_D)$= 0.002. Figure 6.17 shows a photograph of the fabricated BPF. The measured results were plotted against EM simulation results in Figure 6.18. The measured results show that the BPF has low IL of -1.3 dB at f_0= 2.4 GHz and the return loss is greater than 18 dB. It exhibits a 3 dB FBW of 13% and a rejection level of more than -15 dB from 3.3 to 11.4 GHz (4.7 f_0) due to the presence of three TZs at 4.6, 7.5, and 9.7 GHz. Good correlation between simulation and measurement results are obtained and the slight difference between them is mainly attributed to fabrication tolerances.
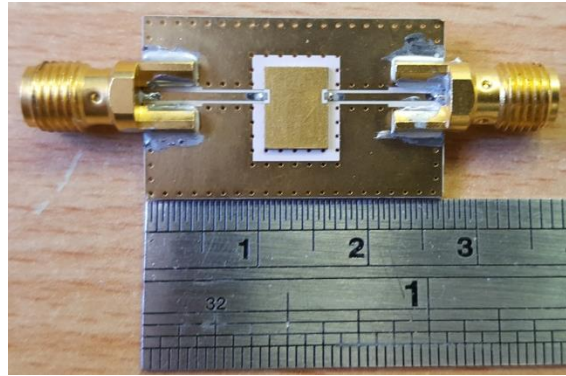
Figure 6.17 Photo of the fabricated wide-stopband LTCC BPF.
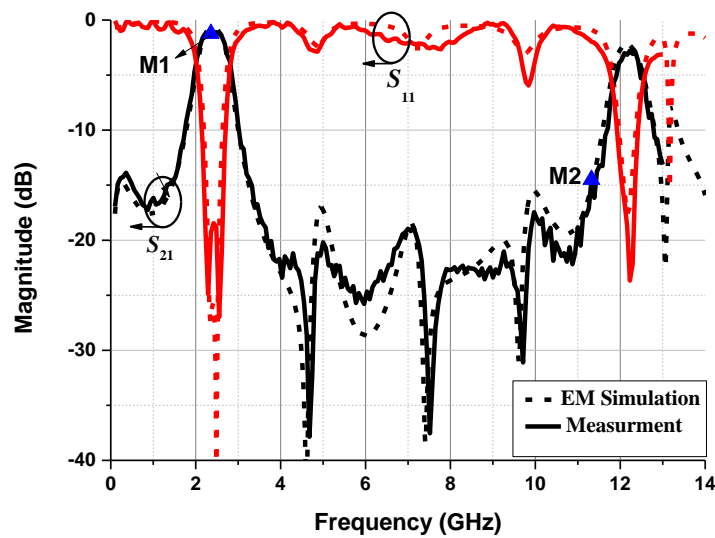
Figure 6.18 Simulated and measured results of the proposed LTCC BPF design (M1= 1.3 dB at 2.4 GHz, M2= 15 dB at 11.3 GHz).

The proposed design is compared to other reported LTCC BPFs in the literature in Table I, showing that the BPF based on feedback concept is capable of providing superior performance in terms of IL, FBW, upper stopband bandwidth with comparable electrical size. Although wider stopband bandwidth is achieved in [118], the proposed filtering structure is easier to design and has lower insertion loss.

Table 6.1 Comparsion of the proposed BPF with recent reported LTCC BPFs.

Ref.	f_o (GHz)	IL (dB)	FBW %	Stopband (GHz)	Physical size (mm^3)	Electrical size (λg^3 at f_o)
[118]	2.4	2.59	11.5	5.2 f_o (25 dB)	3.5×2.8×1.7	0.00007
[129]	2.4	2.4	7	1.63 f_o (38 dB)	6.0×5.0×1.6	0.00037
[130]	2.45	2.5	8	3.26 f_o (35 dB)	0.76×0.75×0.67	0.00009
[131]	2.45	2.5	10.8	4 f_o (26 dB)	2.48×2.02×0.6	0.00003
[132]	2.4	2.4	12.5	3.1 f_o (30 dB)	2.63×2.61×0.5	0.00004
[133]	10	2.46	1.95	1.38 f_o (40 dB)	23×10×1	0.12217
[134]	2.6	2.47	10.2	4.15 f_o (28 dB)	3×2.8×2	0.00006
[135]	2.5	1.5	10	2.2 f_o (30 dB)	5.4×3.9×0.765	0.00011
This work	2.4	1.3	13	4.7 f_o (15 dB)	6.34×4.15×0.52	0.00010

λ_g denote guided wavelength at f_o

6.2.6 Improved BPF design using stepped impedance coupled-line

To improve the performance of the proposed BPF design mentioned in the previous section, the simple topology used before can be modified by cascading two couplers in the feedback instead of a single coupler. These two couplers provide extra degree of freedom that can be utilized to broaden the upper stopband bandwidth or realize a high selectivity BPF. The modified structure is presented in Figure 6.19 using ideal TL components. Since ideal transmission line model will be used to enhance the performance of the fabricated BPF, the arbitrary variation of the associated design parameters may lead to impractical solutions from a fabrication standpoint. Therefore, in order to restrict the analysis to feasible parameter values, their variation have been limited to the following ranges:

- Characteristic impedance (Z_m, Z_{f1}, Z_{f2}): 10 to 150 Ω.

- Coupling factor (k_m, k_{f1}, k_{f2}): 0.1 to 0.9.

- Electrical length (θ_m, θ_{f1}, θ_{f2}): 10 to 360°.
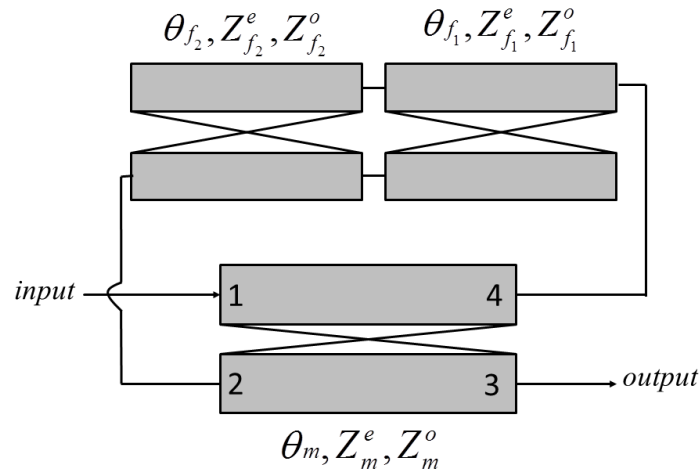
Figure 6.19 Modified structure of the proposed BPF with two cascaded couplers in the feedback.

Nevertheless, the range of parameter values that can be practically realised largely depend of the particular implementation technology employed as well as on the tolerances of the associated fabrication processes. The first goal from studying this structure is to extend the upper stopband of the BPF mentioned in the previous section to at least to $7f_o$ while keeping similar passband performance (f_o = 2.4 GHz, IL = -1 dB, RL = -15 dB, 3dB FBW = 10%). The topology has been optimised with the parameters limitations that have been described earlier, leading to the performance shown in Figure 6.20. The optimised parameters are : (θ_m = 104.15, Z_m = 14.88, k_m = 0.14, θ_{f1} = 20.04, Z_{f1} = 16.16, k_{f1} = 0.11, θ_{f2} = 42.86, Z_{f2} = 10, k_{f2} = 0.22). It can be seen here that the cascaded couplers resemble the case of stepped impedance coupled-lines (SICLs) which is well known approach for harmonic suppression[136] where the resonant frequencies of SICLs can be tuned by modifying the SICL parameters such as impedance ratio. Due to the combined effect of SICL and feedback signal interference, a spurious passband cantered at about 18.5 GHz appears in the response, leaving an upper stopband between 3.44 and 17.27 GHz (7.2 f_o), and a lower stopband from 1.45 GHz down to DC. The rejection level is greater than 15 dB within both stopbands, except for a few

very narrow regions where it reaches approximately 14.75 dB. The IL is lower than 0.6 dB and the return loss is greater than 10 dB with a centre frequency of 2.47 GHz and FBW of 30%.
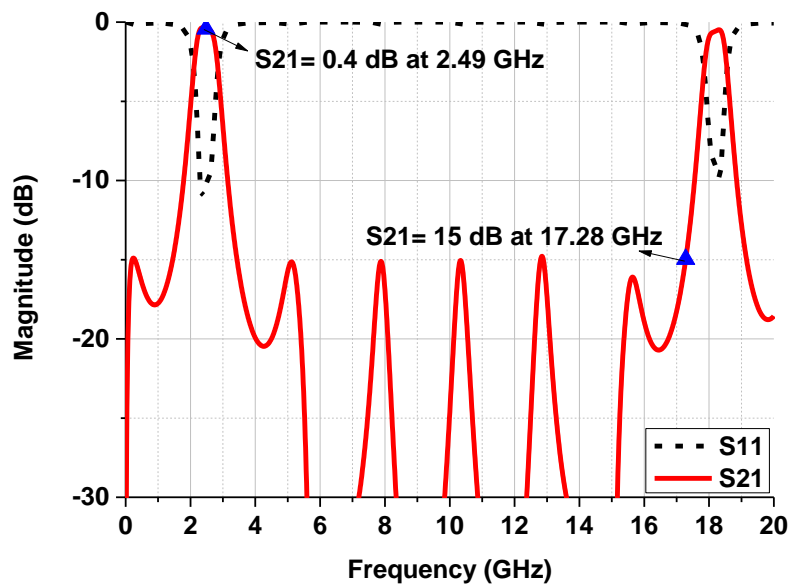
Figure 6.20 Ideal TL model simulation results for the improved BPF design.

It should be mentioned here that the passband is clearly wider than the initial specification required for this design. Due to the limited number of design parameters in the modified structure, the different features in the frequency response are interconnected in such a way that they cannot be separately controlled such as 3dB FBW. Thus, attempting to obtain a narrower passband that is more suitable for narrow band BPF, would in turn lead to degradation of stopband performance and realizing narrower upper stopband bandwidth. Analogously, it has not been possible to further improve the design in terms of either rejection level or upper stopband bandwidth, which indicates that the current design is close to the optimum values.

The selectivity of the proposed filtering structure mentioned in the previous section can be improved by increasing electrical length ratio *n*. The modified structure presented in this section can be also utilized to design high selectivity BPF with a roll-on/off rate of least 200 dB/GHz. The structure has been progressively optimised to obtain the following specifications: (f_o = 2.4 GHz, IL = -1 dB, RL = -15 dB, 3dB FBW = 10%) while the upper stopband bandwidth

requirement was relaxed to $2f_o$ with a rejection level of 15 dB. The frequency responses for three different solutions are presented in Figure 6.21 to show how the selectivity for the modified structure can be enhanced. The optimised parameters for each design are specified in Table 6.2. It can be concluded from these ideal TL model simulation results that design III has the highest selectivity with a roll-on/off rate of 345 and 200 dB/GHz, respectively. This impressive selectivity performance achieved at the cost of producing several narrow peaks over 15 dB throughout the stopbands. The peaks are relatively smooth in the design II, whereas those in design III exhibit very harsh oscillations and very sensitive to slight variations in the parameters.
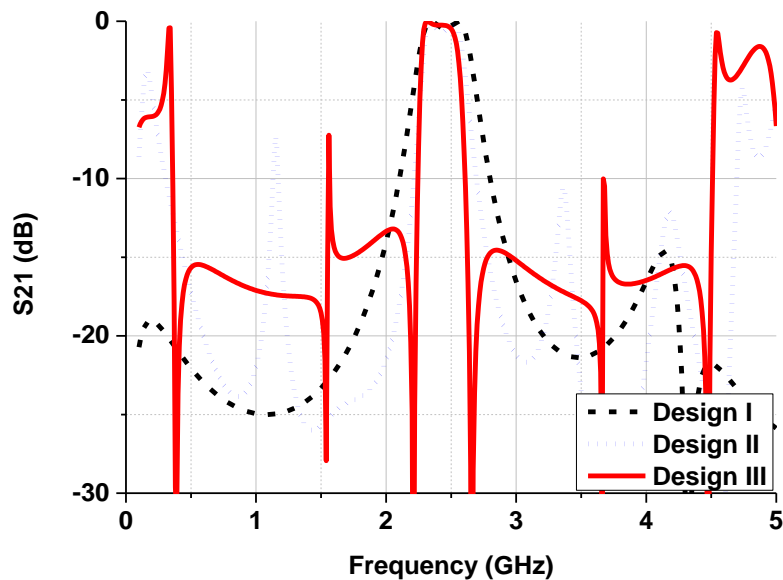
Figure 6.21 Ideal TL model simulation results for the high selectivity cases using stepped impedance coupled in the feedback.

Table 6.2 Design parameters for the three solutions for high selectivity BPF.

Design parameters	Design I	Design II	Design II
θ_m	116.274°	110.64°	174.71°
θ_{f1}	55.712°	171.23°	184.47°
θ_{f2}	18.931°	203.48°	20.83°
Z_m	10.1 Ω	115.61 Ω	10 Ω
Z_{f1}	22.38 Ω	26.85 Ω	135.41 Ω
Z_{f2}	22.48 Ω	150 Ω	32.58 Ω
k_m	0.11	0.17	0.36
k_{f1}	0.1	0.1	0.86
k_{f2}	0.1	0.89	0.9

From Table 6.2, it can be seen that electrical length for the two couplers used in the feedback is significantly higher than the electrical length for the coupler used in the main signal path in design III. This was already observed in the previous section where increasing electrical length ratio *n* enabled the improvement of selectivity. Here, another requirement is needed to increase roll-up/down rate which is the high coupling factor value needed within the feedback circuit. This requirement restricts the fabrication of this design to multi-layers technology such as LTCC and Liquid-crystal polymers (LCP) technologies. Both of the designs presented in this section will be considered for the future work of this research project.

6.3 High Selectivity Microstrip Coupled-line BPF Using Feedback CRLH TL unit cell

In this section, a simple approach to design high selectivity microstrip BPF is discussed. Based on the signal interference concept, the selectivity of a BPF using CRLH TL unit cell can be significantly improved. Thus, by employing a single coupled-line section in the direct pass and CRLH TL unit cell in the feedback, a high selectivity BPF with multiple TZs within the upper stopband has been realized. The measured results show that the proposed BPF has a center frequency of 2.4 GHz with roll-up rate of 400 dB/GHz and roll-down rate of 330 dB/GHz.

The configuration for the proposed high selectivity BPF design is shown in Figure 6.22. It consists of coupled-line coupler and CRLH TL in the feedback circuit. Thus, the BPF has two electrical paths: a direct signal propagation path associated with the feedback CRLH TL and another path associated with the single stage coupled-line coupler.
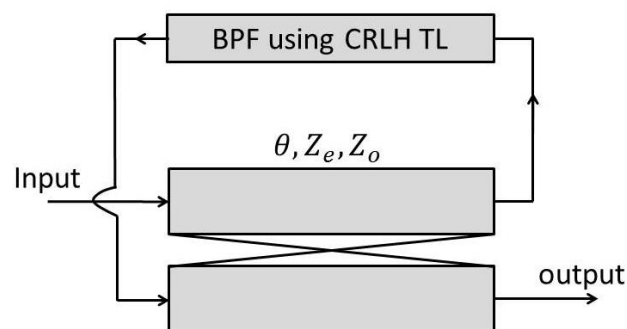
Figure 6.22 Proposed high selectivity BPF design based on signal interference feedback concept.

The BPF used in the feedback is constructed using single unit cell of CRLH TL. The left-handed property of the CRLH TL is represented by the series capacitance (C_L) and shunt

inductance (L_L) provided by the two interdigital capacitors and grounded stub as shown in Figure 6.23. Moreover, two open stubs are used for matching purpose.
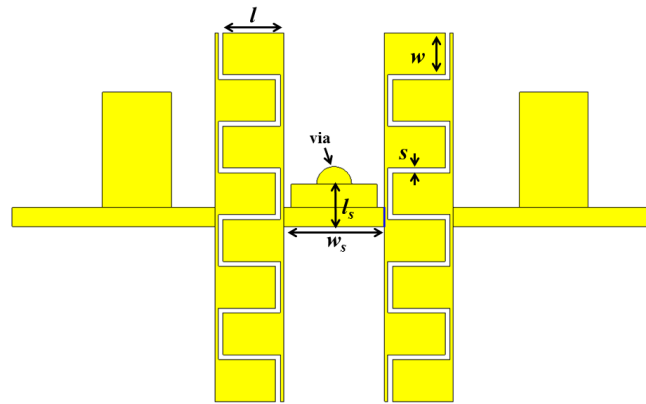
Figure 6.23 Layout of CRLH TL unit cell used in the feedback circuit.

Desired effective inductance and capacitance is obtained by optimising the geometric parameters for the interdigital capacitors and grounded stub. The geometry of such structure is described by the finger width (w), finger length (l), spacing between two fingers (s), and number of fingers (n). The capacitance of the interdigital capacitor and inductance of grounded stub can be determined using the approximate formulas (3.4) and (3.5). These formulas can be used to obtain the needed effective capacitance (C_L) and inductance (L_R) for the interdigital capacitor as shown in the equivalent circuit model in Figure 6.24. C_R and L_L account for the grounded stub. This equivalent circuit is optimised using Advanced Design System (ADS) software to design a BPF with centre frequency of 2.4 GHz, 3-dB FBW of 8% and roll-up/down rate of 100 dB/GHz assuming a terminal impedance of 50 ohm. Simulation results confirmed that required values for C_L and L_R are 1.2785 pF and 0.81 nH, respectively. Similarly, C_R and L_L have the values of 6.85 pF and 0.117 nH. The open stubs are represented by L_S and C_S which have the values of 0.373 nH and 1.246 pF, respectively. These values can be used to obtain the physical dimensions for the interdigital capacitor and grounded stub. The initial dimension for the interdigital capacitor are determined as $w = 1.79$ mm, $l = 2.6$ mm, $s = 0.2$ mm, $n = 8$,

whereas the dimensions for the grounded stub are obtained as $w_s = 4.29$ mm, $l_s = 1.82$ mm. These initial physical values were used to construct the CRLH TL unit cell using Rogers RO3006 substrate with a thickness of 0.64 mm, dielectric constant $\varepsilon r = 6.15$, copper cladding $= 35$ μm and 3D electromagnetic full-wave simulation using CST Microwave studio refined these dimensions. The simulation results from ADS were compared to the simulation results obtained by CST in Figure 6.24. It can be noted that good correlation is obtained between equivalent circuit and 3D model simulation results.
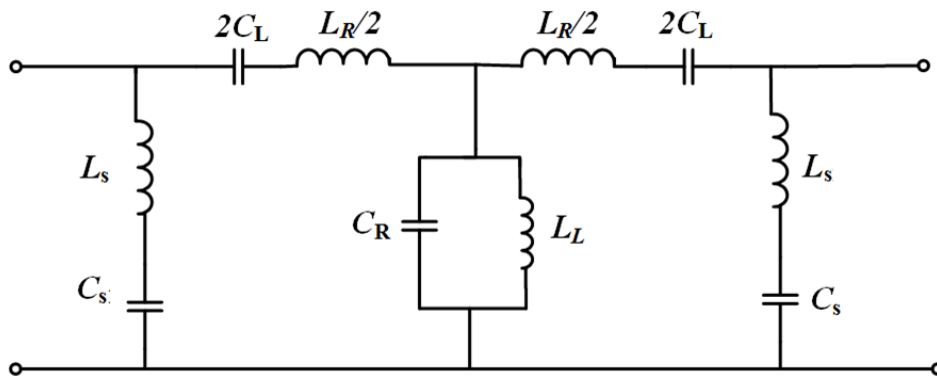
Figure 6.24 Equivalent circuit model of the CRLH unit cell used in the feedback circuit including open stubs.
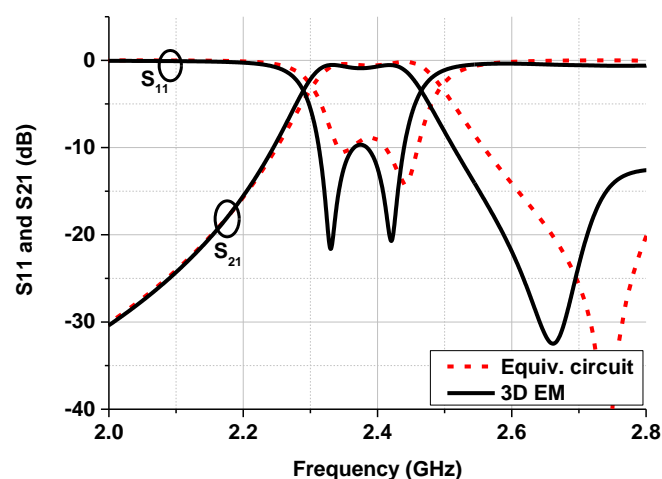
Figure 6.25 Comparison of simulated S-parameter for the CRLH TL unit cell including open stub using equivalent circuit mode and 3D model.

162

The CRLH TL unit cell was then connected to the single stage coupled-line coupler to form the whole BPF design as shown in Figure 6.26. The final simulation results show that the BPF has a 3dB FBW of 6% at the center frequency 2.4 GHz and roll-up/down rates of 400 dB/GHz and 300 dB/GHz respectively as depicted in Figure 6.27. Due to the inherent high pass properties of the CRLH TL, the roll-up rate is much higher than the roll-down rate. Moreover, four TZs are generated by the feedback signal interference within the upper stopband at 2.54, 2.66, 2.8, and 2.91 GHz.
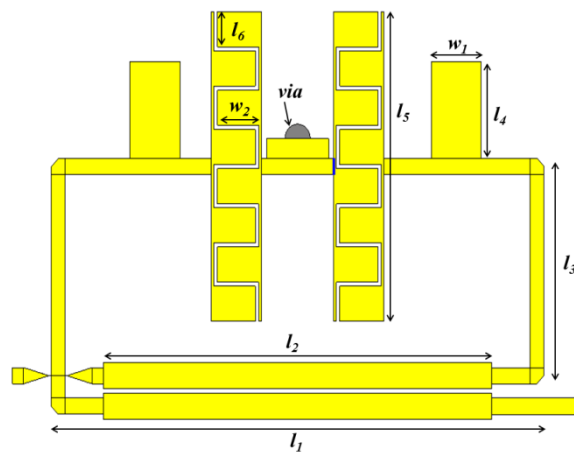
Figure 6.26 Layout of proposed BPF using CRLH TL unit cell in the feedback circuit.
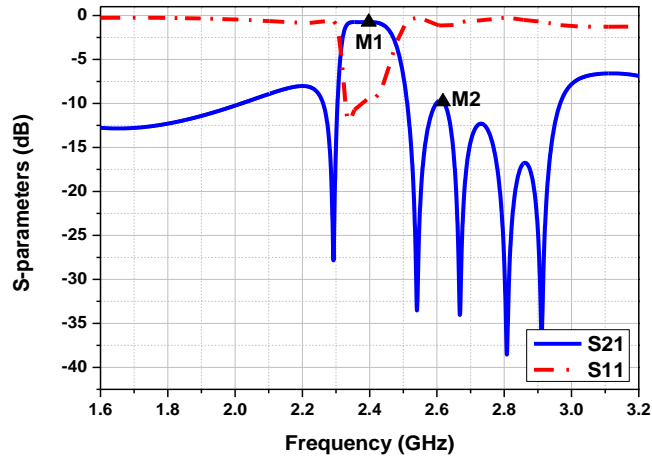
Figure 6.27 Simulated S_{11} and S_{21} for the proposed BPF using feedback CRLH TL unit cell (M1= 0.75 dB at 2.4 GHz, M2= 9.75 dB at 2.61 GHz).

The existence of left/right handed region within the passband can be easily obtained using the S-parameter retrieval method [103] mentioned in Chapter 5. The results show that the proposed BPF exhibit a left-handed region from 2.31 to 2.4 GHz and a right-handed region from 2.4 to 2.48 GHz as depicted in Figure 6.28.
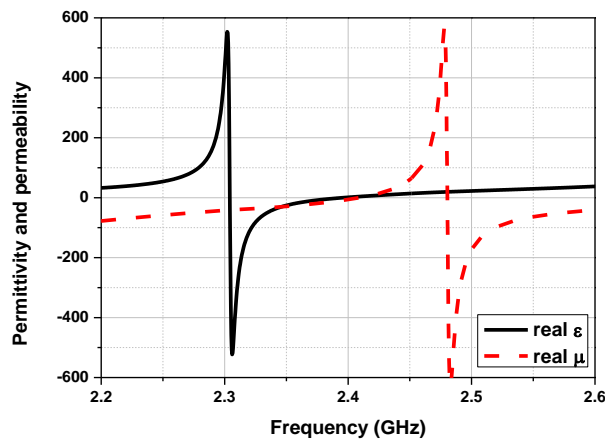
Figure 6.28 Real part of the extracted ε and μ for the proposed BPF utilizing CRLH TL unit cell in the feedback.

Sharp selectivity obtained using signal interference feedback concept is constrained by the coupling factor within the coupled-line coupler. To show the effect of coupling factor on the location and proximity of the TZs to the passband, the BPF was simulated with different

164

coupled-line spacing (*g*). The simulation results in Figure 6.29 and Figure 6.30 show that wider the spacing (weaker the coupling) results in the TZs being located further apart from the passband. Thus, selectivity and return loss are slightly degrading as coupling factor is increased while rejection level within the lower stopband is improved.
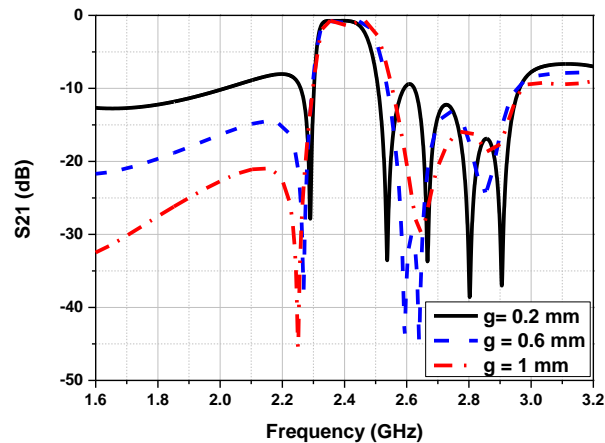
Figure 6.29 Simulated S21 for different coupled-line spacing within the main signal path.
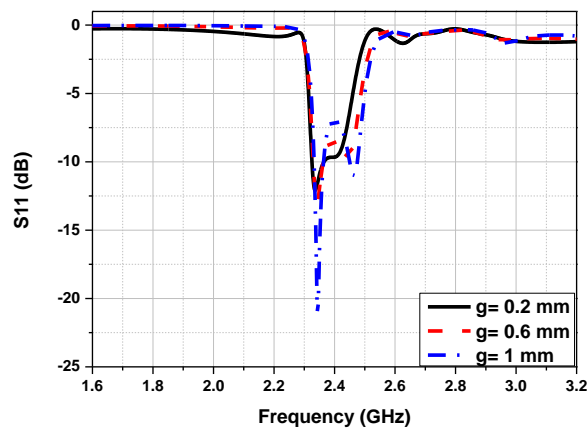
Figure 6.30 Simulated S11 for different coupled-line spacing within the main signal path.

The proposed BPF was fabricated using Rogers RO3006 substrate with relative dielectric constant ε_r= 6.15, thickness H=0.64 mm, loss tangent $\tan(\delta_D)$= 0.002. The optimized dimensions for the BPF are (mm): l_1= 29.17, l_2= 22.93, l_3= 11.13, l_4= 4.92, l_5= 15.77, l_6= 2.45, w_1= 2.94, w_2=1.79, via radius= 0.75 and finger spacing = 0.2. Figure 6.31 shows a photograph of the fabricated BPF. The simulated and measured power transmission and

reflection response of the proposed BPF are compared in Figure 6.32. The measured results show that roll-up/down rate of more than 300 dB/GHz can be obtained with an IL less than 2 dB at a center frequency of 2.4 GHz. The discrepancies between simulation and measurement results are attributed to the fabrication tolerance and the use of wire crossover to connect the input to the coupled-line coupler. The unwanted spurious near the passband can be suppressed by using stepped impedance coupled line in the main signal path. Another approach is to cascade bandstop filter to have a better rejection profile within the upper stopband. In the future work of this research, the use of proper crossover and spurious elimination will be addressed to achieve high selectivity and good stopband performance.
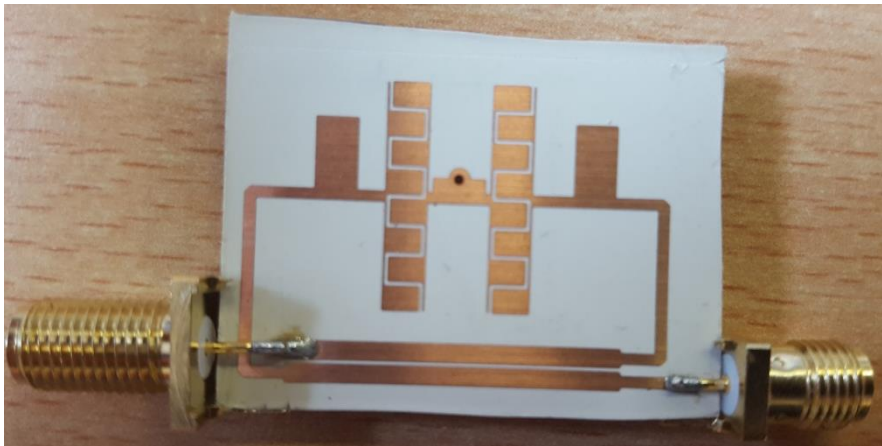
Figure 6.31 Photo of the fabricated BPF using feedback CRLH TL unit cell.
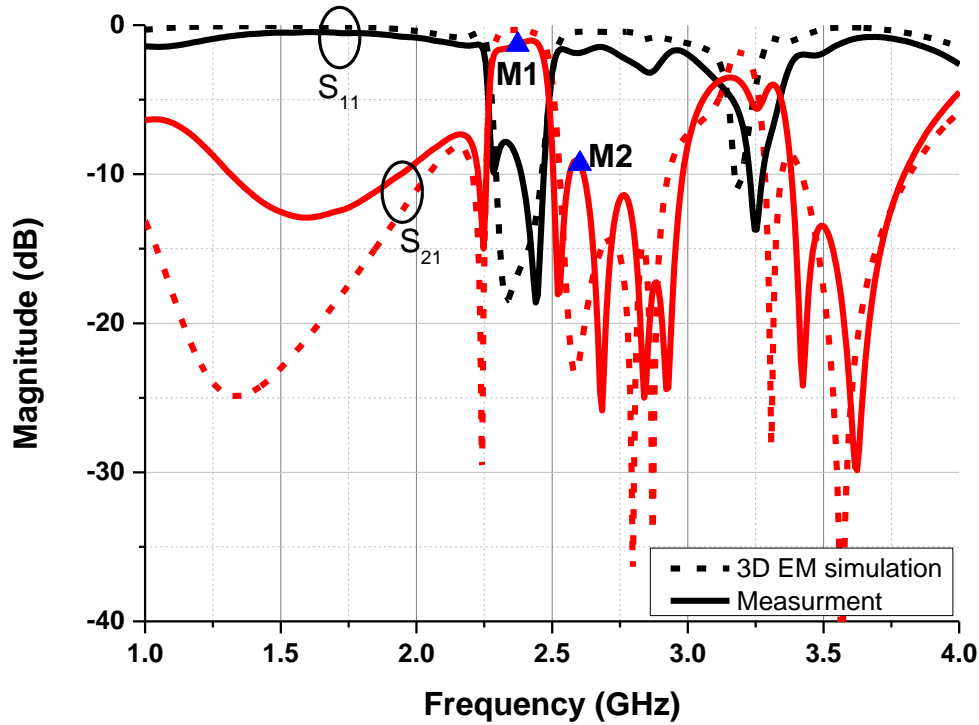
Figure 6.32 Comparison of simulated and measured S-paramters of the fabricated BPF (M1= 1.24 dB at 2.38 GHz, M2= 9.3 dB at 2.6 GHz).

6.4 Chapter summary

In this chapter, feedback signal interference concept is presented and explored to design high performance BPFs. In section 6.1, wide-stopband BPF with good selectivity is designed using a simple structure that contains only two couplers. The first coupler is used in the main signal path and the second coupler which is open circuited at the opposite ends is connected in the feedback circuit. The intriguing features that this new structure holds are discussed and illustrated using ideal TL simulation. One of the interesting cases is the ability to supress the harmonics with a very good rejection level. The measured results show that the fabricated BPF has an IL of -1.3 dB at a centre frequency of 2.4 GHz. Moreover, it has a rejection level of -15 dB up to $4.7f_o$ and roll-up/down rate of more than 20 dB/GHz.

The second design is presented in section 6.3 where high selectivity microstrip BPF is designed using coupled-line coupler in the main signal path and CRLH TL unit cell in the feedback. CRLH TL unit cell can be considered as a filtering structure and the selectivity of such a structure can be only improved by using extra unit cells which enlarge the circuit size and might introduce extra insertion loss. Here, an easy alternative method is presented where the selectivity can be improved by using a simple coupled coupler. It was shown through simulation that significant improvement in selectivity can be achieved with minor degradation within the passband performance.

Chapter 7: Conclusion and Future work

7.1 Conclusion

The first objective of this research was to explore the potential of metamaterial in designing compact BPF with enhanced performance. More specifically, it was explored to design ultra-wideband BPF with high selectivity and compact size using single CRLH TL unit cell. The proposed UWB BPF was designed and characterized using available equations in the literature. The measured results for the proposed UWB BPF show that more than 100% 3dB FBW can be achieved at a centre frequency of 6.85 GHz with an IL of -1 dB. Good selectivity is achieved and group delay variation within the passband was less than 0.44 ns.

Designing super compact dual-band BPF was the second objective of this research. It was realized using two slotted open stubs and single shorted stub that enable filter designer to engineer the stopbands to design a dual-band BPF with very small electrical size. The proposed slotted open stub has the advantages of relatively low IL, compact size, and the ability to control resonant frequencies which usually associated with multi-mode resonator. Furthermore, inner open stub that is located within the slotted open stub was examined and studied to enhance the performance of the designed dual-band BPF. Simulation results show that it can be utilized to control the second passband bandwidth, improve the roll-off rate at the upper edge of the second passband, and obtain wider upper stopband without increasing the circuit size. The final design was optimised using CST microwave studio and then fabricated to verify the proposed approach. Measurement results show that 117% and 36% 3dB FBW can be obtained for the first and second passband which are centred at 1/6.65 GHz. IL of 0.3/1 dB within the two passbands is achieved with an isolation between the two passbands of more than 20 dB from

2.0 to 4.9 GHz. The proposed structure exhibit high selectivity and an attenuation level of more than 20 dB from 8.5 to 12 GHz with super compact electrical size $\lambda g^2 = 0.004$.

Examining spectrum based quality factor for BPF based on CRLH TL to design low phase noise oscillator was the third objective of this research. Spectrum based quality factor was studied thoroughly and investigated to minimise phase noise in oscillator design. Simulation results show that high complex factor can be achieved within the LH region due to the slow wave propagation observed in CRLH TL based BPF. This intriguing feature enables the reduction of phase noise in oscillator design. The proposed filter based oscillator was designed and simulated at both group delay peak and spectrum based quality factor peak frequencies. Simulation results show significant improvement in phase noise performance is attained. The proposed oscillator design was fabricated to validate the design approach. The measured results confirmed that the fabricated oscillator has better performance when compared to the latest reported planar BPF based oscillator. The proposed design has measured phase noise of -126.7 dBc/Hz at an offset frequency of 100 KHz away from 2.05 GHz, an FoM of -207.2 dBc/Hz, while the oscillator core's total power consumption is 6.1 mW from a 2.135V DC supply.

The last objective of this research was to propose a new filtering topology that can be used to design high performance BPF with high selectivity and wide upper stopband. The new filtering structure is based on feedback signal interference which was utilized to design two BPF designs. The first design consisted of two coupled-line couplers where the first coupler was positioned in the main signal path and another coupler open circuited at the opposite ends is utilized in the feedback circuit. This structure was thoroughly studied using ideal TL simulation in ADS and simulation results show that it can be used to design BPF with good selectivity and wide upper stopband. The first design was fabricated using LTCC technology and the measurement results show that -15 dB rejection level can be achieved up to $4.7f_o$ with an IL of -1.3 dB at $f_o = 2.4$ GHz. The fabricated LTCC BPF shows superior performance and comparable

electrical size when compared to the latest reported wide-stopband LTCC BPF. The second BPF structure consists of coupled-line coupler in the main signal path and single CRLH TL unit cell in the feedback. The filtering performance of CRLH TL based BPF can only be improved by increasing number of unit cell at the expense of increasing the circuit size. This drawback can be easily tackled using the proposed BPF design. By utilizing the feedback signal interference concept, high selectivity microstrip BPF can be realized using a single coupler and CRLH TL unit cell in the feedback. The measured results show that high selectivity can be achieved with multiple TZs within the upper stopband and low IL.

7.2 Future work

The results of this research work confirmed the promising future of metamaterials and their applications to design compact high performance passive and active RF/microwave components. Moreover, feedback signal interference concept presented in this thesis proved to be an easy alternative method to design passive BPF with superior performance. The extension of the work presented in this thesis can be done on the following areas:

- It would be interesting to further study the UWB BPF design based on single CRLH TL unit cell presented in this thesis and suggest a new approach to include single or multi notched band(s) to minimize interference between UWB radio system and other wireless communication systems.

- Developing a synthesis method for the super compact dual-band BPF presented in chapter 4 is one of the interesting research topics that can enable filter designer to realize multi-band BPF at other frequency bands with compact size.

- The measurement results for the low phase noise oscillator presented in chapter 5 show an impressive performance and it is worth investigating the possibility of designing low phase noise voltage controlled oscillator using CRLH TL based BPF.

- Feedback signal interference concept presented in this thesis can be utilized to design different kinds of passive BPF such as multi-band BPF, tunable BPF. The wide-stopband BPF design mentioned in chapter 6 can be easily improved using stepped impedance coupled-line instead of uniform coupled-line as mentioned in section 6.2.6. The simulation result show that a rejection level of -15 dB up to $7f_c$ with good passband performance. The size of this BPF design can be reduced using meandered lines and fabricated to validate the simulation results.

List of Publications

(1)   A. Alburaikan, M. Aqeeli, X. Huang, and Z. Hu, "Miniaturized ultra-wideband bandpass filter based on CRLH-TL unit cell," in *44th Europ. Microw.Conf. (EuMC),* Rome, 2014, pp. 540-543.

(2)   A. Alburaikan, M. Aqeeli, X. Huang, and Z. Hu, "Miniaturized via-less ultra-wideband bandpass filter based on CRLH-TL unit cell," in *IEEE Radio and Wirel. Symp. (RWS)*, San Diego, 2015, pp. 126-128.

(3)   A. Alburaikan, M. Aqeeli, X. Huang, and Z. Hu, "Low phase noise free-running oscillator based on high selectivity bandpass filter using composite right/left-handed transmission line," *IEEE Microw. Wirel. Compon. Lett.*, vol. 26, no. 4, pp. 273-275, Apr. 2016.

(4)   M. Aqeeli, A. Alburaikan, C. Muvianto, X. Huang, and Z. Hu, "An ultra-wideband and gain linearized CMOS VCO with minor phase noise variation," in *Asia-Pacific Microw. Conf. (APMC),* Sendai, 2014, pp. 965-967.

(5)   M. Aqeeli, T. Leng, X. Huang, J. C. Chen, K. H. Chang, A. Alburaikan, and Z. Hu, "Electromagnetic interference shielding based on highly flexible and conductive graphene laminate," *Electr. Lett.*, vol. 51, no. 17, pp. 1350-1352, Aug. 2015.

(6)   M. Aqeeli, A. Alburaikan, X. Huang, and Z. Hu, "Low-phase noise variation VCO implementing resistorless digitally controlled varactor," in *Int. Conf. IC Des. & Tech. (ICICDT)*, Leuven, 2015, pp. 1-4.

(7)   M. Aqeeli, A. Alburaikan, X. Huang, and Z. Hu, "Wide tuning range voltage controlled oscillator (VCO) with minimized phase noise variation in nanoscale CMOS technology," in *IEEE 15th Int. Conf. Nanotech. (IEEE-NANO)*, Rome, 2015, pp. 51-54.

(8)   X. Huang, X. Zhang, Z. Hu, M. Aqeeli, and A. Alburaikan, "Design of broadband and tunable terahertz absorbers based on graphene metasurface: equivalent circuit model approach," *IET Microw., Antennas & Propag.*, vol. 9, no. 4, pp. 307-312, Mar. 2015.

(9)   M. Aqeeli, Z. Hu, X. Huang, A. Alburaikan, and C. Muvianto, "Low-power and wideband LC-VCO for WiMAX in CMOS technology," in *UKSim-AMSS 16th Int. Conf. Comp. Model. Simul. (UKSim),* Cambridge, 2014, pp. 553-557.

(10)   A. Alburaikan, M. Aqeeli, and Z. Hu, "Miniaturized dual-wideband bandpass filter using coupled slotted open stubs," in *IEEE MTT-S Int. Microw. Symp. (IMS)*, San Francisco, 2016, to be published.

(11)   A. Alburaikan, M. Aqeeli, X. Huang, and Z. Hu, "Coupled-line bandpass filter based on signal interference feedback," *IEEE Transac. Microw. Theor. Tech.*, **Submitted**.

(12)   A. Alburaikan, M. Aqeeli, G.N. Jawad, A. Biswas, and Z. Hu, "High selectivity microstrip bandpass filter using feedback CRLH-TL unit cell," in *2016 Asia-Pacific Microw. Conf. (APMC)*, Delhi, 2016, **Submitted**.

(13)   A. Alburaikan, M. Aqeeli, X. Huang, and Z. Hu, "Metamaterial based bandpass filter with high selectivity using feedback signal interference," *IET Microw., Antennas Propag.*, **Submitted**.

References

[1] C. Caloz, *Electromagnetic metamaterials : transmission line theory and microwave applications : the engineering approach / Christophe Caloz, Tatsuo Itoh*. Hoboken, N.J.: Hoboken, N.J. : Wiley-Interscience, 2006.

[2] G. V. Eleftheriades and K. G. Balmain, *Negative-Refraction Metamaterials: Fundamental Principles and Applications*. Wiley, 2005.

[3] G. V. Viktor, "The electrodynamics of substances with simultaneously negative values of and," vol. 10, ed, 1968, pp. 509-514.

[4] D. R. Smith, W. J. Padilla, D. C. Vier, S. C. Nemat-Nasser, and S. Schultz, "Composite Medium with Simultaneously Negative Permeability and Permittivity," *Physical Review Letters,* vol. 84, no. 18, pp. 4184-4187, 05/01/ 2000.

[5] C. Caloz and T. Itoh, "Novel microwave devices and structures based on the transmission line approach of meta-materials," in *Microwave Symposium Digest, 2003 IEEE MTT-S International*, 2003, vol. 1, pp. 195-198 vol.1.

[6] C. Caloz and T. Itoh, "Transmission line approach of left-handed (LH) materials and microstrip implementation of an artificial LH transmission line," *Antennas and Propagation, IEEE Transactions on,* vol. 52, no. 5, pp. 1159-1166, 2004.

[7] A. Alburaikan, M. Aqeeli, H. Xianjun, and H. Zhirun, "Miniaturized ultra-wideband bandpass filter based on CRLH-TL unit cell," in *Microwave Conference (EuMC), 2014 44th European*, 2014, pp. 540-543.

[8] A. Alburaikan, M. Aqeeli, X. Huang, and Z. Hu, "Miniaturized via-less ultra-wideband bandpass filter based on CRLH-TL unit cell," in *Radio and Wireless Symposium (RWS), 2015 IEEE*, 2015, pp. 126-128.

[9] J. Xu, W. Wu, and G. Wei, "Novel Dual-Band Bandpass Filter and Reconfigurable Filters Using Lumped-Element Dual-Resonance Resonators," *IEEE Transactions on Microwave Theory and Techniques,* vol. 64, no. 5, pp. 1496-1507, 2016.

[10] J.-S. Hong, *Microstrip filters for RF/microwave applications / bJia-Sheng G. Hong, M. J. Lancaster*. New York: New York : Wiley-Interscience, 2001.

[11] D. M. Pozar, *Microwave engineering / David M. Pozar*. Hoboken, N.J.

New York ; Chichester: Hoboken, N.J. : John Wiley, 2005.

[12] G. L. Matthaei, *Microwave filters, impedance-matching networks and coupl structures*. McGraw-Hill, 1964.

[13] R. E. Collin, *Foundations for microwave engineering / Robert E. Collin*. Maidenhead: Maidenhead : McGraw-Hill, 1992.

[14] P. A. Rizzi, *Microwave engineering : passive circuits / Peter A. Rizzi*. Englewood Cliffs, N.J.: Englewood Cliffs, N.J. : Prentice Hall, 1988.

[15] S. Karimian, "Metamaterial Stepped Impedance Resonator Filters for Wireless Communication Systems," Doctor of Philosophy., Manchester, UK, 2011.

[16] C. Broomfield and J. Everard, "High Q printed helical resonators and filters," in *Frequency Control Symposium and PDA Exhibition Jointly with the 17th European Frequency and Time Forum, 2003. Proceedings of the 2003 IEEE International*, 2003, pp. 819-822.

[17] G. L. Matthaei, "Interdigital Band-Pass Filters," *Microwave Theory and Techniques, IRE Transactions on,* vol. 10, no. 6, pp. 479-491, 1962.

[18] R. Sorrentino and G. Bianchi, *Microwave and RF Engineering*. Wiley, 2010.

[19] Z. Wu, *Software VNA and microwave network design and characterisation / Zhipeng Wu*. Chichester : John Wiley, 2007.

[20] T. S. K. V. Iyer, *Circuit Theory*. Tata McGraw Hill Publishing Company, 1985.

[21]   P. I. Richards, "Resistor-Transmission-Line Circuits," *Proceedings of the IRE,* vol. 36, no. 2, pp. 217-220, 1948.

[22]   *RF and microwave coupled-line circuits / R.K. Mongia ... [et al.].* Boston: Boston : Artech House, 2007.

[23]   S. B. Cohn, "Parallel-Coupled Transmission-Line-Resonator Filters," *Microwave Theory and Techniques, IRE Transactions on,* vol. 6, no. 2, pp. 223-231, 1958.

[24]   M. Gil, J. Bonache, J. Garcia-Garcia, J. Martel, and F. Martin, "Composite Right/Left-Handed Metamaterial Transmission Lines Based on Complementary Split-Rings Resonators and Their Applications to Very Wideband and Compact Filter Design," *Microwave Theory and Techniques, IEEE Transactions on,* vol. 55, no. 6, pp. 1296-1304, 2007.

[25]   M. A. A. Abdalla, *Ferrite left-handed meta-materials for RF microwave applications*. Manchester: Manchester : University of Manchester, 2008.

[26]   R. A. Shelby, D. R. Smith, and S. Schultz, "Experimental Verification of a Negative Index of Refraction," *Science,* vol. 292, no. 5514, pp. 77-79, 2001.

[27]   J. B. Pendry, A. J. Holden, D. J. Robbins, and W. J. Stewart, "Magnetism from conductors and enhanced nonlinear phenomena," *Microwave Theory and Techniques, IEEE Transactions on,* vol. 47, no. 11, pp. 2075-2084, 1999.

[28]   J. B. Pendry, A. J. Holden, D. J. Robbins, and W. J. Stewart, "Low frequency plasmons in thin-wire structures," *J. Phys.-Condes. Matter,* vol. 10, no. 22, pp. 4785-4809, 1998.

[29]   C. Caloz and T. Itoh, "Application of the transmission line theory of left-handed (LH) materials to the realization of a microstrip "LH line"," in *Antennas and Propagation Society International Symposium, 2002. IEEE*, 2002, vol. 2, pp. 412-415 vol.2.

[30]   K. Sungtek and J. Jeongho, "Design of the UWB bandPass filter based on the 1 cell of microstrip CRLH-TL," in *Microwave and Millimeter Wave Technology, 2008. ICMMT 2008. International Conference on*, 2008, vol. 1, pp. 69-72.

[31]   M. Studniberg and G. V. Eleftheriades, "A Dual-Band Bandpass Filter Based on Generalized Negative-Refractive-Index Transmission-Lines," *Microwave and Wireless Components Letters, IEEE,* vol. 19, no. 1, pp. 18-20, 2009.

[32]   H. Tolani, M. A. Ebersp, x00E, cher, and T. F. Eibert, "Composite Right/Left-Handed Leaky Wave Antenna with structurally non-periodic unit cell arrangement," in *Antennas and Propagation Conference (LAPC), 2010 Loughborough*, 2010, pp. 165-168.

[33]   F. Falcone *et al.*, "Babinet Principle Applied to the Design of Metasurfaces and Metamaterials," *Physical Review Letters,* vol. 93, no. 19, p. 197401, 11/01/ 2004.

[34]   M. N. Durán-sindreu, Jordi. Paredes,Ferran.Bonache,Jordi.Martín,Ferran., "Electrically Small Resonators for Planar Metamaterial, Microwave Circuit and Antenna Design: A Comparative Analysis," *Applied Sciences,* vol. 2, no. 2, p. 375, 2012.

[35]   M. Gil, J. Bonache, and F. Martín, "Metamaterial filters: A review," *Metamaterials,* vol. 2, no. 4, pp. 186-197, 12// 2008.

[36]   A. Ali, M. A. Khan, and Z. Hu, "High selectivity lowpass filter using negative-e metamaterial resonators," *Electronics Letters,* vol. 43, no. 9, pp. 528-530, 2007.

[37]   J. Bonache, I. Gil, J. Garcia-Garcia, and F. Martin, "Novel microstrip bandpass filters based on complementary split-ring resonators," *Microwave Theory and Techniques, IEEE Transactions on,* vol. 54, no. 1, pp. 265-271, 2006.

[38]   F. Aznar, M. Gil, J. Bonache, and F. Martin, "Revising the equivalent circuit models of resonant-type metamaterial transmission lines," in *Microwave Symposium Digest, 2008 IEEE MTT-S International*, 2008, pp. 323-326.

[39]   J. Bonache *et al.*, "Super compact split ring resonators CPW band pass filters," in *Microwave Symposium Digest, 2004 IEEE MTT-S International*, 2004, vol. 3, pp. 1483-1486 Vol.3.

[40]   J. Bonache *et al.*, "Application of complementary split-ring resonators to the design of compact narrow band-pass structures in microstrip technology," *Microwave and Optical Technology Letters,* vol. 46, no. 5, pp. 508-512, 2005.

[41]   P. Mondal, M. K. Mandal, A. Chaktabarty, and S. Sanyal, "Compact bandpass filters with wide controllable fractional bandwidth," *IEEE Microwave and Wireless Components Letters,* vol. 16, no. 10, pp. 540-542, 2006.

[42]   J. Zhao, X. Zhang, and H. Liu, "UWB bandpass filter using complementary split-ring resonator-based highpass filter and defected ground structure," in *Electronics, Communications and Control (ICECC), 2011 International Conference on*, 2011, pp. 1194-1196.

[43]   S. Jegadeesan, J. Vijayakrishnan, N. Chandrasekar, and S. Gnanasundar, "Design of compact ultra wide bandpass filter (UWBPF) with metamaterial - Comparison between different CSRRs," in *Signal Processing, Communication and Networking (ICSCN), 2015 3rd International Conference on*, 2015, pp. 1-6.

[44]   T. Chao-Hsiung and T. Itoh, "Dual-Band Bandpass and Bandstop Filters Using Composite Right/Left-Handed Metamaterial Transmission Lines," in *Microwave Symposium Digest, 2006. IEEE MTT-S International*, 2006, pp. 931-934.

[45]   A. K. Horestani, Z. Shaterian, S. Al-Sarawi, D. Abbott, and C. Fumeaux, "Miniaturized bandpass filter with wide stopband using complementary spiral resonator," in *2012 Asia Pacific Microwave Conference Proceedings*, 2012, pp. 550-552.

[46]   L. Rui and Z. Lei, "Compact UWB Bandpass Filter Using Stub-Loaded Multiple-Mode Resonator," *Microwave and Wireless Components Letters, IEEE,* vol. 17, no. 1, pp. 40-42, 2007.

[47]   H. Ching-Luh, H. Fu-Chieh, and K. Jen-Tsai, "Microstrip bandpass filters for Ultra-Wideband (UWB) wireless communications," in *Microwave Symposium Digest, 2005 IEEE MTT-S International*, 2005, p. 4 pp.

[48]   W. T. Fang, T. H. Tseng, and Y. S. Lin, "Miniaturized Ultra-Wideband Bandpass Filter Using Bridged-T Coil," *IEEE Microwave and Wireless Components Letters,* vol. 24, no. 6, pp. 367-369, 2014.

[49]   Y. C. Or and K. W. Leung, "Compact wideband DGS lowpass filter with modified microstripline," *Microw. Opt. Technol. Lett.,* vol. 50, no. 4, pp. 974-977, 2008.

[50]   P. Vagner and M. Kasal, "Design of Microstrip Lowpass Filter Using Defected Ground Structure," in *Radioelektronika, 2007. 17th International Conference*, 2007, pp. 1-4.

[51]   X. Q. Chen, X. W. Shi, and L. X. Wang, "DGS- Based Resonators Form Lowpass Filters," *MICROWAVES & RF,* vol. 48, no. 9, pp. 76-+, 2009.

[52]   A. M. Abbosh, "Design Method for Ultra-Wideband Bandpass Filter With Wide Stopband Using Parallel-Coupled Microstrip Lines," *IEEE Transactions on Microwave Theory and Techniques,* vol. 60, no. 1, pp. 31-38, 2012.

[53]   B. Qian, D. Jun, and G. Chen Jiang, "New design of ultra-wideband bandpass filter using interdigitated coupled lines CRLH-TL structure," in *Antennas, Propagation & EM Theory (ISAPE), 2012 10th International Symposium on*, 2012, pp. 486-489.

[54]   A. M. Abbosh, "Ultrawideband Balanced Bandpass Filter," *IEEE Microw. Wirel. Compon. Lett.,* vol. 21, no. 9, pp. 480-482, 2011.

[55]   M. Mokhtaari, J. Bornemann, and S. Amari, "A Modified Design Approach for Compact Ultra-Wideband Microstrip Filters," *Int. J. RF Microw. Comput-Aid. Eng.,* vol. 20, no. 1, pp. 66-75, 2010.

[56]   B. Xia, L. S. Wu, and J. F. Mao, "An ultra-wideband balanced bandpass filter based on defected ground structures," *Progress In Electromagnetics Research C,* vol. 25, pp. 133-144, 2012.

[57]   A. M. Abbosh, "Planar bandpass filters for ultra-wideband applications," *IEEE Trans. Microw. Theory Tech.,* vol. 55, no. 10, pp. 2262-2269, 2007.

[58]   A. S. H. Kuek, H. T. Su, and M. K. Haldar, "Sextuple-mode ultra-wideband bandpass filter with wide upper stopband," in *Region 10 Symposium, 2014 IEEE*, 2014, pp. 1-5.

[59]   L. Daotong, Z. Yonghong, T. Cong, S. Kaijun, and F. Yong, "A novel UWB bandpass filter based on quadruple-mode resonator," in *Wireless Symposium (IWS), 2015 IEEE International*, 2015, pp. 1-3.

[60]   X. B. Wei, Y. Shi, P. Wang, J. X. Liao, Z. Q. Xu, and B. C. Yang, "Compact dual-band bandpass filter with improved stopband characteristics," *Electronics Letters,* vol. 48, no. 12, pp. 704-705, 2012.

[61]   C. Yu-Chi, K. Chia-Hsiung, W. Min-Hang, and Y. Ru-Yuan, "Design of the Compact Dual-Band Bandpass Filter With High Isolation for GPS/WLAN Applications," *Microwave and Wireless Components Letters, IEEE,* vol. 19, no. 12, pp. 780-782, 2009.

[62]   C. Chu-Yu and H. Cheng-Ying, "A simple and effective method for microstrip dual-band filters design," *Microwave and Wireless Components Letters, IEEE,* vol. 16, no. 5, pp. 246-248, 2006.

[63]   C. Chi-Feng, T.-Y. Huang, and R.-B. Wu, "Design of Dual- and Triple-Passband Filters Using Alternately Cascaded Multiband Resonators," *Microwave Theory and Techniques, IEEE Transactions on,* vol. 54, no. 9, pp. 3550-3558, 2006.

[64]   S. Sheng, "A Dual-Band Bandpass Filter Using a Single Dual-Mode Ring Resonator," *Microwave and Wireless Components Letters, IEEE,* vol. 21, no. 6, pp. 298-300, 2011.

[65]   C. Yi-Chyun, W. Cho-Yu, and K. Jen-Tsai, "New Miniaturized Dual-Mode Dual-Band Ring Resonator Bandpass Filter With Microwave ≪formula formulatype="inline"> <img src="/images/tex/276.gif" alt="C"> </formula>-Sections," *Microwave and Wireless Components Letters, IEEE,* vol. 20, no. 2, pp. 67-69, 2010.

[66]   L. Sha, Z. Lei, and S. Sheng, "A Dual-Band Ring-Resonator Bandpass Filter Based on Two Pairs of Degenerate Modes," *Microwave Theory and Techniques, IEEE Transactions on,* vol. 58, no. 12, pp. 3427-3432, 2010.

[67]   T. Lin-Chuan and H. Ching-Wen, "Dual-band bandpass filters using equal-length coupled-serial-shunted lines and Z-transform technique," *Microwave Theory and Techniques, IEEE Transactions on,* vol. 52, no. 4, pp. 1111-1117, 2004.

[68]   L. An-Shyi, T.-Y. Huang, and R.-B. Wu, "A Dual Wideband Filter Design Using Frequency Mapping and Stepped-Impedance Resonators," *Microwave Theory and Techniques, IEEE Transactions on,* vol. 56, no. 12, pp. 2921-2929, 2008.

[69]   R. Loeches-Sanchez, D. Psychogiou, D. Peroulis, and R. Gomez-Garcia, "Sharp-rejection highpass and dual-band bandpass planar filters with multi-transmission-zero-generation transversal cell," in *Radio and Wireless Symposium (RWS), 2015 IEEE*, 2015, pp. 147-149.

[70]   R. Gomez-Garcia and M. Sanchez-Renedo, "Microwave Dual-Band Bandpass Planar Filters Based on Generalized Branch-Line Hybrids," *IEEE Transactions on Microwave Theory and Techniques,* vol. 58, no. 12, pp. 3760-3769, 2010.

[71]   M. A. Sanchez-Soriano and R. Gomez-Garcia, "Sharp-Rejection Wide-Band Dual-Band Bandpass Planar Filters With Broadly-Separated Passbands," *Microwave and Wireless Components Letters, IEEE,* vol. 25, no. 2, pp. 97-99, 2015.

[72]   B. M. Schiffman and G. L. Matthaei, "Exact Design of Band-Stop Microwave Filters," *Microwave Theory and Techniques, IEEE Transactions on,* vol. 12, no. 1, pp. 6-15, 1964.

[73]   M. Hayati and A. Khajavi, "A Dual-Band Bandpass Filter Using Coupled Semi-circular Stepped Impedance Resonators with Sharp Roll-off and Wide Stopband," (in English), *Arabian Journal for Science and Engineering,* vol. 39, no. 5, pp. 3963-3968, 2014/05/01 2014.

[74]   L. Yuan Chun, W. Hang, and X. Quan, "Dual-Mode Dual-Band Bandpass Filter Based on a Stub-Loaded Patch Resonator," *Microwave and Wireless Components Letters, IEEE,* vol. 21, no. 10, pp. 525-527, 2011.

[75]   C. Kuo-Sheng and Y. Jun-Hong, "Dual-Wideband Bandpass Filter Using Short-Circuited Stepped-Impedance Resonators," *Microwave and Wireless Components Letters, IEEE,* vol. 19, no. 3, pp. 155-157, 2009.

[76] X. Jin, W. Wen, and M. Chen, "Compact Microstrip Dual-/Tri-/Quad-Band Bandpass Filter Using Open Stubs Loaded Shorted Stepped-Impedance Resonator," *Microwave Theory and Techniques, IEEE Transactions on,* vol. 61, no. 9, pp. 3187-3199, 2013.

[77] Z. Runqi, L. Sha, and Z. Lei, "Asymmetrical-Response Dual-Band Bandpass Filters on <formula formulatype="inline"> <img src="/images/tex/18921.gif" alt="\lambda /8"> </formula> Transmission Lines With Modified Richard's Transformation," *Microwave and Wireless Components Letters, IEEE,* vol. 24, no. 10, pp. 680-682, 2014.

[78] X. Jin, W. Wen, and M. Chen, "Compact and Sharp Skirts Microstrip Dual-Mode Dual-Band Bandpass Filter Using a Single Quadruple-Mode Resonator (QMR)," *Microwave Theory and Techniques, IEEE Transactions on,* vol. 61, no. 3, pp. 1104-1113, 2013.

[79] J. G. Zhou, W. J. Feng, and W. Q. Che, "Dual-wideband bandpass filter using T-shaped structure based on transversal signal-interaction concepts," *Electronics Letters,* vol. 48, no. 24, pp. 1539-1540, 2012.

[80] Z. Runqi, Z. Lei, and L. Sha, "Dual-Mode Dual-Band Bandpass Filter Using a Single Slotted Circular Patch Resonator," *Microwave and Wireless Components Letters, IEEE,* vol. 22, no. 5, pp. 233-235, 2012.

[81] Z. Runqi and Z. Lei, "Design of a Compact Dual-Band Bandpass Filter Using Coupled Stepped-Impedance Resonators," *Microwave and Wireless Components Letters, IEEE,* vol. 24, no. 3, pp. 155-157, 2014.

[82] C. Fulong, S. Kaijun, H. Bingkun, and F. Yong, "Compact Dual-band Bandpass Filter Using HMSIW Resonator and Slot Perturbation," *Microwave and Wireless Components Letters, IEEE,* vol. 24, no. 10, pp. 686-688, 2014.

[83] Z. Runqi and Z. Lei, "Synthesis of Dual-Wideband Bandpass Filters With Source-Load Coupling Network," *Microwave Theory and Techniques, IEEE Transactions on,* vol. 62, no. 3, pp. 441-449, 2014.

[84] M. Bhardwaj, *Design of Voltage Controlled Oscillator*. Saarbrücken, Germany: Lambert Academic Publishing, 2011.

[85] R. G. Rogers, *Low phase noise microwave oscillator design*. Boston, Mass. ; London: Boston, Mass. ; London : Artech House, 1991.

[86] D. B. Leeson, "A simple model of feedback oscillator noise spectrum," *Proceedings of the IEEE,* vol. 54, no. 2, pp. 329-330, 1966.

[87] B. Razavi, "A study of phase noise in CMOS oscillators," *Solid-State Circuits, IEEE Journal of,* vol. 31, no. 3, pp. 331-343, 1996.

[88] G. Lan, D. Kalokitis, E. Mykietyn, E. Hoffman, and F. Sechi, "Highly Stabilized, Ultra-Low Noise FET Oscillator with Dielectric Resonator," in *Microwave Symposium Digest, 1986 IEEE MTT-S International*, 1986, pp. 83-86.

[89] G. D. Vendelin, *Microwave circuit design using linear and nonlinear techniques / George D. Vendelin, Anthony M. Pavio, Ulrich L. Rohde*. New York ; Chichester: New York ; Chichester : Wiley, 1990.

[90] T. Chao-Hsiung and C. Chih-Lin, "Design of Low Phase-Noise Microwave Oscillator and Wideband VCO Based on Microstrip Combline Bandpass Filters," *Microwave Theory and Techniques, IEEE Transactions on,* vol. 60, no. 10, pp. 3151-3160, 2012.

[91] T. Ohira, "Rigorous Q-factor formulation for one- and two-port passive linear networks from an oscillator noise spectrum viewpoint," *Circuits and Systems II: Express Briefs, IEEE Transactions on,* vol. 52, no. 12, pp. 846-850, 2005.

[92] J. B. Encinas, *Phase locked loops*. London: London : Chapman & Hall, 1993.

[93] K. a. Shu, *CMOS PLL Synthesizers: Analysis and Design*. Boston, MA : Springer US, 2005.

[94] C. Jonghoon, C. Meng-Hung, and A. Mortazawi, "An X-band Low Phase Noise Oscillator Employing a Four-pole Elliptic-Response Microstrip Bandpass Filter," in *Microwave Symposium, 2007. IEEE/MTT-S International*, 2007, pp. 1529-1532.

[95] C. Jonghoon, M. Nick, and A. Mortazawi, "Low Phase-Noise Planar Oscillators Employing Elliptic-Response Bandpass Filters," *Microwave Theory and Techniques, IEEE Transactions on,* vol. 57, no. 8, pp. 1959-1965, 2009.

[96] C. Jaewon and S. Chulhun, "Microstrip Square Open-Loop Multiple Split-Ring Resonator for Low-Phase-Noise VCO," *Microwave Theory and Techniques, IEEE Transactions on,* vol. 56, no. 12, pp. 3245-3252, 2008.

[97] H. Weichen, Z. Jianyi, and C. Peng, "An X-Band Low Phase Noise Free-Running Oscillator Using Substrate Integrated Waveguide Dual-Mode Bandpass Filter With Circular Cavity," *Microwave and Wireless Components Letters, IEEE,* vol. 25, no. 1, pp. 40-42, 2015.

[98] M. Nick and A. Mortazawi, "Low Phase-Noise Planar Oscillators Based on Low-Noise Active Resonators," *Microwave Theory and Techniques, IEEE Transactions on,* vol. 58, no. 5, pp. 1133-1139, 2010.

[99] N. H.V and C. C, "Broadband highly selective bandpass filter based on a tapered coupled-resonator CRLH structure," in *Proceedings of the European Microwave Association*, 2006, vol. 2, no. March 2006, pp. 44 - 51.

[100] M. Gil, J. Bonache, and F. Martin, "Synthesis and applications of new left handed microstrip lines with complementary split-ring resonators etched on the signal strip," *Microwaves, Antennas & Propagation, IET,* vol. 2, no. 4, pp. 324-330, 2008.

[101] M. Gil, J. Bonache, and F. Martin, "Synthesis and applications of new left handed microstrip lines with complementary split-ring resonators etched on the signal strip," *Microwaves, Antennas & Propagation, IET,* vol. 2, no. 4, pp. 324-330, 2008.

[102] Q. L. Zhang, W. Y. Yin, S. He, and L. S. Wu, "Compact Substrate Integrated Waveguide (SIW) Bandpass Filter With Complementary Split-Ring Resonators (CSRRs)," *IEEE Microwave and Wireless Components Letters,* vol. 20, no. 8, pp. 426-428, 2010.

[103] R. W. Ziolkowski, "Design, fabrication, and testing of double negative metamaterials," *Antennas and Propagation, IEEE Transactions on,* vol. 51, no. 7, pp. 1516-1529, 2003.

[104] M. H. Weik, *Fiber optics and lightwave communications standard dictionary*. New York ; London: New York ; London : Van Nostrand Reinhold, 1981.

[105] S. Tanaka, K. Mukaida, and R. Sugita, "High-Q CRLH transmission line stub resonator utilizing negative order resonance modes," in *Microwave Conference (EuMC), 2013 European*, 2013, pp. 585-588.

[106] Infineon. Low Noise Silicon Bipolar RF Transistor BFP405 [Online]. Available: http://www.infineon.com/dgdl/Infineon-BFP405-DS-v01_01-en.pdf?fileId=db3a30431400ef68011427753c330778

[107] A. Technologies, "Harmonic Balance Simulation," ed, 2006.

[108] M. Tiebout, "Low-power low-phase-noise differentially tuned quadrature VCO design in standard CMOS," *Solid-State Circuits, IEEE Journal of,* vol. 36, no. 7, pp. 1018-1024, 2001.

[109] C. Zhe, H. Wei, C. Jixin, and Z. Jianyi, "Design of High-Q Tunable SIW Resonator and Its Application to Low Phase Noise VCO," *Microwave and Wireless Components Letters, IEEE,* vol. 23, no. 1, pp. 43-45, 2013.

[110] C. Chih-Lin and T. Chao-Hsiung, "Design of Low Phase-Noise Oscillator and Voltage-Controlled Oscillator Using Microstrip Trisection Bandpass Filter," *Microwave and Wireless Components Letters, IEEE,* vol. 21, no. 11, pp. 622-624, 2011.

[111] M. Byeong-Taek and M. Noh-Hoon, "Design of Low Phase-Noise Oscillator Based on a Hairpin-Shaped Resonator Using Composite Right/Left-Handed Transmission Line," *Microwave and Wireless Components Letters, IEEE,* vol. 24, no. 1, pp. 44-46, 2014.

[112] A. Dal, K. Chul-Soo, C. Min-Ho, L. Dwong-Hwan, L. Dae Won, and H. Heon Jin, "The design of parallel coupled line filter with arbitrary image impedance," in *Microwave Symposium Digest, 1998 IEEE MTT-S International*, 1998, vol. 2, pp. 909-912 vol.2.

[113] C. Y. Chang and T. Itoh, "A modified parallel-coupled filter structure that improves the upper stopband rejection and response symmetry," *IEEE Transactions on Microwave Theory and Techniques,* vol. 39, no. 2, pp. 310-314, 1991.

[114] K. Jen-Tsai, C. Sin-Ping, and J. Meshon, "Parallel-coupled microstrip filters with over-coupled end stages for suppression of spurious responses," *IEEE Microwave and Wireless Components Letters,* vol. 13, no. 10, pp. 440-442, 2003.

[115] C. Ka Fai and T. Kam Weng, "Miniaturized cross-coupled filter with second and third spurious responses suppression," *IEEE Microwave and Wireless Components Letters,* vol. 15, no. 2, pp. 122-124, 2005.

[116] C. W. Tang, C. T. Tseng, S. H. Chiu, and P. H. Wu, "Design of Wide Passband/Stopband Microstrip Bandpass Filters With the Stepped Coupled Line," *IEEE Transactions on Microwave Theory and Techniques,* vol. 61, no. 3, pp. 1095-1103, 2013.

[117] M. Akra, E. Pistono, H. Issa, A. Jrad, and P. Ferrari, "Full Study of the Parallel-Coupled Stub-Loaded Resonator: Synthesis Method in a Narrow Band With an Extended Optimal Rejection Bandwidth," *IEEE Transactions on Microwave Theory and Techniques,* vol. 62, no. 12, pp. 3380-3392, 2014.

[118] Q. Y. Guo, X. Y. Zhang, L. Gao, Y. C. Li, and J. X. Chen, "Microwave and Millimeter-Wave LTCC Filters Using Discriminating Coupling for Mode Suppression," *IEEE Transactions on Components, Packaging and Manufacturing Technology,* vol. 6, no. 2, pp. 272-281, 2016.

[119] R. Gomez-Garcia and J. I. Alonso, "Design of sharp-rejection and low-loss wide-band planar filters using signal-interference techniques," *IEEE Microwave and Wireless Components Letters,* vol. 15, no. 8, pp. 530-532, 2005.

[120] F. Wen Jie, C. Wen Quan, C. Yu Mei, S. Su Yang, and X. Quan, "High Selectivity Fifth-Order Wideband Bandpass Filters With Multiple Transmission Zeros Based on Transversal Signal-Interaction Concepts," *Microwave Theory and Techniques, IEEE Transactions on,* vol. 61, no. 1, pp. 89-97, 2013.

[121] R. Zhang and L. Zhu, "Design of a Wideband Bandpass Filter With Composite Short- and Open-Circuited Stubs," *IEEE Microwave and Wireless Components Letters,* vol. 24, no. 2, pp. 96-98, 2014.

[122] A. Alburaikan, M. Aqeeli, X. Huang, and Z. Hu, "Low Phase Noise Free-Running Oscillator Based on High Selectivity Bandpass Filter Using Composite Right/Left-Handed Transmission Line," *IEEE Microwave and Wireless Components Letters,* vol. PP, no. 99, pp. 1-3, 2016.

[123] G. Nikandish and A. Medi, "Transformer-Feedback Interstage Bandwidth Enhancement for MMIC Multistage Amplifiers," *IEEE Transactions on Microwave Theory and Techniques,* vol. 63, no. 2, pp. 441-448, 2015.

[124] O. Garcia-Perez, A. Garcia-Lamperez, V. Gonzalez-Posadas, M. Salazar-Palma, and D. Segovia-Vargas, "Dual-Band Recursive Active Filters With Composite Right/Left-Handed Transmission Lines," *IEEE Transactions on Microwave Theory and Techniques,* vol. 57, no. 5, pp. 1180-1187, 2009.

[125] K. Laker and M. Ghausi, "A comparison of active, multiple-loop feedback techniques for realizing high order bandpass filters," *IEEE Transactions on Circuits and Systems,* vol. 21, no. 6, pp. 774-783, 1974.

[126] F. Cervera and H. Jiasheng, "High Rejection, Self-Packaged Low-Pass Filter Using Multilayer Liquid Crystal Polymer Technology," *IEEE Transactions on Microwave Theory and Techniques,* vol. 63, no. 12, pp. 3920-3928, 2015.

[127] R. Gomez-Garcia, R. Loeches-Sanchez, D. Psychogiou, and D. Peroulis, "Single/multi-band Wilkinson-type power dividers with embedded transversal filtering sections and application to channelized filters," *Circuits and Systems I: Regular Papers, IEEE Transactions on,* vol. 62, no. 6, pp. 1518-1527, 2015.

[128] F. Wenjie, C. Wenquan, and X. Quan, "Transversal Signal Interaction: Overview of High-Performance Wideband Bandpass Filters," *Microwave Magazine, IEEE,* vol. 15, no. 2, pp. 84-96, 2014.

[129] J. X. Chen, C. Shao, Q. Y. Lu, H. Tang, and Z. H. Bao, "Compact LTCC balanced bandpass filter using distributed-element resonator," *Electronics Letters,* vol. 49, no. 5, pp. 354-356, 2013.

[130] T. Yang, M. Tamura, and T. Itoh, "Super Compact Low-Temperature Co-Fired Ceramic Bandpass Filters Using the Hybrid Resonator," *IEEE Transactions on Microwave Theory and Techniques,* vol. 58, no. 11, pp. 2896-2907, 2010.

[131] X. Dai, X. Y. Zhang, H. L. Kao, B. H. Wei, J. X. Xu, and X. Li, "LTCC Bandpass Filter With Wide Stopband Based on Electric and Magnetic Coupling Cancellation," *IEEE Transactions on Components, Packaging and Manufacturing Technology,* vol. 4, no. 10, pp. 1705-1713, 2014.

[132] X. Y. Zhang, X. Dai, H. L. Kao, B. H. Wei, Z. Y. Cai, and Q. Xue, "Compact LTCC Bandpass Filter With Wide Stopband Using Discriminating Coupling," *IEEE Transactions on Components, Packaging and Manufacturing Technology,* vol. 4, no. 4, pp. 656-663, 2014.

[133] Z. Q. Xu, P. Wang, J. X. Liao, and Y. Shi, "Substrate integrated waveguide filter with mixed coupled modified trisections," *Electronics Letters,* vol. 49, no. 7, pp. 482-483, 2013.

[134] J. X. Xu, X. Y. Zhang, X. L. Zhao, and Q. Xue, "Synthesis and Implementation of LTCC Bandpass Filter With Harmonic Suppression," *IEEE Transactions on Components, Packaging and Manufacturing Technology,* vol. 6, no. 4, pp. 596-604, 2016.

[135] J. Yng-Huey, S. F. R. Chang, and L. Hsiao-Kuang, "A high stopband-rejection LTCC filter with multiple transmission zeros," *IEEE Transactions on Microwave Theory and Techniques,* vol. 54, no. 2, pp. 633-638, 2006.

[136] J. T. Kuo and E. Shih, "Microstrip stepped impedance resonator bandpass filter with an extended optimal rejection bandwidth," *IEEE Transactions on Microwave Theory and Techniques,* vol. 51, no. 5, pp. 1554-1559, 2003.